



Smith, Scott Graeme (2017) *Electrons as probes of chiral materials*.
PhD thesis.

<http://theses.gla.ac.uk/8580/>

Copyright and moral rights for this work are retained by the author

A copy can be downloaded for personal non-commercial research or study, without prior permission or charge

This work cannot be reproduced or quoted extensively from without first obtaining permission in writing from the author

The content must not be changed in any way or sold commercially in any format or medium without the formal permission of the author

When referring to this work, full bibliographic details including the author, title, awarding institution and date of the thesis must be given

Enlighten:Theses
<http://theses.gla.ac.uk/>
theses@gl.a.ac.uk

Electrons as Probes of Chiral Materials



Scott Graeme Smith

School of Physics and Astronomy
University of Glasgow

This dissertation is submitted for the degree of
Doctor of Philosophy

November 2017

Abstract

In this work we present electron beam techniques for probing the chiral structure of materials. The motivation for the work lies in two distinct aspects of chiral materials science. In the first case, chiral plasmonic excitations have recently been proposed for use in a variety of sensing technologies but require structural optimisation, in which modern electron microscopy techniques excel. In the second case, the recent development of intrinsically chiral electron ‘vortex beams’ suggests the prospect of being able to discriminate chiral crystal structures directly within the electron microscope. We were keen to explore this prospect because it could overcome a long-standing and fundamental limitation in TEM techniques.

The introduction section of this thesis provides an overview of the essential background and theory underpinning the research, specifically considering the theory of surface plasmons, the properties of electron beams and a description of crystal chirality, all of which will be used in our work. We give a description of diffraction of electrons in a crystal and show the wavefunctions of electron vortex beams. Results show electron channeling in a simple cubic crystal, highlighting the impact of the position of the beam on the unit cell. When the beam is focused onto an atomic column the electrons are forward scattered along the column, whereas they are scattered outwards when the beam is centered between columns.

In Chapter 2 we discuss the details of data acquisition and post processing techniques, namely Richardson-Lucy deconvolution and non-negative matrix factorisation, which together extract plasmonic modes from EELS data sets. We give a detailed analysis of the plasmonic excitations which exist on the surfaces of both a nanopatterned gold chiral nanoparticle and a hole in a continuous metallic film that also supports localised surface plasmon resonances. We show, using EELS in a scanning transmission electron microscope that we can map the resonance modes of the structure with high spatial resolution. We confirm the link between the modes supported by a plasmonic nanoparticle and a hole of similar shape, though we find that 3D roughness has an effect on the energy of the modes, shifting modes by around $0.3eV$ in some cases. The modes found are chiral leading to chiral fields, which have applications as sensors of biological molecules.

In Chapter 3 we demonstrate the ability to simulate EELS, with accuracy, of realistic plasmonic nanoparticles with 3D shapes which extends beyond the usual two-dimensional or idealised simulations of the literature. We study the effects of inevitable manufacturing and other structural imperfections on the plasmonic response of real patterned structures and show that they lead to shifts in energy and spatial intensity of the modes due to these

defects. We find that structural defects are enough to make so called dark modes (ie. those that do not have dipole character and are therefore not usually excited by incident photons) become bright, and shift the energy of modes between similar structures. We also illustrate the ability to predict the intensity distribution of plasmonic modes on structures using only symmetry arguments. This type of calculation gives a simple derivation of the modes which would exist on a plasmonic nanoparticle without requiring a more complicated eigenmode analysis. Using symmetry terms and irreducible representations the modes which appear on a nanoparticle can be grouped by symmetry terms, allowing the breaking of symmetry, via defects, to be better be visualised.

In the latter part of this work we turn to a completely different experiment to consider the exploitation of newly-discovered vortex electron beams in assigning chirality to crystals within a simple electron microscopy experiment. With these beams, which possess an orbital angular momentum, will show that it is possible (in favourable cases) to detect the handedness of the crystal via a difference in diffraction pattern intensity distribution for beams of opposite OAM, when scattering in opposite handed crystals. Our work demonstrates the ease of assigning chirality using convergent electron vortex diffraction for a crystal with a threefold, fourfold and sixfold screw axis. We present this work using modified multislice simulations of the diffraction of vortex electron beams from chiral potential layers. We demonstrate that the azimuthal phase component of electron vortex beams opens up new opportunities for rapid chiral discrimination and structural studies in electron diffraction. We show that the symmetry of the resulting convergent beam patterns matches the point symmetry of the crystal only when the handedness of both the impinging vortex probe and chirality of the crystal are congruent. This methodology was tested on the real crystal structures of α -quartz and the magnetic crystal $Cr\frac{1}{3}NbS_2$. It was found that effects (due to the matching of the beam and crystal chirality) are most obvious in the overlap of diffraction disks, where interference effects allow the novel phase profile of vortex beams to produce intensity variations. The thickness of the crystal, the convergence angle and the energy of the beam were all parameters which need to be tuned in order to achieve chiral specific scattering. In thinner crystals the effects were less obvious, requiring a deduction in the beam energy in order to see a difference between CBED patterns of enantiomers. In cases where the convergence angle did not lead to overlapping disks in the CBED pattern the effects of chiral specific scattering were not obvious. Future work should include an experimental check of the feasibility of observing such weak diffraction effects in an electron microscope. Should this prove possible, this method could be of use to discriminate chiral crystal structures directly within the electron microscope using only one set of diffraction patterns.

“We all change, when you think about it. We’re all different people all through our lives. And that’s OK, that’s good, you gotta keep moving, so long as you remember all the people that you used to be. I will never forget one line of this, not one day, I swear, I will always remember when the Doctor was me. ”

-11th Doctor

Declaration

This thesis has been written by myself and details the research I have carried out within the MCMP group under the supervision of Prof. Robert L Stamps, and Dr Donald A MacLaren and in the school of Physics and Astronomy at the University of Glasgow from 2012 - 2017. The work described is my own except where otherwise stated. This thesis has not previously been submitted for a higher degree.

Scott Graeme Smith

November 2017

Acknowledgements

I would like to thank my supervisors Dr Donald MacLaren and Professor Robert Stamps, for all the support during the last four years. Their guidance, patience and encouragement are the reason for this PhD thesis being possible. It has been a pleasure working under your supervision and I feel very fortunate to have been welcomed into the group.

I would also like to thank all the members of the MCMP group, they say all good things must come to an end, but I hope the friendships gained over the last four years continue on. I would especially like to thank Gary for all his help and support over the course of my thesis. This work would not have been possible had it not been for him. Also thank you to Matus, my office mate and friend. Also a special mention to Dominic, who introduced me to the department and quickly became the best part of my first year. Thank you to Mathew who helped teach me about the joys of vortex beams.

Special mention has to go to Kirsty who kept me sane and normal all those days in 409. I am unbelievably fortunate to call her a friend and her friendship is one of the best things to come from my PhD.

I would like to say a huge thank you to my family and friends, who's emotional support and love have propelled me through the difficult days. Despite not really knowing what I did, they encouraged me nonetheless. Especially to Ashleigh and Craig who let me live with them while I began the long task of writing this. To my Mum and Robert who told me often how proud they were of me. To my Dad and to my Stepmum Lee who believed in me from the very beginning.

Thank you to Claire, Greg, Kyle and Jennifer, my wonderful friends who helped keep me laughing throughout my PhD. No matter what distance we are separated by they were always a phone call away whenever I needed them.

And finally, they say that doing a PhD sometimes feels like a 24 hour job. On those long days and late nights in the office it makes all the difference to have a friend there with you. From motivational quotes to late night pep talks, to simply believing in me, I know that this thesis is more a testament to his patience than it is to mine. I can say with absolute certainty that had it not been for him I would never have made it to the other side. So to Rair Macêdo I would like say thank you for making this possible.

Table of contents

List of figures	xv
List of tables	xxv
1 Introduction	1
1.1 Overview	1
1.2 Free Electron Beams	2
1.2.1 Electron Wavelength	2
1.2.2 Electron Matter Interactions	3
1.2.3 Electron Coherence and Diffraction	6
1.2.4 Electron Channelling	9
1.3 Surface Plasmons	9
1.3.1 Propagating Surface Plasmons	11
1.3.2 Localised Surface Plasmons	14
1.3.3 Boundary Element Method	15
1.4 The Electron Microscope	17
1.4.1 Electron Sources	17
1.4.2 Electron Microscope Optics	18
1.5 Electron Energy Loss Spectroscopy	19
1.5.1 An Electron Energy Loss Spectrum	19
1.5.2 Spectrum Imaging	21
1.6 Chirality and How it is Studied	22
1.6.1 Chiral Plasmonic Nanostructures	23
1.6.2 Observing Crystal Chirality in the Transmission Electron Microscope	24
1.7 Optical and Electron Vortices	25
1.7.1 Orbital Angular Momentum	29
1.8 The Multislice Method	30
1.9 Outline of Thesis	31
2 Experimental Comparison of Gold Chiral Plasmonic Nanoparticles.	33
2.1 Introduction	33
2.2 Plasmonic Hole Structures	36

2.3	Localised Surfaces Plasmons in Coupled Nanospheres	37
2.4	Optical and Electron Spectroscopies	38
2.5	Babinet's Principle	40
2.6	Chiral Metamaterials	41
2.7	Experimental Details	42
2.8	Richardson-Lucy Deconvolution of Experimental Data Set	44
2.9	Matrix Factorization of Experimental Data Set	45
2.10	Experimental Modes	46
2.11	Thickness Calculation of Negative Nanoparticle	48
2.12	Conclusion	50
3	Simulated Comparison of Chiral Gold Plasmonic Nanoparticles.	53
3.1	Introduction	53
3.2	Edge Imperfections and Roughness in a Realistic Nanoparticle	54
3.3	Creating a Mesh	56
3.4	Symmetry Analysis	58
3.4.1	Symmetry Analysis of a Positive Plasmonic Nanoparticle	58
3.5	Eigenmode Analysis	62
3.5.1	Eigenmodes of an Ideal Positive Plasmonic Nanoparticle	62
3.5.2	Eigenmodes of an Experimentally Realistic Positive Plasmonic Nanoparticle	65
3.5.3	Eigenmodes of a Devised Positive Plasmonic Nanoparticle	68
3.5.4	Eigenmodes of an Experimental Realistic Negative Plasmonic Particle	71
3.6	Electron Energy Loss Maps of the Nanoparticles	74
3.6.1	EELS Maps of an Ideal Positive Plasmonic Nanoparticle	74
3.6.2	EELS Maps of an Actual Positive Plasmonic Nanoparticle	76
3.6.3	EELS Maps of a Devised Positive Plasmonic Nanoparticle	78
3.6.4	EELS Maps of an Experimentally Realistic Negative Plasmonic Nanoparticle	80
3.7	Electric Fields of the Structures	81
3.7.1	Field Chirality	81
3.8	Effect of Adding a Substrate	84
3.9	Conclusion	88
4	Convergent Beam Electron Diffraction with Electron Vortex Beams	91
4.1	Introduction	91
4.2	Convergent Beam Electron Diffraction	92
4.3	Vortex Beam Diffraction in a Achiral Crystal	93
4.4	Vortex Beam Diffraction in a Square Chiral Crystal	97
4.5	Vortex Beam Diffraction in a Hexagonal Chiral Crystal	107
4.6	Vortex Beam Diffraction in Quartz	114

4.7	Vortex Beam Diffraction in <i>NbSCr</i>	118
4.8	Conclusions	120
5	Outlook	121
5.1	Conclusion and Outlook	121
	References	123

List of figures

1.1	a) Diagram showing the various ways an electron beam can interact with a specimen. b) Graph showing the cross sections for some of the interactions shown in a). The graph shows that losses leading to the generation of plasmons have the highest cross section, followed by elastic losses. K- and L-shell ionisation is less likely and even less likely is the generation of secondary electrons. Adapted from Williams and Carter [1].	4
1.2	The mechanics of electron diffraction. a) A plane wave electron beam is scattered by a column of atoms by an angle θ . b) The scattered and incident beams, k_s and k_i , can be visualised in reciprocal space using the concept of the Ewald Sphere. c) Using the points where the Ewald Sphere touches the reciprocal lattice allows us to see the zero-order Laue zones (ZOLZ) and higher-order Laue zones (HOLZ).	8
1.3	Simulated wavefunctions for a planewave electron beam focused at different points on the unit cell of iron. For a beam positioned (a) on an atomic column, (b) between two atomic columns and (c) in free space. The wavefunctions after (d,e,f) 1 unit cell (g,h,i) 2 unit cells and (j,k,l) 3 unit cells are shown. The on column beam channels quicker than that positioned between columns. Over this distance the beam in free space does not change.	10
1.4	(a) Propagating surface plasmon at the interface between a dielectric and a metal. The arrows indicate the electric field at the interface. The surface plasmon is an electromagnetic excitation which propagates along the interface, in the x direction b) The field caused by the surface plasmon has an exponential decay shown in green, this decay happens faster in the metal than in the dielectric. This results in the enhanced near field applications of surface plasmons.	12
1.5	A localised surface plasmon occurs in nanoparticles which are small enough to see the outside perturbation as a static excitation leading to a standing wave mode.	14

1.6	Effect of particle size on resonant peaks for a planewave excitation of a gold nanosphere. We see that when the particle size is increased there is both a shift in wavelength of the plasmon mode, by about $10nm$ and a decrease in the overall intensity. This is what we would expect from the analysis. . . .	15
1.7	Typical ray diagram for a transmission electron microscope operated in a) CTEM and b) STEM mode. An electron source emits electrons which are focused through a series of apertures and electromagnetic lenses to be imaged. In CTEM the specimen is illuminated by a planewave electron beam, whereas in STEM the beam is focused to a spot.	20
1.8	Schematic of the EELS spectrometer where a magnetic prism is used to disperse electrons according to their momentum (kinetic energy). Electrons that lose no energy will be deflected by a given angle, whereas electrons that have scattered inelastically will be dispersed as a measure of the energy lost with respect to the incident beam.	21
1.9	A typical EELS loss spectrum which plots the signal intensity against the energy loss of electrons as they pass the sample. This shows a low loss region, where the dominant feature is the zero-loss peak. The first plasmon peaks can be observed close to the zero-loss. At higher energy, moving towards the high loss part of the spectrum, the bulk plasmon can be seen.	22
1.10	A schematic diagram of spectrum imaging, showing the 4D data cube, which can be used for quantitative analysis of EELS. At each pixel in the STEM image a loss spectrum is obtained.	23
1.11	The chiral space groups a) $P3_121$ and b) $P3_221$. The black triangles show threefold screw axes perpendicular to the plane of the page. The red circles show symmetry equivalent points. The superscript numbers, above the circles, denote the height in the c direction (perpendicular to the page). See [2] for more details.	24
1.12	The wavefront for a) $l=-1$, b) $l=0$ and c) $l=+1$ electron beam, the different values of l give rise to twisted wavefronts for the vortex beams and the planar wavefront of a planewave. The twisted wavefront gives rise to a quantised OAM about the axis of propagation.	25
1.13	A 2D representation in the (x,y) plane showing the a) real and b) imaginary parts of a Gaussian wavefunction, Ψ . Before propagating through the crystal the Gaussian wavefunction is purely real.	26
1.14	A 2D representation in the (x,y) plane showing the a) real and b) imaginary parts of a vortex wavefunction, Ψ . Note the presence of imaginary part in the wavefunction of a vortex beam when compared with a Gaussian beam. . . .	27

1.15	A 2D representation of the probability density a) of the beam shown in Figure 1.13 and b) Figure 1.14 showing a Gaussian and vortex beams probability density respectively. Due to the difference in intensity distribution the vortex beam appears less intense.	28
1.16	The 2D probability current $j(x,y)$ of the beams shown in a) Figure 1.13 and b) Figure 1.14. Notice that the Gaussian probability current propagates outwards from a point, whereas the vortex current is a circulation about the centre. This is the inherent chirality of the beam.	28
1.17	Schematic of the Multislice method. In this method a crystal is divided into potential slices in the direction of propagation the effects of each slice are calculated individually and then the wavefunction is propagated through free space.	31
2.1	The Lycurgus Cup is one of the oldest examples of the exploitation of the unique interaction of nanoparticles with light. The cup appears a) green in colour when seen by reflected light and b) red when lit from within the cup. Printed with permission from the British Museum [3].	33
2.2	Coupling effects between nanospheres, calculated using the MNPBEM toolbox as discussed in Section 1.3.3. We see that when a second sphere is added there is a shift in wavelength and thus in energy of the plasmon mode, by about 15 nm (80 eV) and an increase in the overall intensity.	37
2.3	a) Typical EELS spectrum showing the three resonant modes of a gold patterned nanotriangle of width 80nm. The electron beam is positioned on the points shown in the inset. The 2D loss maps produced at each of the three resonant modes in the EELS loss spectra are shown at energies of b) 1.87 eV, c) 2.19 eV and d) 2.36 eV.	39
2.4	An example of Babinet's principle for a) a nano-triangle and b) atriangular hole. Similar modes appear for both the positive and hole structure however they appear at different energies. The mode for the positive structure appears at 1.7eV whereas the same mode for the hole is shifted to 2.1 eV.	40
2.5	The a) negative and b) positive nano-swirl structures which are being studied in this work. Each swirl is approximately 60 nm thick and has a diameter of around 500 nm. Deviations in the actual structure, including the surface roughness and edge imperfections are the result of the fabrication process and will be studied in this chapter.	41
2.6	An example of a typical spectrum image obtained using the experimental conditions given in the text, showing a) the 2D spectrum image showing the integrated intensity of the energy loss at each pixel and b) a typical loss spectrum at a single pixel. We can see that the high intensity zero-loss peak dominates the spectrum.	43

2.7	Mean spectrum before (blue curve) and after (red curve) performing Richardson-Lucy deconvolution. The width of the mean zero-loss peak before deconvolution is 0.321 eV and the width after is 0.103 eV. We see after deconvolution the appearance of peaks which were obscured by the zero-loss in addition to some noise at higher energies.	45
2.8	Example showing the four factors found after applying non-negative matrix factorisation on the experimental positive nanoparticle. The black curve is the deconvolved data before the factorization is performed.	46
2.9	The decomposition loadings from the NMF decomposition corresponding to spatial distributions of bound charge on the surface of the positive nanoparticle. The red dashed line indicates the location of the particle boundaries, which have been masked to better show the intensity variations. The energies are a)0.89 eV, b)1.21 eV, c)1.51 eV and d) 2.19 eV.	47
2.10	The decomposition loadings from the NMF decomposition corresponding to spatial distributions of bound charge on the surface of the negative nanoparticle. The energies are a)0.9 eV, b)1.32 eV, c)2.21 eV, d) 2.34 eV and e) 2.45 eV.	49
2.11	a) Regions of the spectrum used in the thickness calculation. b) I_0 : elastic intensity, which includes the zero loss. c) I_{l1} : inelastic region before the loss falls off at as a power-law. d) I_{l2} : To includes losses past the upper cut off of the image a power law is used to extrapolate the region and summed. e) The final values of $\frac{t}{\lambda}$	51
3.1	The gold plasmonic nano-swirl structures which are being studied in this work. Details of each shape are given in the text. Each swirl is approximately 60 nm thick and has a diameter of around 500 nm. Deviations in the actual structure, including the surface roughness and edge imperfections are the result of the fabrication process.	54
3.2	The meshes used for the MNPBEM calculation. The meshes are for a) the devised positive nanoparticle shown in Figure 3.1d and b) the experimental negative nanoparticle shown in Figure 3.1c.	57
3.3	The symmetry allowed modes of the positive ideal structure as calculated from the point group of the structure. Group theory arguments allowed the modes to be determined in terms of an irreducible representation.	62
3.4	The surface charge eigenvectors, σ_k , of the ideal positive plasmonic structure from Figure 3.1a. The colourmap represents the intensity of the surface charge, calculated using Eqn 3.20. Only the real part is shown. (c) and (d) have similar real component however they would differ in imaginary component, as shown in the equations in section 3.4. Similarly with (e) and (f). 64	64

3.5	The surface charge eigenvectors, σ_k , of the experimental positive plasmonic structure from Figure 3.1b. The colourmap represents the intensity of the surface charge, calculated using Eqn 3.20.	66
3.6	Comparison between the ideal (red) and experimentally realistic (blue) eigenvalues. We see a grouping of the eigenmodes in clusters of similar eigenvalues. We can also see a shift in eigenvalue between the ideal and actual eigenvalues, suggesting a shift in energy.	67
3.7	The surface charge eigenvectors, σ_k , of the devised positive plasmonic structure from Figure 3.1d. The colourmap represents the intensity of the surface charge, calculated using Eqn 3.20.	70
3.8	The surface charge eigenvectors, σ_k , of the negative plasmonic structure from Figure 3.1c. The colourmap represents the intensity of the surface charge, calculated using Eqn 1.3 from the previous chapter. The modes are ordered in order of increasing eigenvalue.	72
3.9	Comparison between the devised positive and experimentally realistic negative nanoparticle's eigenvalues. We see a grouping of the eigenmodes in clusters of similar eigenvalues. We can also see a shift in eigenvalue between the two nanoparticle's eigenvalues, suggesting a shift in energy.	73
3.10	Inset: The impact positions for the electron beam, chosen on the ideal particle from Figure 3.1a. Graph: EELS spectrum for the ideal particle the beam positions indicated with circles in the top panel. In the simulations we assume a kinetic electron energy of 200 keV.	74
3.11	Spatial EELS maps corresponding to the peaks in Figure 3.10 for the ideal particle in Figure 3.1a. The modes (a) and (b) appear to be a single broader mode, as the spatial intensity only slightly changes radially outward from the central region.	75
3.12	Inset: The impact positions for the electron beam, chosen on the experimental particle from Figure 3.1b. Graph: EELS spectrum for the experimental particle obtained at the beam positions indicated with circles in the top panel. In the simulations we assume a kinetic electron energy of 200 keV.	76
3.13	Spatial EELS maps corresponding to the peaks in Figure 3.12 for the experimental particle in Figure 3.1b.	77
3.14	Top: The impact positions for the electron beam, chosen on the devised particle from Figure 3.1d. Bottom: The loss maps corresponding to each impact parameter.	78
3.15	Spatial EELS maps corresponding to the peaks in Figure 3.14 for the actual particle in Figure 3.1d.	79
3.16	Spatial EELS maps corresponding to the experimental negative particle in Figure 3.1c.	80

3.17	Z- component of E field around the ideal nanoparticle, calculated using an eigenmode expansion. Symmetry terms are used to quantify the loss and group similar terms.	82
3.18	Z- component of E field around the experimentally realistic nanoparticle, calculated using an eigenmode expansion. Symmetry terms are used to quantify the loss and group similar terms.	83
3.19	The surface charge eigenvectors, σ_k , of the ideal positive plasmonic structure from Figure 3.1d, with a substrate added. The colourmap represents the intensity of the surface charge, calculated using Eqn 3.20.	86
3.20	Comparison between the ideal and ideal with substrate eigenvalues. We see a grouping of the eigenmodes in clusters of similar eigenvalues, with only slight shifts in energy shifts until higher order modes.	87
3.21	Z- component of E field around the ideal nanoparticle, calculated using an eigenmode expansion. Symmetry terms are used to quantify the loss and group similar terms.	89
4.1	a) Conventional diffraction compared with b) convergent beam electron diffraction (CBED) from a bcc iron crystal oriented along the 100 direction. In conventional diffraction the pattern is made up of sharp spots, whereas in CBED these spots form disks which can overlap.	93
4.2	The conventional set up for CBED. In this setup an electron beam originating from point P in the incident beam, will find itself scattered to point P' in the diffraction disks. By adding a phase term to the incident beam (as in a vortex beam) we would expect to see the interference effects in the region where the phase difference is most prominent, this would be in the region of overlap between two disks, as seen in the figure.	94
4.3	Diffraction patterns for two opposite handed vortex beams a) =+1 and c) =-1 and c) a Gaussian beam scattering from an achiral bcc iron crystal. The beam energy is 200keV. d-f) show a convergence angle of 6mrad and g-i) the convergence angle is 8mrad. The diffraction patterns are calculated after scattering through 10 unit cells. The simulation was run with 1024×1024 pixels, with real space dimensions of $28.59 \times 28.59 \text{ \AA}$. The intensity scaling in each of the diffraction patterns is the same.	95
4.4	The overlap of the vortex beam probability density with the square chiral potential, looking down the beam direction. The donut shaped intensity is chosen to lie directly over the fourfold helix, this results in overlapping diffraction disks. The radius of the probe is around 1.5 \AA	97

- 4.5 Set up of the simulation for a square chiral crystal showing the (a) plus vortex beam wavefront, (b) minus vortex beam wavefront. (c)-(d) show the entrance face of the crystal viewed along the beam direction. (e)-(f) show the atomic positions within the unit cell. 98
- 4.6 CBED diffraction pattern corresponding to the probability densities shown in Figure 4.7. The differences are shown for a $l=+1$ (left), $l=0$ (middle) and $l=-1$ vortex beam (right) scattering through a left (top) and right (bottom) handed crystal. Notice that several features match between the figures in opposite corners. The thickness of the crystal is 140nm. The simulation was run with 1024×1024 pixels, with real space dimensions of $57.18 \times 57.18 \text{ \AA}$. The beam energy was 200keV and a convergence angle of 6mrad. 99
- 4.7 Exit wave probability densities for a $l=+1$ (left), $l=0$ (middle) and $l=-1$ (right) vortex beam scattering through a left (top) and right (bottom) handed crystal. Notice that the intensity distribution within the central disk matches between the figures in opposite corners. The thickness of the crystal is 140nm. The simulation was run with 1024×1024 pixels, with real space dimensions of $57.18 \times 57.18 \text{ \AA}$. The beam energy was 200keV and a convergence angle of 6mrad. 100
- 4.8 Exit wave probability densities for a $l=+1$ (left) and $l=-1$ vortex beam (right) scattering through a left (top) and right (bottom) handed crystal. Note the similarities of the pattern from beams of the same sign. Features are dominated by the vortex beam sign. The thickness of the crystal is 28nm. The simulation was run with 1024×1024 pixels, with real space dimensions of $57.18 \times 57.18 \text{ \AA}$. The beam energy was 200keV and a convergence angle of 6mrad. 102
- 4.9 CBED diffraction pattern corresponding to the probability densities shown in Figure 4.8. The differences are shown for a $l=+1$ (left) and $l=-1$ vortex beam (right) scattering through a left (top) and right (bottom) handed crystal. The vortex beam sign is the dominant feature in the patterns. The thickness of the crystal is 28nm. The simulation was run with 1024×1024 pixels, with real space dimensions of $57.18 \times 57.18 \text{ \AA}$. The beam energy was 200keV and a convergence angle of 6mrad. 103
- 4.10 CBED patterns for scattering from a thin square chiral crystal. The thickness of the crystal is 28nm. The simulation was run with 1024×1024 pixels, with real space dimensions of $57.18 \times 57.18 \text{ \AA}$. The beam energy was 60keV and a convergence angle of 11.64mrad. 104
- 4.11 Exit wave diffraction patterns for a square chiral crystal. The thickness of the crystal is 11nm. The simulation was run with 1024×1024 pixels, with real space dimensions of $57.18 \times 57.18 \text{ \AA}$. The beam energy was 10keV and a convergence angle of 19.46mrad. 105

4.12	Exit wave diffraction patterns for a square chiral crystal. The thickness of the crystal is 11 nm. The simulation was run with 1024×1024 pixels, with real space dimensions of $57.18 \times 57.18 \text{ \AA}$. The beam energy was 10 keV and a convergence angle of 29.19 mrad . Differences are now more apparent in the region of overlap.	106
4.13	The overlap of the vortex beam probability density with the hexagonal chiral potential, looking down the beam direction. The donut shaped intensity is chosen to lie directly over the sixfold helix, this results in overlapping diffraction disks.	107
4.14	CBED patterns from scattering with the hexagonal crystal. The thickness of the crystal is 9 nm. The simulation was run with 1024×1024 pixels, with real space dimensions of $49.6 \times 49.6 \text{ \AA}$. The beam energy was 10 keV and a convergence angle of 35.26 mrad	108
4.15	Set up of the simulation for a hexagonal chiral crystal showing the (a) plus vortex beam wavefront, (b) minus vortex beam wavefront. (c)-(d) show the entrance face of the crystal viewed along the beam direction. (e)-(f) show the atomic positions within the unit cell.	109
4.16	Probability densities for scattering from a hexagonal chiral crystal. The thickness of the crystal is 9 nm. The simulation was run with 1024×1024 pixels, with real space dimensions of $49.6 \times 49.6 \text{ \AA}$. The beam energy was 10 keV and a convergence angle of 35.26 mrad	110
4.17	CBED diffraction patterns for scattering from a hexagonal chiral crystal. The thickness of the crystal is 47 nm. The simulation was run with 1024×1024 pixels, with real space dimensions of $49.6 \times 49.6 \text{ \AA}$. The beam energy was 200 keV and a convergence angle of 7.24 mrad	111
4.18	Probability densities for scattering from a hexagonal chiral crystal. The thickness of the crystal is 47 nm. The simulation was run with 1024×1024 pixels, with real space dimensions of $49.6 \times 49.6 \text{ \AA}$. The beam energy was 200 keV and a convergence angle of 7.24 mrad	111
4.19	Integrated intensities of a) $l = +1$ b) $l = 0$ and c) $l = -1$ electron beam scattering through both a clockwise and anticlockwise sixfold screw axis arrangement of iron atoms.	113
4.20	The unit cells of α Quartz showing the two different chiral configurations (a) L-Quartz with contains a left handed screw axis and (b) D-Quartz which contains a right handed screw axis when looking down the 001 direction.	114
4.21	The overlap of the vortex beam probability density on the quartz chiral potential, looking down the beam direction. The donut shaped intensity is chosen to lie directly over the screw axis of the crystal, this results in overlapping diffraction disks.	115

- 4.22 CBED patterns for alpha quartz. The thickness of the crystal is 10nm. The simulation was run with 1024×1024 pixels, with real space dimensions of $40 \times 40 \text{ \AA}$. The beam energy was 10keV and a convergence angle of 29.79mrad . The crystals are related to each other by being mirrored along the z-direction. 115
- 4.23 Quartz positions before and after permuting the layers. We see that by keeping the first layer constant and permuting the other layers such that $2 \rightarrow 9, 3 \rightarrow 8$ and so on, we transform one crystal into the other. 116
- 4.24 CBED patterns from alpha quartz. The thickness of the crystal is 10nm. The simulation was run with 1024×1024 pixels, with real space dimensions of $40 \times 40 \text{ \AA}$. The beam energy was 10keV and a convergence angle of 29.79mrad . The crystals are related to each other by a mirror plane perpendicular to the page. 117
- 4.25 CBED patterns from alpha quartz. The thickness of the crystal is 10nm. The simulation was run with 1024×1024 pixels, with real space dimensions of $40 \times 40 \text{ \AA}$. The beam energy was 10keV and a convergence angle of 29.79mrad . The crystals are related to each other by being mirrored along the z-direction and a shift in the beam position. 117
- 4.26 The unit cells of $Cr_{\frac{1}{3}}NbS_2$ showing the two different chiral configurations where the silicon atoms, shown in yellow, form a a) clockwise and (b) anticlockwise crystal when viewed along the c-axis. 118
- 4.27 The overlap of the vortex beam probability density with the $Cr_{\frac{1}{3}}NbS_2$ potential, looking down the beam direction. The donut shaped intensity is chosen to lie directly over the silicon atoms which form the screw axis, which results in overlapping diffraction disks. 119
- 4.28 CBED patterns. The thickness of the crystal is 12nm. The simulation was run with 1024×1024 pixels, with real space dimensions of $45.91 \times 45.91 \text{ \AA}$. The beam energy was 10keV and a convergence angle of 29.79mrad 119

List of tables

3.1	The character table for the point group C_{6h} , where $\varepsilon = \exp(i\pi/3)$	59
3.2	SALCs for the point group C_{6h}	60
3.3	The character table for the irreducible representation, where $\varepsilon = \exp(i\pi/3)$	61
3.4	The calculated dipole moment for the eigenmodes of the ideal and actual nanoparticle.	68
3.5	The change in E field chirality between an ideal and experimentally realistic plasmonic nanoparticle.	84
3.6	The calculated dipole moment for the eigenmodes of the ideal nanoparticle with and without a substrate.	85
3.7	The calculated E field chirality for the eigenmodes of the ideal nanoparticle with and without a substrate.	88

Chapter 1

Introduction

1.1 Overview

This thesis will explore the use of electrons as probes of chiral materials and will develop two main themes. The first is the use of electrons as probes of matter, specifically in electron microscopes. The second is chirality and the means of observing and characterising chiral structures. This chapter will introduce the concepts required to understand the natural choice of electrons as probes of matter for the topics discussed in our work. We will start by introducing what information can be obtained when using electrons to probe samples and why the need for electrons as probes arises. We will then outline the formation of electron beams, as found in electron microscopes, and what properties of these beams will be important for the results found in later chapters. The concepts developed in this chapter will include the importance of a bright source of electrons, the wavelength of electrons and how this varies in an electron microscope, the concept of electron coherence, the mechanics of how electrons interact with matter and modern electron microscopy instrumentation. We will highlight the different types of information which can be obtained using various electron microscopy instrumentation, each of which relies on a different fundamental interaction which an electron can have with a specimen. We will complete this chapter with a discussion of crystal chirality, how electrons interact with chiral materials in an electron microscope and the limitations of this technique when observing chirality. We will also introduce a chiral electron probe and discuss how the phase profile of electron vortex beams effectively alters forward scattering through a chiral sample. Results shown in this chapter highlight the importance in the choice of beam position on the unit cell of a crystal. When the beam is positioned along an atomic column we observed electron channelling, where the beam was focused towards the centre of the column as it propagated through the crystal. We also show towards the end of this chapter simulated wavefunctions and probability densities of vortex beams. These have been derived during this work by modifications of existing electron microscopy simulation tools.

1.2 Free Electron Beams

The discovery of electrons by J. J. Thomson in 1897 not only led to a fundamentally new understanding of physics but also enabled scientists to produce and manipulate free electrons in beams, which in turn led to the development of electron microscopy. In this work we will exploit some of the unique properties of electrons and how they scatter and interact with samples. Much of the rationale for using electrons as probes will centre on a need for higher resolution, which is ultimately limited by the electron's de-Broglie wavelength.

1.2.1 Electron Wavelength

In 1925 de Broglie's hypothesis of electron wave-particle duality [4] led to the introduction of the de-Broglie wavelength of electrons, λ_B . For electrons accelerated by a potential difference, V , the relativistic de-Broglie wavelength (Eqn 1.1) can be calculated as,

$$\lambda_B = \frac{h}{(2m_0eV(1 + \frac{eV}{2m_0c^2}))^{1/2}} \quad (1.1)$$

where m_0 is the rest mass, e is magnitude of the charge of an electron and h is Planck's constant. If we take the electrons described in the following chapters, the instruments were operated at an acceleration voltage of 200 keV. Using a rest mass energy of 0.511 MeV, this gives a de-Broglie wavelength of $\lambda_B = 2.5$ pm or 2.7 pm without relativistic correction. This gives a theoretical resolution of subatomic scale. However it is important to note that this resolution is not achievable in current electron microscopes, although 20 pm resolution has been reported in the current literature [5]. In contrast the wavelength of visible light is in the region of 500 nm, which, due to the diffraction limit, means the best resolution of traditional optical microscopes is around 250 nm [6]. The resolution of an electron microscope is not diffraction limited but instead is limited by the instrument itself, in the form of lens defects, source resolution and scattering effects. These concepts will be explored further in later sections.

The first working electron microscope by Knoll and Ruska demonstrated that, just as in an optical microscope where light is focused into a beam, electrons emitted from an electron source could be focused into an electron beam using magnetic lenses. This microscope also produced the first image taken with electrons and was the starting point of the field of electron microscopy. Then, in 1933, Ruska showed that an electron microscope could obtain images at a higher resolution than an optical microscope showing the importance of electron beams as probes of matter. With better instruments, the performance of electron microscopes gradually improved towards the goal of subatomic resolution. In 1949 Heidenreich showed that thin films were electron transparent, thus leading to the invention of the transmission electron microscope (TEM). Historically TEMs were used only to study two elastic signals, that of the direct and diffracted beams. This meant that a large quantity of information was

being thrown away. Modern TEMs are complicated instruments which have a multitude of components, each of which can be used to perform a different analysis of a sample and can detect information carried by the electrons. Thus modern TEMs, and their ability to study a range of different processes which result from the interaction of electron beams with matter, further support the use of electrons as probes of matter. Some of these interactions will now be discussed in the next section, with their applications in a transmission electron microscope discussed in the following sections.

1.2.2 Electron Matter Interactions

Electrons interact with the atoms of a sample through electrostatic (Coulomb) forces. This interaction can take one of many forms and Figure 1.1a shows some of the possible interactions which can occur between a beam of fast electrons (typical energy of hundreds of keV) with matter. If the sample is sufficiently thin (in the region of tens of nanometers), then it can be considered a thin film, and most of the electrons will be transmitted through. These, so called, forward scattered electrons are usually the ones observed in a TEM. Electrons may also be scattered back in the beam direction, either as backscattered electrons from the incident beam or via the production of secondary electrons. These electrons are not usually observed in a TEM unless a detector is placed before the sample and their absence from our electron simulations will be discussed in Section 1.8.

The forward scattered electrons can interact with atoms in the solid, either with the nuclei or the electrons. Thus, there are two types of interaction which can occur when an electron beam interacts with the sample. The first is *elastic scattering*. This occurs when an electron in the beam interacts with the electrostatic field around the dense positive charge of the atomic nuclei. If electrons pass close to the nuclei they will be deflected through a large angle, with electrons deflected by over 90° said to be backscattered. The vast majority of electrons however will not pass by the nuclei at such a close distance, and thus will only be slightly deflected by an amount of only a few milliradians [7]. Although the term elastic scattering implies no energy change, due to a change in momentum the electrons can experience a slight change in energy, which is small in comparison to other scattering events, less than 1 eV.

The second type of interaction which can occur is *inelastic scattering* where the incident electrons in the beam excite processes such as electronic promotion or phonons. If this interaction occurs with inner, tightly held, shell electrons, due to the increased energy required to excite these electrons to an outer shell, the deflection angle will be larger than those of an interaction with outer shell electrons. This energy can be in the region of hundreds of electron volts [8]. The transfer of energy from the incident electrons to the sample leaves it in an excited state, and the electrons excited to a higher energy level may subsequently de-excite, leading to the emission of electromagnetic radiation or a secondary electron. This radiation will most likely be in the form of x-rays.

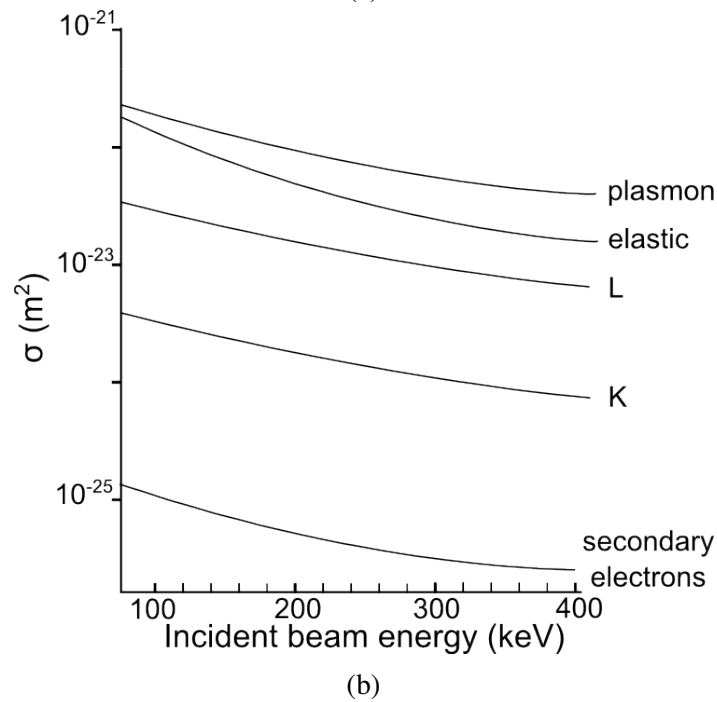
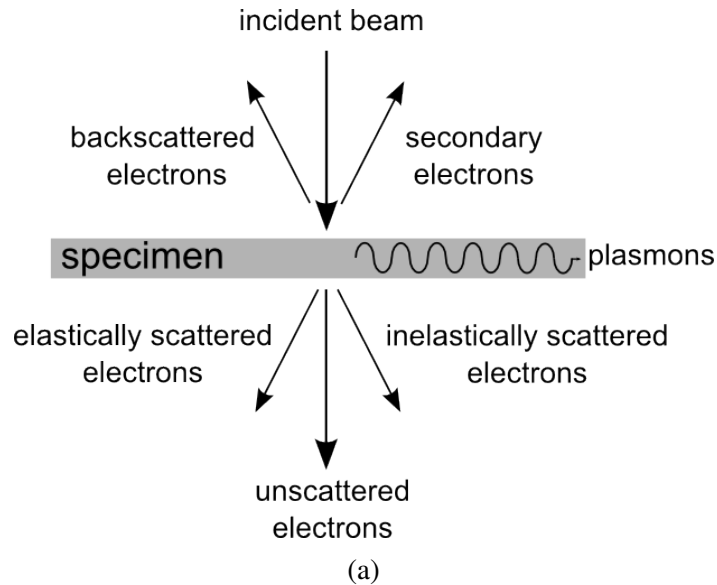


Fig. 1.1 a) Diagram showing the various ways an electron beam can interact with a specimen. b) Graph showing the cross sections for some of the interactions shown in a). The graph shows that losses leading to the generation of plasmons have the highest cross section, followed by elastic losses. K- and L-shell ionisation is less likely and even less likely is the generation of secondary electrons. Adapted from Williams and Carter [1].

A probing electron can also excite more than just a single outer-shell electron, it can excite a number of valence electrons at the same time. This collective excitation of valence electrons is known as a *plasmon* and takes the form of a longitudinal traveling wave. Such excitations are common in most materials and the energy transferred between an incident electron and a plasmon is around $5 - 30\text{eV}$. A plasmon as described above is a collective oscillation in the bulk of a material, however such an excitation can exist purely on the surface of a material. Thus we shall differentiate between *bulk plasmons* and *surface plasmons*, the latter of which will be discussed in more detail in Section 1.3

The probability of an incident electron undergoing a particular scattering event with an atom in the solid is governed by an interaction *cross section*, usually denoted σ . Every type of interaction has a particular cross section, which is dependent on the energy of the incident beam and is an effective area which quantifies the probability of that event occurring. This means the higher the cross section, the more likely that scattering event will occur. Elastic scattering usually has a higher cross section than inelastic events, with the exception of plasmon losses, which have the highest cross section as shown in Figure 1.1b. The total cross section, σ_T , for a particular atom is the sum of the inelastic and elastic cross sections as we consider the two different types of scattering separately. If we consider the number of atoms per unit volume in a sample we can define the cross section in terms of this volume as

$$N\sigma_T = \frac{N_0\sigma_T\rho}{A}, \quad (1.2)$$

where A is the atomic weight N_0 is Avogadro's constant, $6.022 \times 10^{23} \text{ mol}^{-1}$, and N is the total number of atoms. As the angle of scattering is an important quantity when studying how electrons scatter its also important to understand the concept of the *differential cross section*. The differential cross section, $\frac{d\sigma}{d\Omega}$ is a measure of the angular distribution of scattering, where Ω is the angular span of a detector. While the interaction cross section only decreases the likelihood of an event occurring, the differential cross section tells you the likelihood of that event occurring for a given angle of scattering. Figure 1.1b shows the interaction cross section for a number of different electron scattering events. We see that the most likely interaction an incident electron can have with a specimen is through the production of a plasmon. Second most likely is for the incident electron to undergo an elastic scattering event, followed by inelastic events, K- and L- ionization are shown on the graph. Production of secondary electrons is less likely and thus has the lowest cross section. It should be noted from the graph that the likelihood of a particular scattering event occurring is less dependent on the energy of the beam at energies in the region of hundreds of *keVs*.

Up until now we have considered an electron in the beam having an individual interaction with an atom in a solid, however multiple scattering events can occur and, due to the wave nature of electrons, interference can occur. This will be discussed in the next section.

1.2.3 Electron Coherence and Diffraction

In order to discuss interference effects that can occur when electrons interact with a solid we must first discuss the concept of electron coherence. Coherence is a measure of the ability of electrons in a beam to interfere with one another and cause interference effects. A beam of coherent electrons will all have a constant phase relation and a constant wavelength, governed by the source (electron gun as discussed in Section 1.4.1). Similarly, if a scattering event creates coherent electrons then they will all share a similar wavelength. Due to the wave nature of electrons we have discussed in Section 1.2 an electron wavelength, we can now also think about an electron phase. This allows us to split scattering electrons into *coherent* and *incoherent*, which describes their phase in relation to one another. The scattering events discussed in Section 1.2.2 were grouped as elastic and inelastic. Elastically scattered electrons are usually coherent and inelastically scattered electrons are usually incoherent. This means if a set of electrons undergo different inelastic scattering events then they may have no relationship between their phases. Due to the lower scattering cross sections for inelastic scattering events at the typical energies of a TEM, these scattering events are usually ignored when studying diffraction or considered to be an absorption effect. However elastic scattering events will generate scattered electrons which scatter with similar wavelengths thus interference effects between the different electrons can produce information about the sample. Thus we have a measure of a source of electrons, which we call *temporal coherence*, which is a measure of how in phase emitted electrons are from a source. For a source of electrons which has an energy spread ΔE we can define a coherence length, λ_c defined as,

$$\lambda_c = \frac{v h}{\Delta E}, \quad (1.3)$$

where v is the electron velocity. This means that a smaller energy spread will lead to a more coherent beam as one would expect. In practice it is impossible to have a perfectly monochromatic source of electrons however recent advances have come close [9]. This will be further explored in Section 1.4.1, when we look at sources of electrons.

We have seen in the previous sections that we can describe an electron with a wavelength and a phase, due to their wave nature. We can now discuss the concept of diffraction of electrons. After the wave nature of electrons was developed, Davidson and Germer verified this concept with the first observation of electron diffraction using 54 eV electrons reflected from nickel [10]. If we define an amplitude, Ψ_0 and a phase ϕ , then we can write the electron beam in the form of a wavefunction,

$$\Psi = \Psi_0 e^{i\phi}. \quad (1.4)$$

We discussed the need for coherence if interference effects are to occur between electrons and we can take this idea further by expressing the path difference between electrons and apply Bragg's law. In a crystal, the atomic layers form a periodic lattice, made up of repeating unit

cells. We can use scattering within this unit cell to describe the entire lattice by introducing a structure factor, $F(\theta)$. The structure factor describes the diffracted wave and is thus a complex number with amplitude and phase defined as,

$$F(\theta) = \sum_j f_j(\theta) \exp(-i\mathbf{p} \cdot \mathbf{r}_j), \quad (1.5)$$

where f_j is the scattering amplitude and \mathbf{r}_j the position of atom j and \mathbf{p} is the scattering vector. The sum is over all atoms in the unit cell, and $\mathbf{p} \cdot \mathbf{r}_j$ is the phase. $F(\theta)$ is a measure of the amplitude of the scattered electron. The scattered intensity in any direction θ is given by $|F(\theta)|^2$ and has a sinusoidal amplitude, peaking where the scattered waves are in phase. Each maximum in the intensity can be considered to be a reflection from atomic planes. The spacing of these atomic planes depends on the Miller indices and unit cell dimensions. Bragg reflections occur when the angle between the incident beam and the diffraction planes coincides with a Bragg angle, θ_B such that,

$$n\lambda = 2d \sin \theta_B. \quad (1.6)$$

Figure 1.2a shows an incident plane wave scattered by an atomic column. The two scattering vectors k_i and k_s can be represented on the reciprocal lattice as shown in Figure 1.2b. All vectors k_s which add up constructively with the incident vector k_i will lie on a sphere in reciprocal space. This sphere is called the Ewald sphere [11] and has a radius of $\frac{1}{\lambda}$. Thus at the high incident energies found in a TEM the sphere will appear flat and planes of points in the reciprocal lattice will all lie on the Ewald sphere. This is shown in Figure 1.2c. These planes will appear in the diffraction pattern as the zero-order (ZOLZ), first-order (FOLZ), second-order (SOLZ) and higher-order (HOLZ) Laue zones. In many standard experiments, only the ZOLZ spots are readily observed, which implies that structural information along the beam direction is lost and that only a two-dimensional projection of a sample contributes to the diffraction or, indeed, to images. In many standard experiments, only the ZOLZ spots are readily observed, which implies that structural information along the beam direction is lost. Only a two-dimensional projection of a sample contributes to the diffraction or, indeed, to images. As most chiral crystals will appear similar when projected onto a 2D plane this usual makes them indistinguishable in diffraction patterns. An aspect of diffraction that will be of interest in this work is Friedel's law [12]. Friedel's law was introduced as an empirical rule for diffraction of X-rays by crystals. It states that diffraction effects in a crystal are invariant under inversion of the crystal (with respect to the incident beam). In other words the two reflections (hkl) and $(\bar{h}\bar{k}\bar{l})$ will have equal intensities in the diffraction pattern of a crystal. Friedel's law can be derived from the kinematical theory of diffraction. It is Friedel's law which makes probing chiral materials with conventional electron microscopy difficult. However, Friedel's law only applies to diffraction of planewaves, which allows electron vortex beams to break Friedel's law.

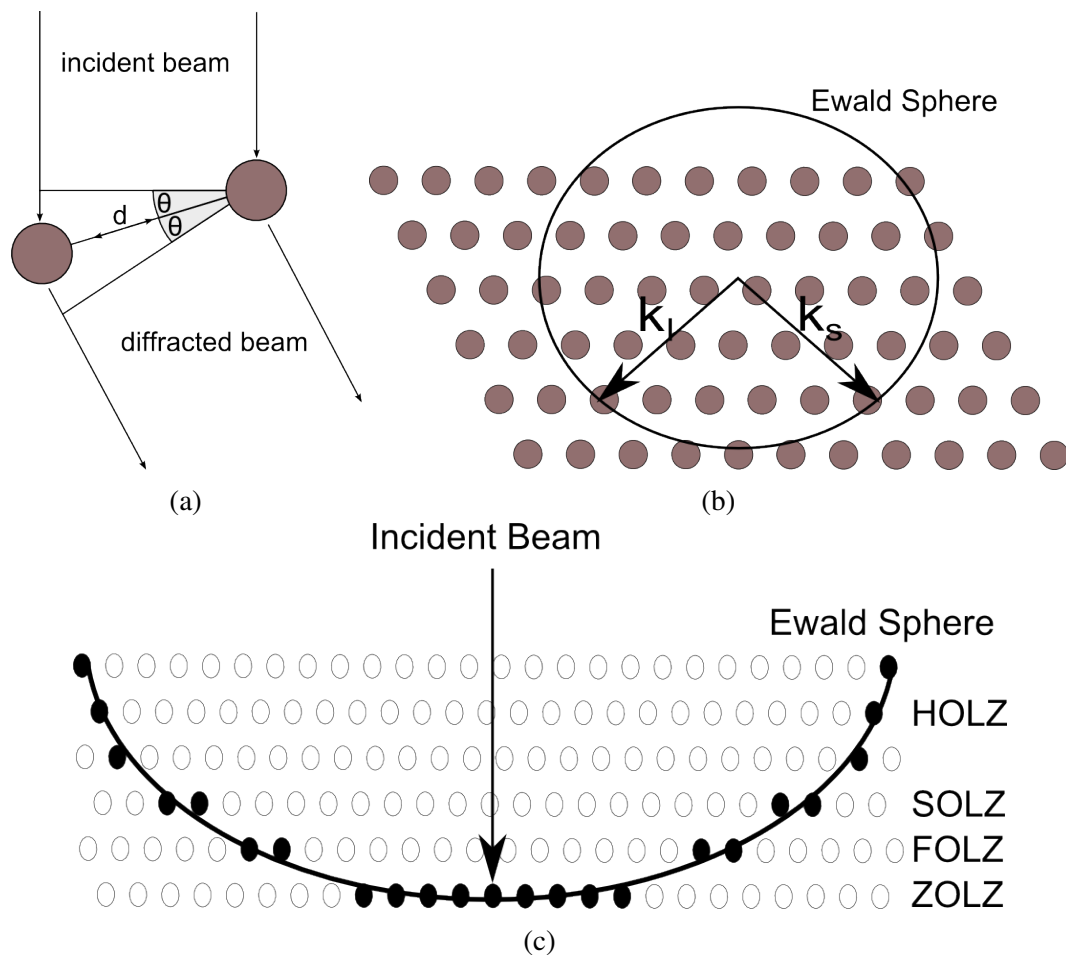


Fig. 1.2 The mechanics of electron diffraction. a) A plane wave electron beam is scattered by a column of atoms by an angle θ . b) The scattered and incident beams, k_s and k_i , can be visualised in reciprocal space using the concept of the Ewald Sphere. c) Using the points where the Ewald Sphere touches the reciprocal lattice allows us to see the zero-order Laue zones (ZOLZ) and higher-order Laue zones (HOLZ).

1.2.4 Electron Channelling

When an electron propagates through a periodic crystal its wavefunction will often have a similar intensity to the periodic potential it is scattering through. This is due to the evolving probability current as the electron propagates through the crystal. Solutions to the time-independent Schrodinger equation are in the form of Bloch waves: plane waves with a modulated amplitude that matches the periodic potential. The propagating electrons in the material are then described as a sum of Bloch waves. A Bloch wave which has intensity peaked at an atomic column will exhibit a higher kinetic energy and the overall distribution of the electron wavefunction will be focused around the atomic column. Periodic focusing of the electron's wavefunction about successive atomic cores as it propagates through the crystal is known as *electron channelling*. This effect is important when using a focused beam of electrons, as is shown in Figure 1.3. When a Gaussian plane wave is focused onto a spot which has dimensions smaller than the unit cell of a crystal then the beam can be positioned to align either along an atomic column or between them. If the beam is placed on an atomic column as shown in Figure 1.3 a then the beam will be channeled quicker than when it is positioned between two atomic columns, as in Figure 1.3b. This is shown by the sharp central spot which appears in Figures 1.3d, 1.3g and 1.3j whereas in Figures 1.3e, 1.3h and 1.3k there is still a high intensity region between the two columns as well as on each of the atomic sites. The free space beam is shown in Figures 1.3c, 1.3f, 1.3i and 1.3l to show that the beam maintains its shape when no periodic potential is present. It is important to note that this channelling effect can occur over just a few unit cells. This will be important in the later chapter on vortex beams, as we will be positioning a probe on a unit cell and it is important to know at which depth our wavefunction no longer resembles the entrance wavefunction.

1.3 Surface Plasmons

Electrons can also interact with matter to create plasmons, the excitation of which was shown in Figure 1.1 to dominate electron scattering in typical samples. Surface plasmons are a collective electromagnetic excitation which can exist on the surface of a conductor, or at its interface with a dielectric [13]. SPs are the result of the interaction between the free electrons in the conductor and an external electric field, usually produced by a photon or an incident electron [14]. The free electrons in a metal are able to respond to the incident radiation, specifically to the AC field of an incident photon or the time dependent electrostatic field of a propagating electron. As this is an electrodynamic problem to define the properties of SPs we must apply Maxwell's Equations to this interface. Maxwell's equations can be written as

$$\nabla \cdot \mathbf{D} = 0, \quad (1.7)$$

$$\nabla \cdot \mathbf{B} = 0, \quad (1.8)$$

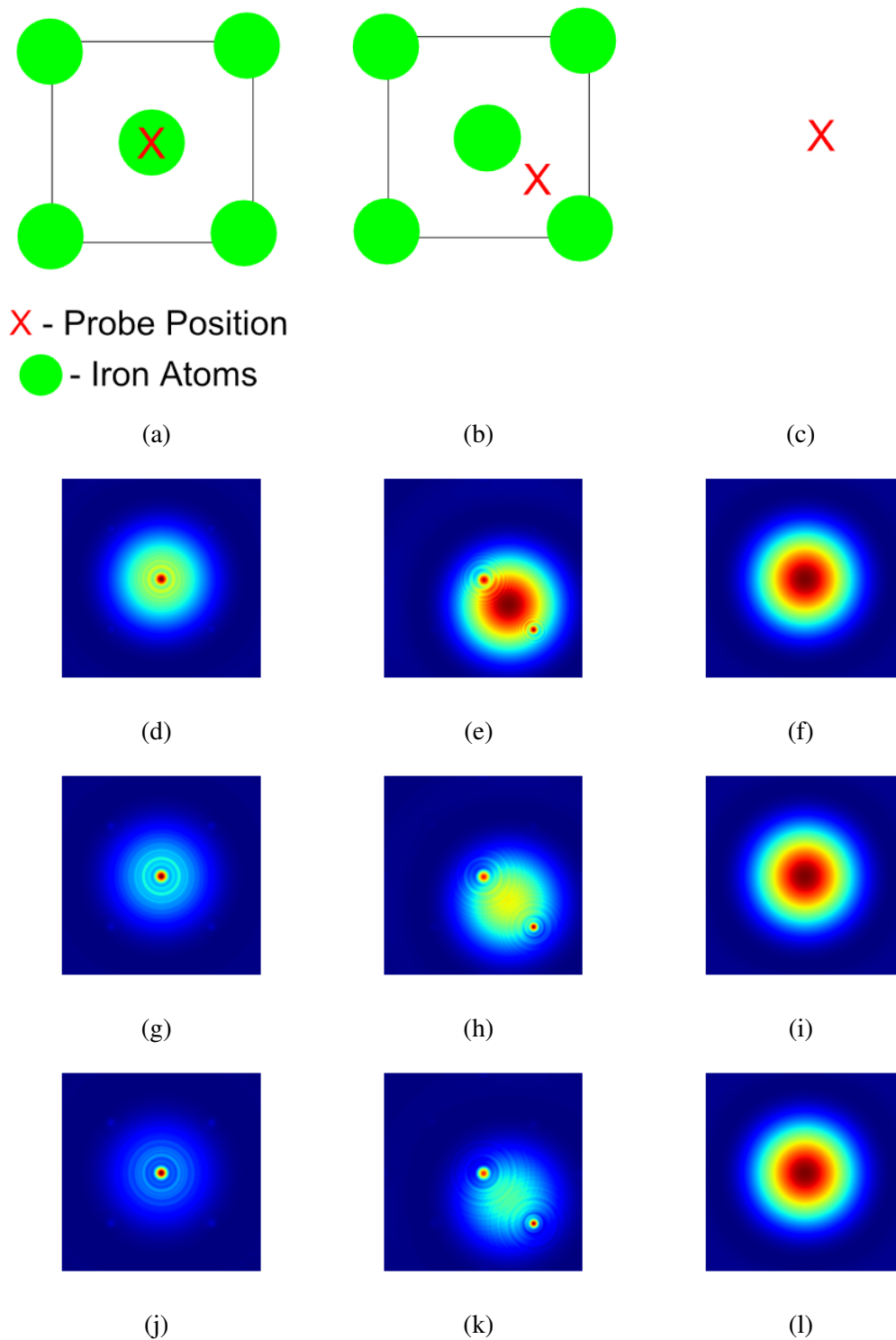


Fig. 1.3 Simulated wavefunctions for a planewave electron beam focused at different points on the unit cell of iron. For a beam positioned (a) on an atomic column, (b) between two atomic columns and (c) in free space. The wavefunctions after (d,e,f) 1 unit cell (g,h,i) 2 unit cells and (j,k,l) 3 unit cells are shown. The on column beam channels quicker than that positioned between columns. Over this distance the beam in free space does not change.

$$\nabla \times \mathbf{E} = -\frac{\partial \mathbf{B}}{\partial t}, \quad (1.9)$$

and

$$\nabla \times \mathbf{H} = \mathbf{J}_{\text{ext}} + \frac{\partial \mathbf{D}}{\partial t}. \quad (1.10)$$

In these equations the four macroscopic fields are \mathbf{D} (the dielectric displacement), \mathbf{E} (the electric field), \mathbf{H} (the magnetic field), and \mathbf{B} (the magnetic induction or magnetic flux density) with the external charge and current densities given by ρ_{ext} and \mathbf{J}_{ext} respectively. Equations 1.9 and 1.10 can be combined, in the absence of external charge ($\rho_{\text{ext}} = 0$) and current densities ($\mathbf{J}_{\text{ext}} = 0$), and assuming a linear, isotropic, homogeneous, non magnetic material ($\mu = 1$) to give,

$$\nabla \times \nabla \times \mathbf{E} = -\mu_0 \frac{\partial^2 \mathbf{D}}{\partial t^2}. \quad (1.11)$$

Where we have used the relation $\mathbf{B} = \mu\mu_0\mathbf{H}$, and μ and μ_0 are the relative permeability of the material and absolute permeability of vacuum respectively. Using the relationship $\nabla \times \nabla \times \mathbf{E} = \nabla(\nabla \cdot \mathbf{E}) - \nabla^2 \mathbf{E}$ leads to the equation

$$\nabla(\nabla \cdot \mathbf{E}) - \nabla^2 \mathbf{E} = -\mu_0 \frac{\partial^2 \mathbf{D}}{\partial t^2} \quad (1.12)$$

$$\nabla^2 \mathbf{E} - \frac{\epsilon}{c^2} \frac{\partial^2 \mathbf{E}}{\partial t^2} = 0. \quad (1.13)$$

Where equation 1.13 is the wave equation of electromagnetic theory and we have used the relations $\mathbf{D} = \epsilon_0 \epsilon \mathbf{E}$ and $c^2 = \frac{1}{\mu_0 \epsilon_0}$, where c is the speed of light, ϵ and ϵ_0 are the relative permittivity (or dielectric constant) of the material and of vacuum respectively. If we assume \mathbf{E} has a harmonic time dependence, such that we can write $\mathbf{E}(\mathbf{r}, t) = \mathbf{E}(\mathbf{r})e^{-i\omega t}$, then equation 1.13 becomes,

$$\nabla^2 \mathbf{E} + k_0^2 \epsilon \mathbf{E} = 0 \quad (1.14)$$

where $k_0 = \frac{\omega}{c}$. This is the Helmholtz equation which we can use to solve Maxwell's equations and will find that our solutions at the boundary are in the form of surface plasmons. Figure 1.4b shows the directions of the fields at the interface of a dielectric and metal as detailed in the equations above.

1.3.1 Propagating Surface Plasmons

Propagating surface plasmons are electromagnetic excitations which propagate along the interface of a metal and dielectric medium. Propagating surface plasmons can be excited in thin films [15], linear chains of nanoparticles [16] and nanoholes in a metallic medium [17]. To derive the surface plasmon conditions we will consider the interface between two semi-infinite non magnetic media, with local dielectric functions ϵ_1 and ϵ_2 . The interface is shown as $z = 0$ in Figure 1.4, where $z > 0$ is the dielectric and $z < 0$ is the metal. We consider

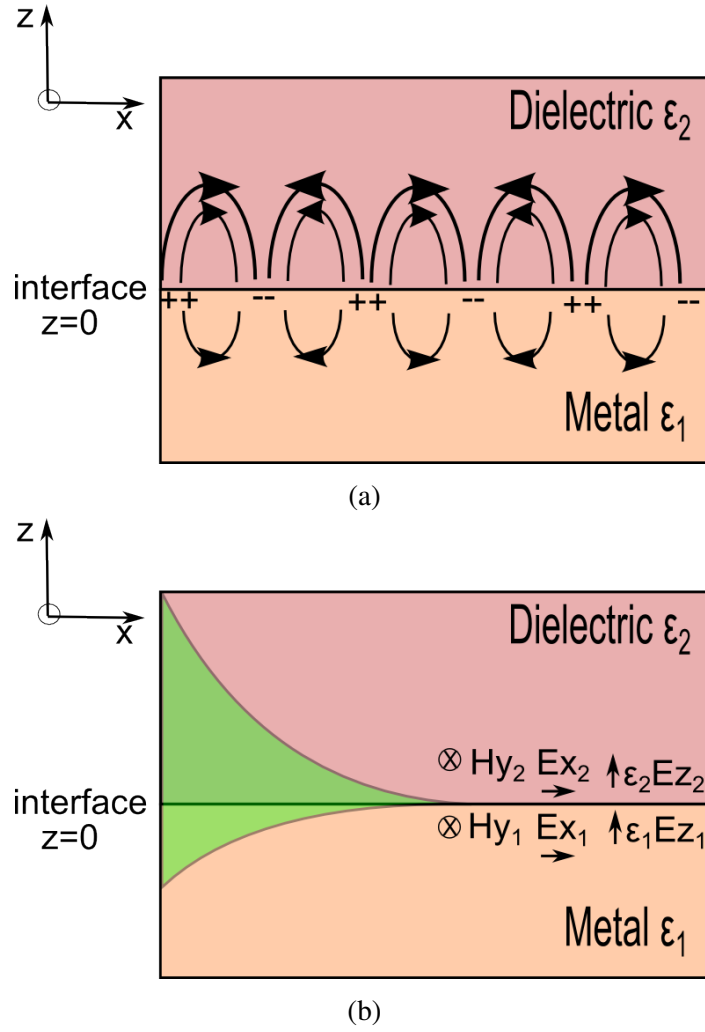


Fig. 1.4 (a) Propagating surface plasmon at the interface between a dielectric and a metal. The arrows indicate the electric field at the interface. The surface plasmon is an electromagnetic excitation which propagates along the interface, in the x direction b) The field caused by the surface plasmon has an exponential decay shown in green, this decay happens faster in the metal than in the dielectric. This results in the enhanced near field applications of surface plasmons.

a field which propagates along the x direction, which has components,

$$\mathbf{E}_i = (E_{ix}, 0, E_{iz})e^{i(k_x x - \omega t)} e^{\pm k_{zi} z} \quad (1.15)$$

$$\mathbf{H}_i = (0, H_{iy}, 0)e^{i(k_x x - \omega t)} e^{\pm k_{zi} z}. \quad (1.16)$$

Where the subscript i denotes the interfaces and the sign of k_{zi} is positive in the dielectric and negative in the metal, and describes the exponential fall off of the field as you move away from the interface. Taking the curl of \mathbf{H} we get,

$$\nabla \times \mathbf{H}_i = \begin{vmatrix} \hat{i} & \hat{j} & \hat{k} \\ \frac{\partial}{\partial x} & \frac{\partial}{\partial y} & \frac{\partial}{\partial z} \\ 0 & H_{iy} & 0 \end{vmatrix} = \left(-\frac{\partial}{\partial z} H_{iy}, 0, \frac{\partial}{\partial x} H_{iy}\right). \quad (1.17)$$

Using equation 1.10 we can write,

$$\nabla \times \mathbf{H}_i = \epsilon_0 \epsilon_i \frac{\partial \mathbf{E}_i}{\partial t} \quad (1.18)$$

$$\left(-\frac{\partial}{\partial z} H_{iy}, 0, \frac{\partial}{\partial x} H_{iy}\right) = \epsilon_0 \epsilon_i \left(\frac{\partial}{\partial t} E_{ix}, 0, \frac{\partial}{\partial t} E_{iz}\right). \quad (1.19)$$

Considering the x-component for the metal ($i = 1$) and dielectric ($i = 2$) this gives,

$$k_{z1} H_{1y} = -i\omega \epsilon_1 \epsilon_0 E_{1x} \quad (1.20)$$

$$-k_{z2} H_{2y} = -i\omega \epsilon_2 \epsilon_0 E_{2x} \quad (1.21)$$

and then dividing both equations gives

$$-\frac{k_{z1} H_{1y}}{k_{z2} H_{2y}} = \frac{\epsilon_1 E_{1x}}{\epsilon_2 E_{2x}}, \quad (1.22)$$

with the boundary conditions that $H_{1y} = H_{2y}$ and $E_{1x} = E_{2x}$ this leads to the surface plasmon condition

$$\frac{\epsilon_1}{k_{z1}} + \frac{\epsilon_2}{k_{z2}} = 0. \quad (1.23)$$

Thus to satisfy this condition the signs of the real parts of dielectric functions must be opposite, which explains why a metal-insulator interface can support surface plasmons. As we have assumed propagation along the x-direction we can write $\mathbf{E}(\mathbf{r}) = \mathbf{E}(z)e^{ik_x x}$ and our wave equation 1.14 becomes

$$\nabla^2 \mathbf{E} + (k_0^2 \epsilon - k_x^2) \mathbf{E} = 0. \quad (1.24)$$

Substituting into this our expressions for \mathbf{H} in the metal and dielectric leads to the system of equations,

$$k_1 = k_x^2 - k_0 \epsilon_1 \quad (1.25)$$

$$k_2 = k_x^2 - k_0 \epsilon_2 \quad (1.26)$$

$$(1.27)$$

which can be inserted into equation 1.23 to yield,

$$k_x = k_0 \sqrt{\frac{\epsilon_1 \epsilon_2}{\epsilon_1 + \epsilon_2}} \quad (1.28)$$

which is the dispersion relation for a propagating surface plasmon. These sets of equations derive the properties of surface plasmons from the dielectric environment and the dielectric functions of the materials in which they propagate. They show the response of the surface plasmons due to a change of either of these dielectric functions but do not give a picture of the response to size and shape changes of the materials. In cases where the materials have nanoscale dimensions, additional plasmonic modes known as localised surface plasmons

(LSPs) can also be excited and are of interest because their characteristics are tunable, as discussed below.

1.3.2 Localised Surface Plasmons

For a metallic nanoparticle with dimensions in the range of the penetration depth the electromagnetic excitation, the distinction between a surface and bulk plasmon disappears (see Section 1.2.2). This leads to the existence of localised surface plasmons, where scattering of propagating surface plasmons from the boundaries of the nanoparticle leads to standing wave solutions, known as localised surface plasmon resonances (LSPR). Figure 1.5 shows a simple schematic of a localised SP. Considering a spherical particle as shown in the figure, if the

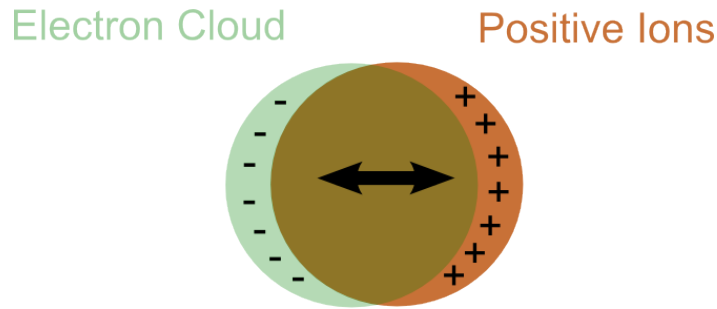


Fig. 1.5 A localised surface plasmon occurs in nanoparticles which are small enough to see the outside perturbation as a static excitation leading to a standing wave mode.

dimensions of this nanoparticle are less than half the wavelength of the incident radiation, the local field will appear to be static within the nanoparticle. This allows us to use a quasi-static approximation to simplify the problem. We can write the Laplace equation in spherical coordinates as,

$$\frac{1}{r^2 \sin \theta} \left[\sin \theta \partial_r (r^2 \partial_r) + \partial_\theta (\sin \theta \partial_\theta) + \frac{1}{\sin \theta} \partial_\phi^2 \right] \Phi(r, \theta, \phi) = 0 \quad (1.29)$$

where Φ is the electrostatic potential inside and outside the nanoparticle. This has solutions of the form,

$$\Phi(r, \theta) = \sum_{l=0}^{\infty} [A_l r^l + B_l r^{-(l+1)}] P_l(\cos \theta) \quad (1.30)$$

where the functions $P_l(\cos \theta)$ are the Legendre Polynomials of order l , and θ is the angle between the z axis and the position r . This solution is independent of the variable ϕ due to the azimuthal symmetry of the system (as we have chosen a sphere). Breaking this solution into the potential outside Φ_{out} and inside Φ_{in} the sphere further simplifies this solution, and taking into consideration boundary conditions gives,

$$\Phi(r, \theta)_{in} = -\frac{3\varepsilon_i}{\varepsilon_0 + 2\varepsilon_i} E_0 r (\cos \theta) \quad (1.31)$$

$$\Phi(r, \theta)_{out} = -E_0 r \cos \theta + \frac{\varepsilon_0 - \varepsilon_i}{\varepsilon_0 + 2\varepsilon_i} E_0 a^3 \frac{\cos \theta}{r^2} \quad (1.32)$$

where a is the radius of the sphere. This is an important result as it shows the dependence on the plasmonic resonance on the size of the nanoparticle. Figure 1.6 shows the result of changing the radius of the sphere on the resonant peaks. Although this result is appropriate only for a spherical object, similar considerations can be applied to more complex geometries and previous studies have shown the result of plasmons in nanodots and nanorods [18], nano-triangles, nano-disks, coupled nanoparticles and a number of other simple geometries [19][20]. We have also assumed that our excitation wavelength is much larger than the dimensions of the plasmonic nanoparticle, allowing us to use a quasistatic approximation. In the case of more complex interfaces, a boundary element method is a better solution and involves discretizing the interface of the two media and solving Maxwell's equations at each point in a mesh. This will be discussed in the Section 1.3.3.

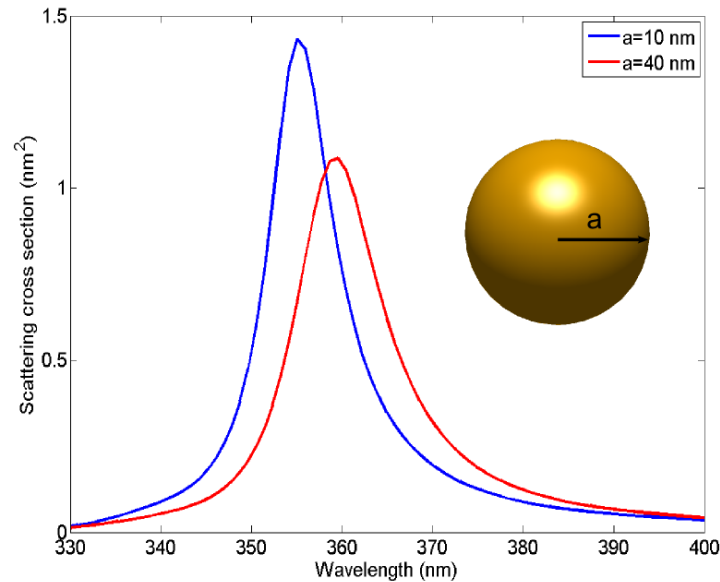


Fig. 1.6 Effect of particle size on resonant peaks for a planewave excitation of a gold nanosphere. We see that when the particle size is increased there is both a shift in wavelength of the plasmon mode, by about 10nm and a decrease in the overall intensity. This is what we would expect from the analysis.

1.3.3 Boundary Element Method

If we assume an excitation wavelength of a probe is much larger than the dimensions of a nanoparticle, we can use a quasistatic approximation to find the plasmonic response of the particle. However in the case of more complex interfaces, in order to solve Maxwell's equations a boundary element method is required. This involves discretizing the interface of the two media and solving Maxwell's equations at each point in a mesh. We can rewrite equation 1.14 in terms of a magnetic vector potential, \mathbf{A} , and electric scalar potential, Φ , such

that

$$\mathbf{B} = \nabla \times \mathbf{A} \quad (1.33)$$

$$\mathbf{E} = ik\mathbf{A} - \nabla\Phi \quad (1.34)$$

with \mathbf{A} and Φ being connected via the Lorentz Gauge condition

$$\nabla \cdot \mathbf{A} = ik\varepsilon\Phi. \quad (1.35)$$

Using these potentials we must solve Poisson equation

$$\nabla^2 G_i + k_i^2 G_i = -4\pi\delta(r) \quad (1.36)$$

where $k_i = \sqrt{\varepsilon_j}k$. The solution to which is a Green's function with the form

$$G_j(r-r') = \frac{e^{ik_j|r-r'|}}{|r-r'|}. \quad (1.37)$$

Leading to solutions for the potentials,

$$\Phi(\mathbf{r}) = \int_{\partial\Omega} G_i(\mathbf{r}-\mathbf{s}')\sigma_i(s')da' + \phi_{ext}(\mathbf{r}) \quad (1.38)$$

$$\mathbf{A}(\mathbf{r}) = \int_{\partial\Omega} G_i(\mathbf{r}-\mathbf{s}')\mathbf{h}_i(s')da' + \mathbf{A}_{ext}(\mathbf{r}) \quad (1.39)$$

$$(1.40)$$

where σ_i and \mathbf{h}_i are surface charge and current distributions respectively and ϕ_{ext} and \mathbf{A}_{ext} represent the scalar and vector potentials of the external perturbation. Equation 1.38 forms the basis of the BEM method. This method has the advantage that due to the calculation involved one only has to consider the boundaries separating the two dielectric media, and not the whole volume of the nanoparticle. Simulating Electron Energy Loss around plasmonic nanoparticles involves solving Maxwell's equations. A number of different solvers exist for doing this, some which use finite difference time domain (FDTD) techniques [21], some which use the discontinuous Galerkin time-domain (DGTD) [22] and others which use Discrete-dipole approximation with surface interactions [23]. In this work simulations are performed using the MNPBEM toolbox [24][25]. This method was developed for the simulation of metallic nanoparticles (MNP), using a boundary element method (BEM). This method uses metallic nanoparticles described through local and isotropic dielectric functions, separated by a sharp interface boundary. This approach relies on using a triangular mesh to solve Maxwell's equations at each node and compute the surface charge at each point in the mesh. The MNPBEM toolkit is used to study plasmons in a wide variety of areas, in this work we use the MNPBEM toolkit to solve Maxwells equations using the perbutation of an electron acting

as the excitations. EELS also has the advantage over light based techniques that so called dark modes, within optical measurements, can be detected [26].

1.4 The Electron Microscope

Here we give a brief overview of the technique of electron microscopy with particular reference to those concepts which be used later in this thesis, however this is not intended to be an exhaustive description and the reader is referred to several good texts including those written by Williams and Carter [1] and Fultz and Howe [27]. The concepts which will be explored here are: the typical setup of an electron microscope, the importance of the choice of the electron source and how such a choice effects measurements which can be taken in a microscope and the various techniques which will be used in terms of electron microscopy in this thesis. We will also give here a review of the relevant literature in the techniques of the electron microscopy of chiral materials, both using diffraction, and spectroscopy. As introduced earlier an electron microscope works on the same imaging principle as an optical microscope, however electrons are able to probe dimensions a thousand times smaller than that of light, with subatomic precision capable of resolving individual columns of atoms. The first step to probe samples with such resolution using electrons is to produce a high quality electron beam.

1.4.1 Electron Sources

An electron microscope requires a bright source of electrons. By brightness we mean a source which produces not only a high number of electrons but also a high number of electrons per unit area and per unit solid angle. There are two types of electron sources commonly found in electron microscopes: thermionic and cold field emission sources, which have different characteristics. The thermionic source uses a material with a low work function, Φ , which means it requires less energy to extract electrons from the tip. These tips are typically made of tungsten or a lanthanum hexaboride (LaB_6) crystal. The current density, J , of emitted electrons using this method is given by the equation,

$$J = AT^2 \exp\left(-\frac{\Phi}{kT}\right), \quad (1.41)$$

where T is the temperature, k is Boltzmann's constant and A is the Richardson constant, which is material specific. J has units of (Am^{-2}).

Alternatively, in a cold field emission electron gun an electron beam can be formed by Fowler-Nordheim tunnelling from the tip, where field emission is enhanced by strongly biasing the tip with respect to a nearby anode [28]. A sharp tip locally enhances the electric field, and as a result of a lower energy barrier the electrons in the tungsten tunnel out. The current density of emitted electrons using a cold field emission electron gun can be given by the

equation

$$J = \alpha E^2 \exp\left(\frac{\beta \Phi^{3/2}}{E}\right). \quad (1.42)$$

E is the electric field and α and β are material specific constants. The gun used in the experimental results seen in later chapters is the cold field emission type. A cold field emission electron gun has the advantage of increased coherence which increases the information one can obtain from a transmission electron microscope [29]. The choice of gun is important, as will be seen in the next two chapters, when studying plasmonic excitations. Plasmonic excitations lie at a lower energy when compared to other scattering events, which means the energy spread of the electron beam can obscure these excitations in experimental data. The electron gun must also produce a coherent source of electrons, as discussed in Section 1.2.3. Due to heating being used in some methods of extracting electrons from a filament the energy of emitted electrons can be in the form of a Boltzmann distribution, which means there will be a spread of wavelengths. This spread of wavelengths will make the electrons non coherent. In order to produce high contrast images this energy distribution must be a small fraction of the overall energy. Once a bright source of electrons has been produced, an electron beam can be formed in an electron microscope by a series of lenses.

1.4.2 Electron Microscope Optics

Once a high quality beam of electrons has been produced in an electron microscope the beam must be focused onto the specimen. Focusing an electron beam will not only decrease the size of the probe but will also increase the intensity of the beam. The lenses in a transmission electron microscope use electrostatic and magnetic fields to focus electron beams. By varying the strength of the lenses we can change the magnification or focus of an image in the microscope. A typical transmission electron microscope can be broken into 3 parts: the condenser, objective and projection systems. The condenser controls the illumination of the sample and both the intensity, via the current in the beam and the diameter of the probe. In conventional transmission electron microscopy (CTEM) electrons from the electron gun are focused to give parallel illumination of the sample. This is usually achieved using both the C1 and C2 lenses, although additional lenses within the objective lens assembly are also often used, as shown in Figure 1.7. Broadly speaking, the C1 lens provides a magnified image of the gun whereas the C2 lens controls the convergence angle of the probe. The condenser aperture allows control over the spread of the beam with a smaller aperture yielding an electron beam with higher spatial coherence but at the cost of lower current density. In CTEM, shown in Figure 1.7a, the upper objective lens is used to illuminate the specimen with a parallel beam. Once the beam has interacted with the specimen the beam is then passed through a series of projector lenses which magnify the image.

In scanning transmission electron microscopy (STEM), shown in Figure 1.7b, the condenser lenses are used to form a probe on the specimen by focusing the electron beam to a spot. The lower objective lens then spreads the beam once it has interacted with the specimen. This

probe can also be raster-scanned across the specimen to obtain information at each probe position, such as when using EELS as will be seen in the later chapters. The electrons in a transmission electron microscope can also be collected in a spectrometer after interacting with the specimen and this will be discussed in the next section.

1.5 Electron Energy Loss Spectroscopy

As discussed in Section 1.2.2, there are many ways an electron can interact with a sample. There may be a finite loss of energy to the sample, or no energy lost at all. The energy lost by the electrons can contain a rich amount of information about the structure, such as chemical composition, bonding information or even plasmonic modes. The technique of analysis such a loss of energy of electrons is called electron energy loss spectroscopy (EELS). After passing through the sample and losing energy, electrons are collected by an electron spectrometer. Figure 1.8 shows the typical setup of an EELS spectrometer. An EELS spectrometer contains a magnetic prism, made up of two pole pieces, which disperse electrons depending on their momentum (energy). This is done by applying a constant magnetic field perpendicular to the path of the electrons and relies on the Lorentz force. In the Figure, electrons that have lost no energy will be bent 90 degrees, whereas all other inelastically scattered electrons will be dispersed at different angles with respect to their energy lost during the scattering process. A drift, or flight tube, passes between the two pole pieces of the magnetic prism. A positive potential is applied to this non magnetic tube in order to accelerate the electrons. The drift tube can be used to shift the whole energy loss spectrum before the electrons meet the detector system. The energy spread of the electrons is usually determined by the spread of the source, as discussed above, however there will also be a resolution of the spectrometer itself and a resolution of the detector system, and as the spectrometer focuses the electrons, aberrations are added. A phosphor-coated CCD camera is then used to detect the electrons. This electron energy loss spectrum can be used to extract chemical information and information about the types of losses electrons have undergone in the sample. It can also be used in combination with a conventional image from a transmission electron microscope to build a broader picture of the specimen being studied in the microscope.

1.5.1 An Electron Energy Loss Spectrum

A typical EELS spectrum can be divided into separate regions, called the low loss and high loss regions. The low loss region, 0 – 100 eV will contain information about the weaker interaction of the probing electrons with valence electrons and those electrons which were elastically scattered. It will also contain the bulk and surface plasmon resonances. The high loss region, 100 eV and above, will contain elemental information, due to the high energy loss associated with the interaction of the probing electrons with the tightly bound core-shell electrons. This region will also contain bonding information. In this work it is the low loss

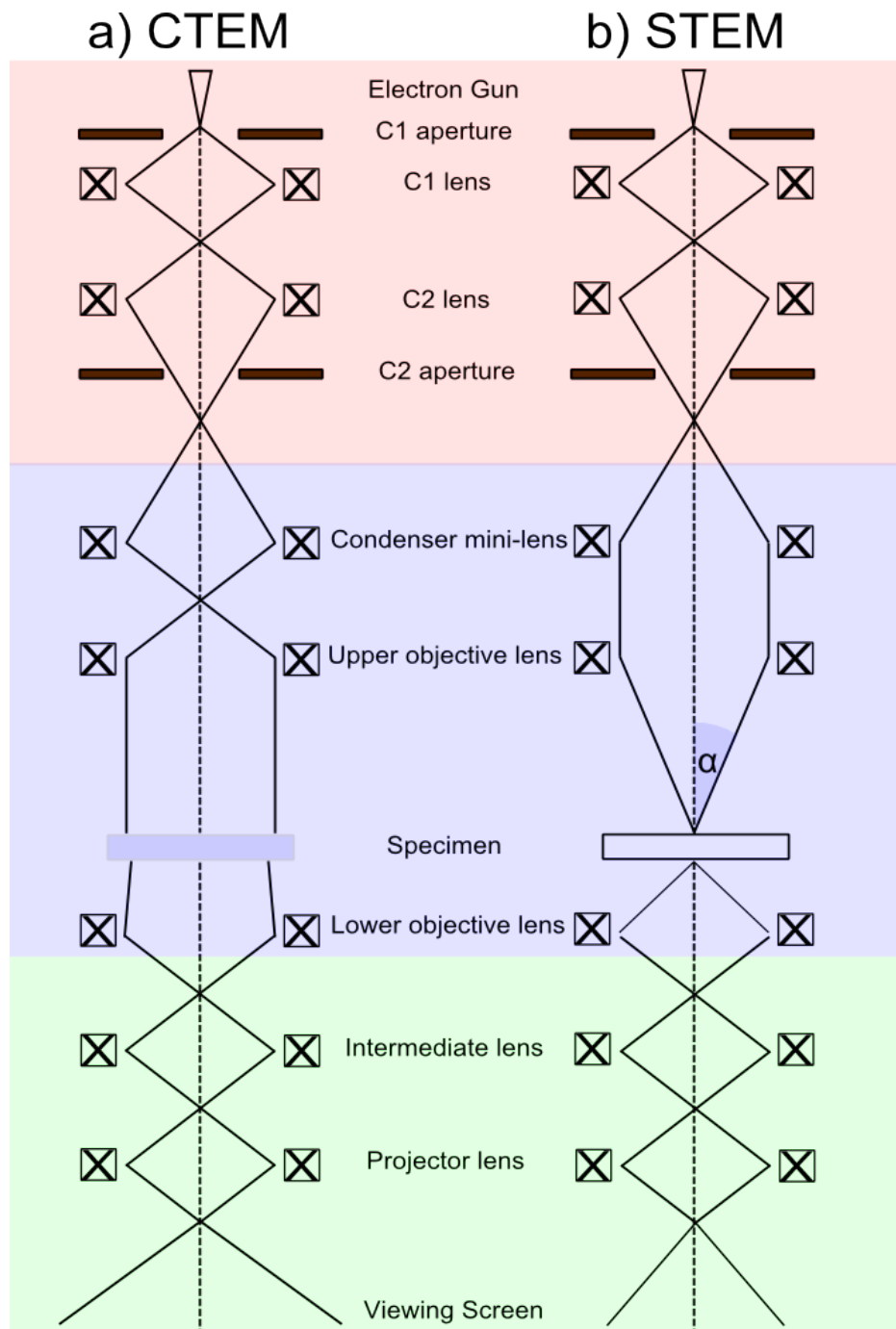


Fig. 1.7 Typical ray diagram for a transmission electron microscope operated in a) CTEM and b) STEM mode. An electron source emits electrons which are focused through a series of apertures and electromagnetic lenses to be imaged. In CTEM the specimen is illuminated by a planewave electron beam, whereas in STEM the beam is focused to a spot.

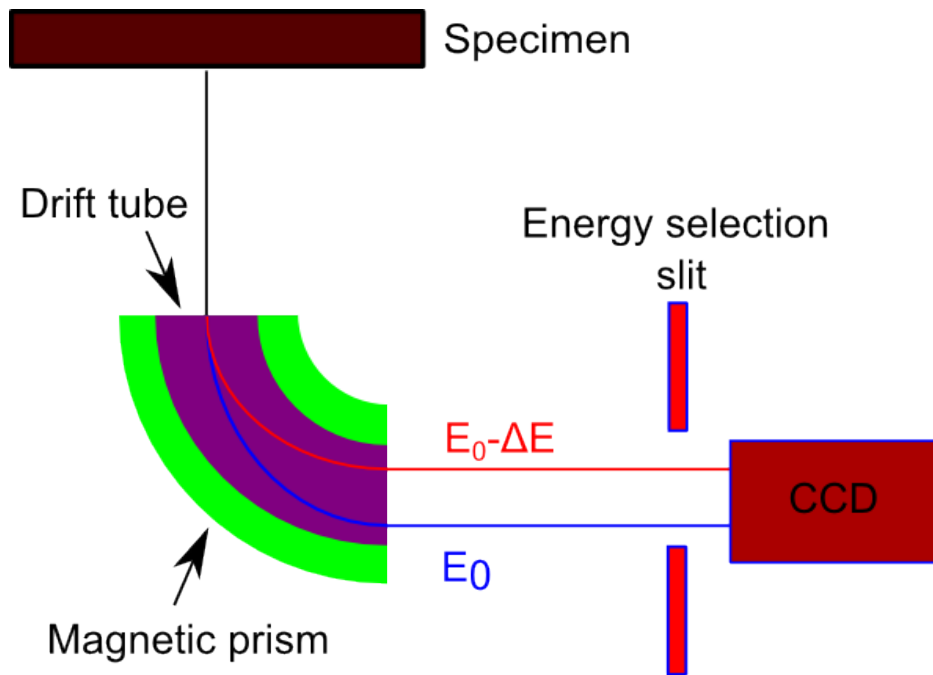


Fig. 1.8 Schematic of the EELS spectrometer where a magnetic prism is used to disperse electrons according to their momentum (kinetic energy). Electrons that lose no energy will be deflected by a given angle, whereas electrons that have scattered inelastically will be dispersed as a measure of the energy lost with respect to the incident beam.

region which will be of interest. Figure 1.9 shows an example of a typical loss spectrum. It is made up of an energy loss axis and an intensity axis. There are several features of note from the spectrum. The first is that out of the collected electrons, the most prominent are those which undergo no (or little) energy change. This is shown by the intense peak centered on zero energy loss, called the *zeroloss peak*. This represents electrons which have either been scattered elastically or have not been scattered at all (as mentioned previously the majority of electrons in the probe pass through the sample unaffected). Though there may be a small amount of energy lost for some of these electrons, the energy loss is below the resolution of the detector. However, post processing techniques can be used to improve this resolution, and will be discussed in later chapters. After the zeroloss peak, as you move up in energy, there are peaks with much smaller intensity. These peaks are plasmon peaks, and represent both surface and bulk plasmons. These peaks will be discussed in later chapters.

1.5.2 Spectrum Imaging

As discussed previously it can be advantageous to combine EELS and TEM in order to extract as much information as possible from one set of data. An example of this technique is spectrum imaging. Using a scanning transmission electron microscope, an energy loss spectrum can be obtained at each pixel in a STEM image, by raster scanning the probe over the specimen. This creates a four dimensional data cube, consisting of a two dimensional intensity (x, y) from the STEM image and at each x and y a given energy loss (E) and intensity.

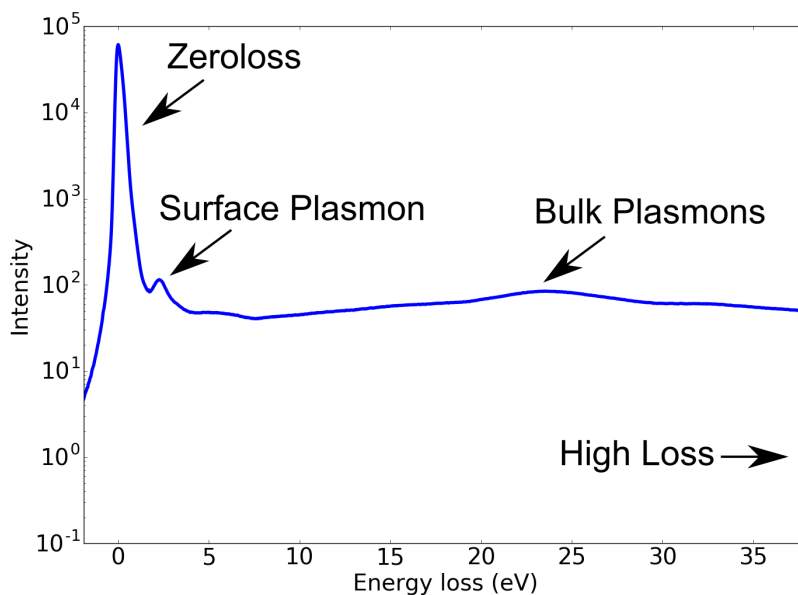


Fig. 1.9 A typical EELS loss spectrum which plots the signal intensity against the energy loss of electrons as they pass the sample. This shows a low loss region, where the dominant feature is the zero loss peak. The first plasmon peaks can be observed close to the zero loss. At higher energy, moving towards the high loss part of the spectrum, the bulk plasmon can be seen.

Spectrum imaging has the advantage of acquiring a lot of spectroscopic data in one image, but has the drawback that it requires long acquisition times. This high acquisition time can lead to a drift in the image which must be corrected while obtaining the image. This is done by recording a drift correction area with a short exposure survey, then during the spectrum image acquisition this drift correction area is reacquired every tenth line to reduce the effect of drift.

1.6 Chirality and How it is Studied

In his 1884 Baltimore Lectures, Lord Kelvin coined the word *chiral* saying “I call any geometrical figure, or group of points, chiral, and say that it has chirality, if its image in a plane mirror, ideally realized, cannot be brought to coincide with itself” [30]. This means all objects fit into two categories, chiral and achiral. Chirality is a symmetry property of matter and if the object can not be superimposed onto its mirror image, then it is chiral. The word chiral comes from the Greek meaning hand, due to the chirality of the human hands. Chiral pairs are called left and right handed enantiomers. Chirality is found in everything from the amino acids which make up all life [31], to artificial metamaterials [32]. When a chiral object interacts with circularly polarized light, which is chiral, then effects like optical rotation or circular dichroism can occur [33]. Optical rotation is caused by a difference in refractive index of left and right enantiomers, where the plane of linearly polarized light is

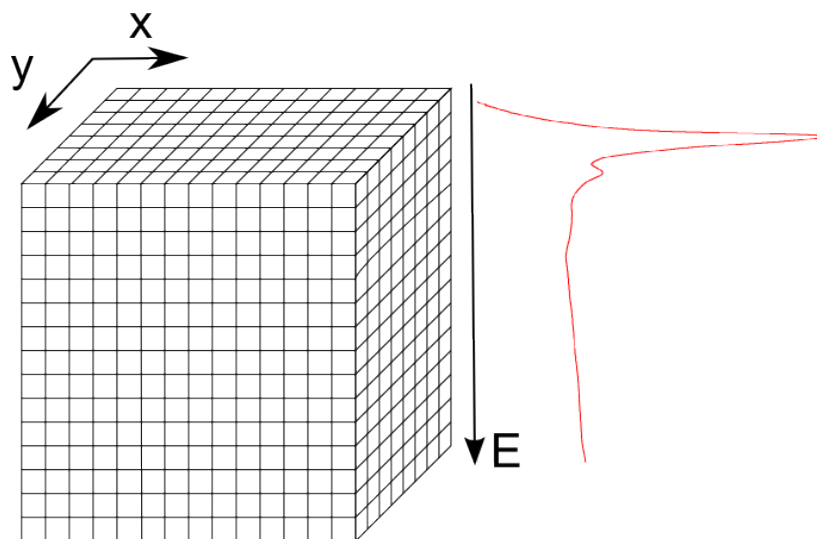


Fig. 1.10 A schematic diagram of spectrum imaging, showing the 4D data cube, which can be used for quantitative analysis of EELS. At each pixel in the STEM image a loss spectrum is obtained.

rotated. Circular dichroism is a difference in transmission between enantiomers caused by a difference in extinction coefficients [34].

Chirality can be quantified by different spectroscopy techniques such as by circular dichroism (CD), optical rotatory dispersion (ORD) and Raman optical activity (ROA) analysis. Circular dichroism spectroscopy measures the difference in the absorption of left and right handed circularly polarised light over a range of wavelengths and has been used to study surface plasmons in nanotubes[35]. Optical rotatory dispersion measures the variance of refractive indices for right and left handed enantiomers as a function of wavelength by measuring the rotation of the polarization of light. Raman optical activity uses a difference in Raman inelastically scattered right and left circularly polarized light in a chiral molecule. Most of these techniques began as tools for studying biological molecules, however the chiral fields produced by biological molecules tend to be weak. More recently these spectroscopy techniques have found similar use in the study of chiral plasmonic nanostructures where the fields are much greater.

1.6.1 Chiral Plasmonic Nanostructures

Chiral plasmonic nanostructures, or metamaterials, can also show optical activity, at a much larger scale than biological molecules. While the chiral response of organic molecules is well studied the equivalent response in artificial metallic nanostructures is less so. This optical activity in metallic nanostructures has been attributed to the presence of surface plasmons which exist on the nanostructure. The properties of this optical activity of chiral plasmonic nanostructures are what make them attractive as sensors. The superchiral electromagnetic fields, generated by the optical excitation of these nanostructures can be used as highly sensitive probes for bioanalysis [36][37]. Their properties also lead to the possibilities of

their use as optical broadband circular polarizers [38]. Weaker chiral effects in molecules are down to the magnitude difference between the pitch of the light beam and chiral arrangement of the molecule's bonds. Plasmonic nanostructures can be constructed to have a higher helical pitch which more closely matches that of the incident light, boosting the interaction. Far-field chiroptical response has been seen in planar nanostructures, multilayer structures and three dimensional nanostructures.

1.6.2 Observing Crystal Chirality in the Transmission Electron Microscope

A crystal which is chiral will belong to one of a chiral space group pair, with two nonequivalent crystal lattices, related to each other by a mirror plane, as shown for the two space groups $P3_121$ and $P3_221$ in Figure 1.11. Out of the 230 space groups there are only 65 chiral space groups, the so called Sohncke space groups [39]. The space groups shown in Figure 1.11 both contain a 3-fold screw axis of opposite handedness. Assignment of

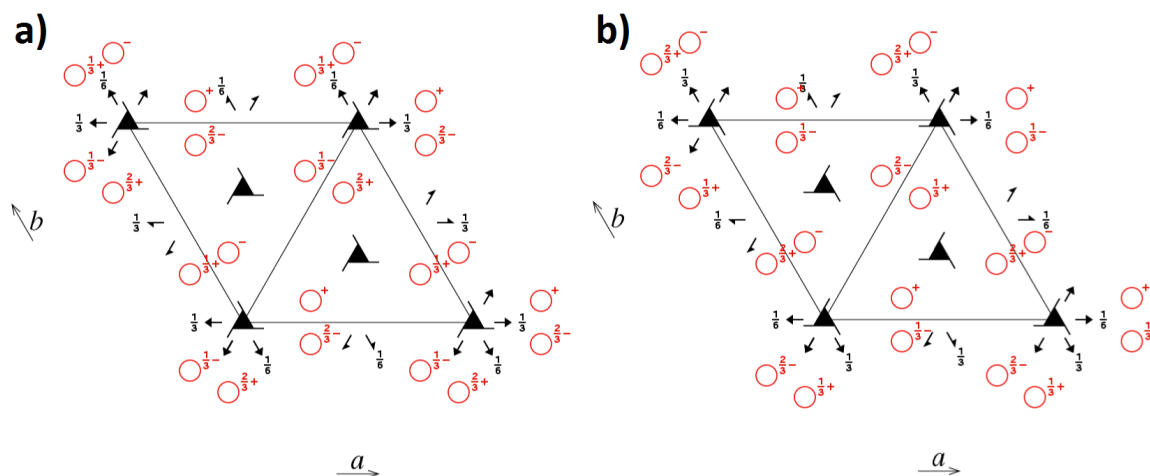


Fig. 1.11 The chiral space groups a) $P3_121$ and b) $P3_221$. The black triangles show threefold screw axes perpendicular to the plane of the page. The red circles show symmetry equivalent points. The superscript numbers, above the circles, denote the height in the c direction (perpendicular to the page). See [2] for more details.

the ‘handedness’ of a chiral crystal using Transmission Electron Microscopy (TEM) can be challenging. Conventional methods typically require collection of (often convergent beam) diffraction patterns collected at a number of different sample orientations for comparison with simulations that can vary from crystal to crystal [40]. This approach can be simplified by using zero-order Laue-zones (ZOLZ) mirror symmetry to orientate the crystal, but only for thin crystals [41]. Moving to thicker crystals allows the diffraction pattern to be seen (in the high-order Laue-zones) as a three-dimensional rather than a two-dimensional projection of the crystal. This is useful as a two-dimensional projection of a chiral crystal would not detect a change in the handedness. A further complication in chiral determination is that

Friedel's law (see Section 1.2.3) adds a centre of inversion to the diffraction pattern that may not be present in the crystal; this may be overcome in the dynamical diffraction regime, where multiple scattering breaks Friedel's law, but requires thicker crystals [42].

1.7 Optical and Electron Vortices

It has been known for the last few decades that light can carry orbital angular momentum (OAM) [43]. This OAM can be visualised by considering the wavefront of the light, when this wavefront is twisted to form a helix the photon has a nonzero OAM, which can take on multiple integer values of \hbar , rather than the flat wavefront of plane wave illumination. Over

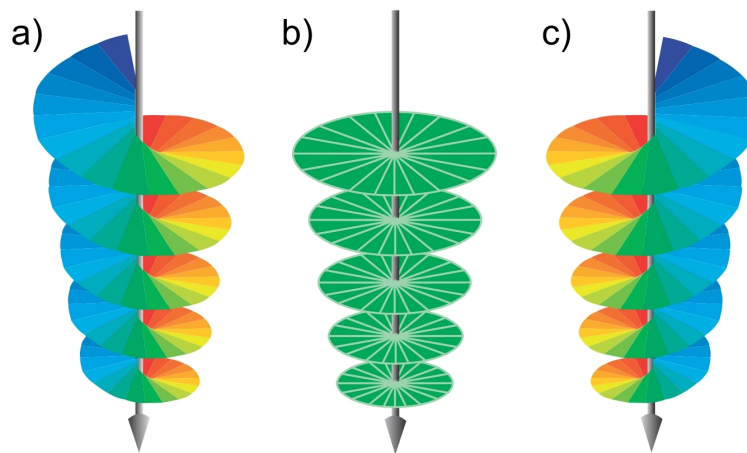


Fig. 1.12 The wavefront for a) $l=-1$, b) $l=0$ and c) $l=+1$ electron beam, the different values of l give rise to twisted wavefronts for the vortex beams and the planar wavefront of a planewave. The twisted wavefront gives rise to a quantised OAM about the axis of propagation.

the last two decades optical vortices have become a prominent research field with applications spanning optical tweezers to memory storage [44][45]. Similarly, electron vortex beams can be formed with an intrinsic orbital angular momentum about their axis of propagation [46]. Figure 1.12 shows the difference in the propagating wavefront of two vortex beams of different sign of OAM and a planewave beam. Electron vortex beams have attracted substantial research interest since their experimental debut because of the new degrees of freedom that they offer, such as a tunable and quantized magnetic moment which opens up exciting new degrees of freedom for diffraction and other electron microscopy techniques. Their orbital angular momentum suggests prospects of electron-optical analogues of optical tweezers and enhanced optical imaging techniques. Electron vortices were first noted in photoemission experiments [47] and were more recently proposed by Bliokh to be feasible in the high energy beams of electron microscopes and have now been produced experimentally [48][49].

An electron vortex beam's quantised OAM can take on values of $l\hbar$, where l is the OAM quantisation number, sometimes called the winding number, describing the twist of the beam [50]. The OAM term gives rise to an azimuthal phase dependent term which, when added to

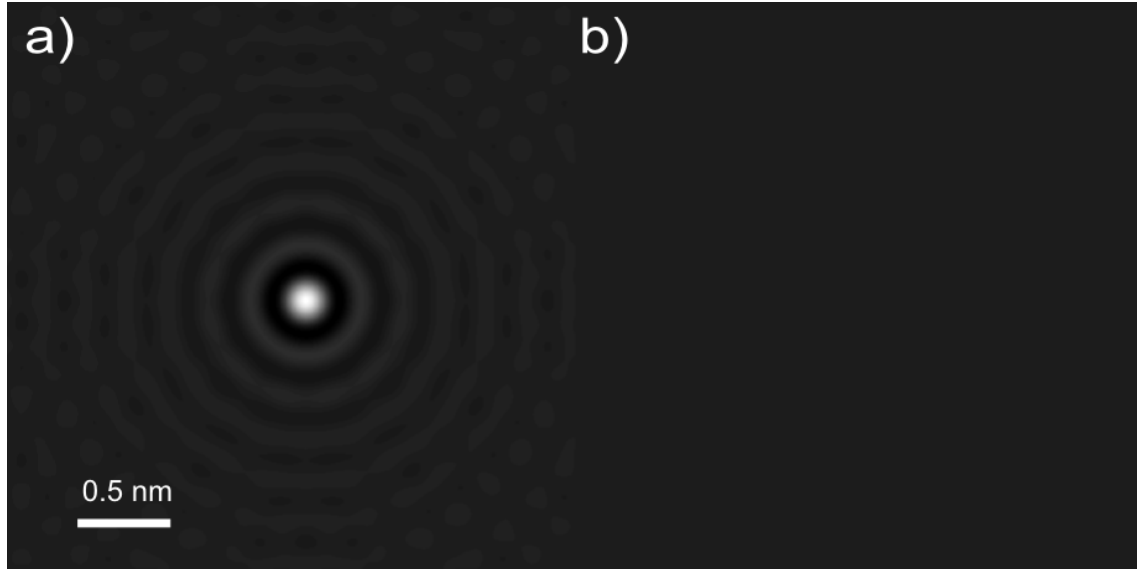


Fig. 1.13 A 2D representation in the (x,y) plane showing the a) real and b) imaginary parts of a Gaussian wavefunction, Ψ . Before propagating through the crystal the Gaussian wavefunction is purely real.

the conventional plane wave wavefunction, gives the typical wavefunction of a vortex beam. The location of electrons in an electron beam can best be described by this wavefunction, Ψ , which defines the most probable location of the electrons in space. It is made up of a real and imaginary part as so,

$$\Psi = \Psi_{real} + i\Psi_{imag} \quad (1.43)$$

In the case of a vortex beam of electrons this wavefunction can be written in the form,

$$\Psi = \exp(ik_z z + il\theta), \quad (1.44)$$

where k_z is the axial wavevector, l the quantized OAM of the beam, z is the distance along the axis of propagation and θ is the azimuthal angle about z . This differs from the a conventional planewave by the addition of the $l\theta$ term which gives the vortex beam its phase dependence. The resulting phase has an axial singularity in the centre, producing a “donut” like probability density intensity profile, as illustrated by the schematics in the next section, Figure 1.15. This wavefunction contains all the information needed to describe the electrons in the beam. It defines the energy, shape and position. Figure 1.13 shows the real and imaginary parts of the wavefunction for a Gaussian planewave beam. Figure 1.14 shows the real and imaginary parts of the wavefunction for a vortex beam: note the appearance of a prominent imaginary part in comparison to that for the Gaussian beam. It is the wavefunction which will be propagated through the crystal potentials, using the multislice algorithm as will be discussed in Section 1.8. The wavefunction is not however the most intuitive way to imagine electron beams, as they contain an imaginary part.

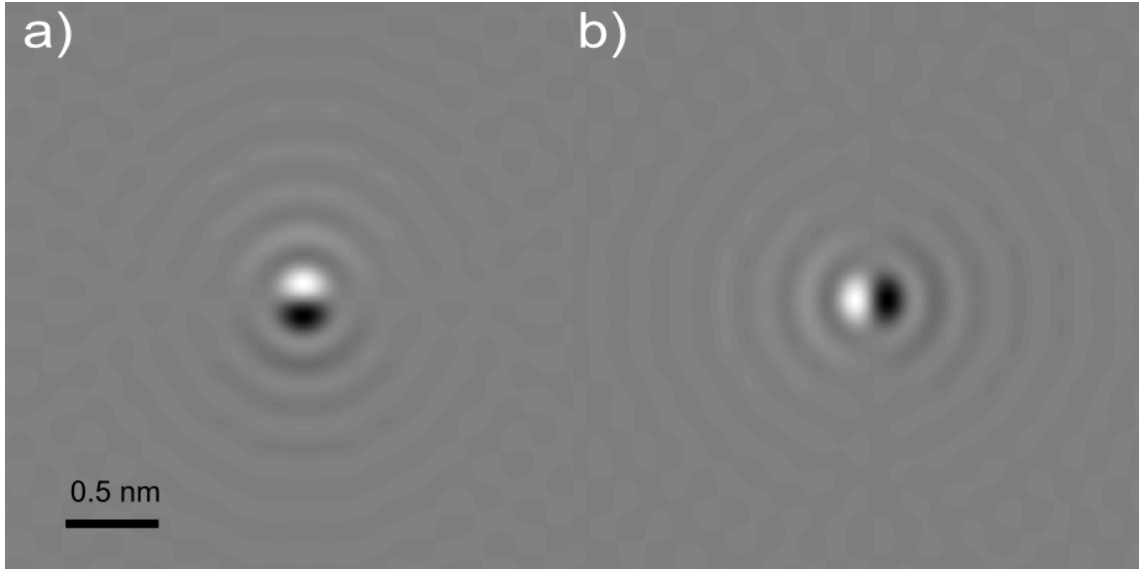


Fig. 1.14 A 2D representation in the (x,y) plane showing the a) real and b) imaginary parts of a vortex wavefunction, Ψ . Note the presence of imaginary part in the wavefunction of a vortex beam when compared with a Gaussian beam.

The real and complex parts of the wavefunction can be combined as a probability density, ρ , which is defined as the square of the wavevector and is purely real;

$$\rho = \Psi^* \Psi = |\Psi|^2. \quad (1.45)$$

The probability density is an amplitude that defines the most probable location of an electron in our beam. Thus if we were to integrate over all space the result would be unity. In this work the probability densities of electron beams follow a “donut” shape pattern as shown in Figure 1.15. This ring shape can best be described by a Bessel function of the first kind, where the amplitude at the origin is zero and oscillates radially. The probability density of a vortex beam contrasts with that of a Gaussian beam (planewave) in which probability density forms a concentrated spot which decreases radially in intensity. As the vortex beam passes through a material the wavefunction, Ψ , changes as the distribution of electrons changes. This change in distribution will depend on the symmetry of the material and the symmetry of the beam intensity and phase. Thus, another important property in understanding how electrons travel through a material is the change in probability density, known as probability current, $j(x_i)$ with $i = \{x,y,z\}$ where $j(x_i)$ is the rate of change of the probability density in i^{th} direction. Calculating probability currents at each layer will reveal how the electrons scatter from each potential layer and show how electrons propagate within the crystal. This is calculated from the wavefunction by;

$$j(x_i) = \frac{i\hbar}{2m} \left[\Psi^* \frac{\partial \Psi}{\partial x_i} - \Psi \frac{\partial \Psi^*}{\partial x_i} \right]. \quad (1.46)$$

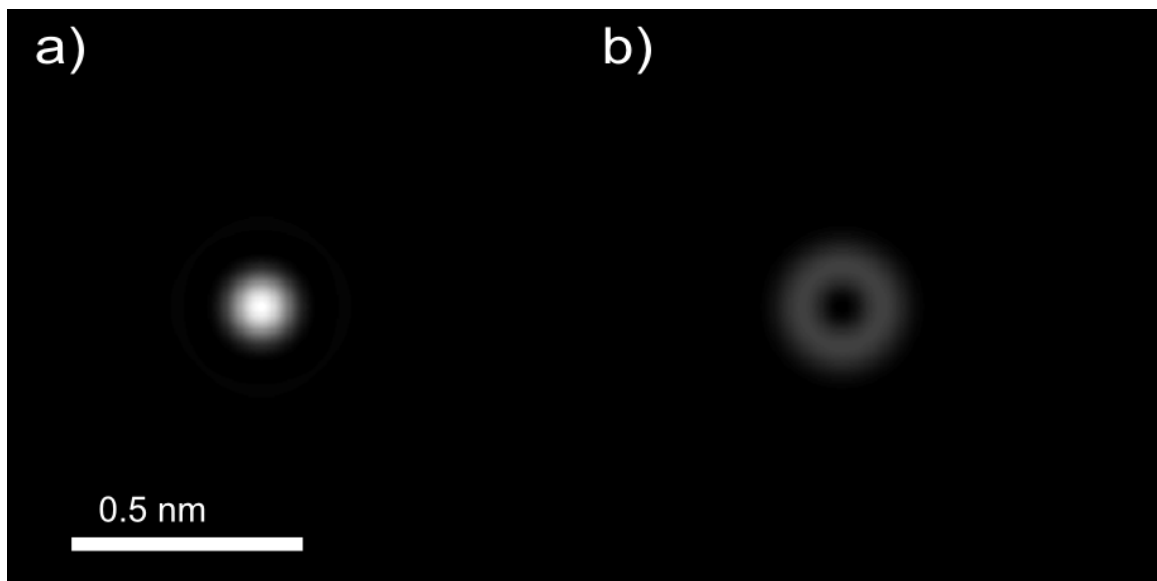


Fig. 1.15 A 2D representation of the probability density a) of the beam shown in Figure 1.13 and b) Figure 1.14 showing a Gaussian and vortex beams probability density respectively. Due to the difference in intensity distribution the vortex beam appears less intense.

For the beam shown in Figure 1.14 the probability current can be calculated and it shows something fundamental about the beam. For a beam with OAM with a value, $l = 1$ you can see the spiraling current $j(x,y)$ shown by the arrows in the x-y plane shown in Figure 1.16. It is this spiraling current that gives rise to the OAM about the z axis, which in this figure would pass through the centre of the beam. It is also this spiraling current which gives our beams a chirality. For an $l = 1$ beam, as shown, the current circulates with a right handed twist, and left handed for an $l = -1$ beam. It has been found that the OAM states in a vortex beam can

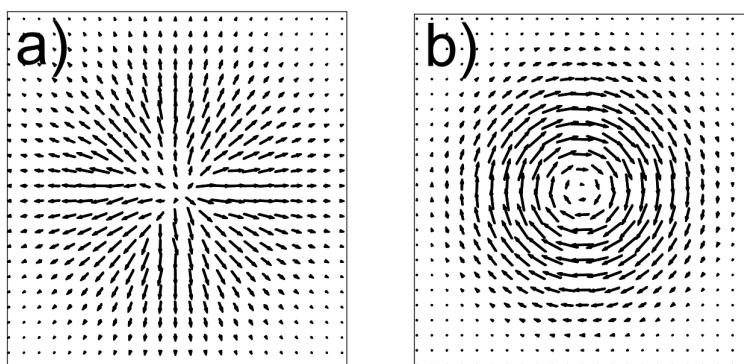


Fig. 1.16 The 2D probability current $j(x,y)$ of the beams shown in a) Figure 1.13 and b) Figure 1.14. Notice that the Gaussian probability current propagates outwards from a point, whereas the vortex current is a circulation about the centre. This is the inherent chirality of the beam.

decompose as the beam propagates through a crystal [51], thus one must calculate the OAM states at each layer in a crystal in order to fully understand vortex beam propagation.

1.7.1 Orbital Angular Momentum

Loffler et al. found that unlike in free space, an electron vortex can become distorted in a material, leading to the decomposition of the initial OAM into other non integer OAM states [52]. The shape and handedness of our vortex beams will be used to determine chirality, thus we must have a clear picture of the OAM value for our beam. Using the Multislice algorithm the expectation value of the orbital angular momentum of the beam is shown to oscillate as a function of depth but with varying oscillatory nature dependent on lateral position on the unit cell. Thus, we will calculate OAM as a function of depth in our materials. OAM can be written in operator form:

$$L = \mathbf{r} \times \mathbf{p} = \begin{vmatrix} \hat{x} & \hat{y} & \hat{z} \\ x & y & z \\ i\hbar \frac{\partial}{\partial x} & i\hbar \frac{\partial}{\partial y} & i\hbar \frac{\partial}{\partial z} \end{vmatrix}$$

Giving the three operators, L_x , L_y and L_z as

$$L_x = yi\hbar \frac{\partial}{\partial z} - zi\hbar \frac{\partial}{\partial y}, \quad (1.47)$$

$$L_y = zi\hbar \frac{\partial}{\partial x} - xi\hbar \frac{\partial}{\partial z} \quad (1.48)$$

and

$$L_z = xi\hbar \frac{\partial}{\partial y} - yi\hbar \frac{\partial}{\partial x}. \quad (1.49)$$

To calculate the expectation value of these OAM values we use the wavefunction of the electron:

$$\langle L_i \rangle = \Psi^* L_i \Psi. \quad (1.50)$$

For the case of L_z this can be expanded as:

$$\begin{aligned} \langle L_z \rangle &= \Psi^* (xi\hbar \frac{\partial}{\partial y} - yi\hbar \frac{\partial}{\partial x}) \Psi \\ &= (\Psi_{real} - i\Psi_{imag})(xi\hbar \frac{\partial}{\partial y} - yi\hbar \frac{\partial}{\partial x})(\Psi_{real} + i\Psi_{imag}) \end{aligned}$$

Giving the real component of L_z as:

$$Re(\langle L_z \rangle) = \Psi_{real}(y\hbar \frac{\partial \Psi_{imag}}{\partial x} - x\hbar \frac{\partial \Psi_{imag}}{\partial y}) + \Psi_{imag}(x\hbar \frac{\partial \Psi_{real}}{\partial y} - y\hbar \frac{\partial \Psi_{real}}{\partial x}) \quad (1.51)$$

Similarly for L_x and L_y ;

$$Re(\langle L_x \rangle) = \Psi_{real}(z\hbar \frac{\partial \Psi_{imag}}{\partial y} - y\hbar \frac{\partial \Psi_{imag}}{\partial z}) + \Psi_{imag}(y\hbar \frac{\partial \Psi_{real}}{\partial z} - z\hbar \frac{\partial \Psi_{real}}{\partial y}) \quad (1.52)$$

$$Re(\langle L_y \rangle) = \Psi_{real} \left(x\hbar \frac{\partial \Psi_{imag}}{\partial z} - z\hbar \frac{\partial \Psi_{imag}}{\partial x} \right) + \Psi_{imag} \left(z\hbar \frac{\partial \Psi_{real}}{\partial x} - x\hbar \frac{\partial \Psi_{real}}{\partial z} \right) \quad (1.53)$$

Equations 1.51, 1.52 and 1.53 will be used to probe the OAM value as a function of depth in a crystal to better understand the interaction of a chiral beam and a chiral crystal.

1.8 The Multislice Method

In this work we map the change in probability density and current as a vortex beam of electrons passes through a crystal. To do this we first need to understand how the electron's wavefunction changes as it passes through a crystal. For this we will use the *multislice method* formulated by Cowie and Moodie [53]. In this method a crystal is divided into 'slices' in the direction of propagation, which in this work is the z direction. A natural choice is the individual potential layers in the crystal with each slice being separated by a distance Δz .

An electron wavefunction Ψ_n of the beam is successively passed through the slices of the crystal. At each slice an exit wavefunction Ψ_{n+1} is calculated. This exit wave is then propagated through the crystal until it gets to the next slice, with the whole process being repeated until the wave exits the crystal.

$$\Psi_n \rightarrow \text{effect of slice} \rightarrow \Psi_{n+1} \rightarrow \dots$$

Kirkland [54] developed the code that will be used in this chapter to calculate the electron wavefunction at each layer in a crystal using the multislice method. The code runs by inputting the beam wavefunction $\Psi_n(x, y)$ as a 2D image including the real and imaginary parts, of the form of Figure 1.13. This input wavefunction is first multiplied by a *transmission function*, $t_n(x, y)$, for slice n . This transmission function is the effect of the beam seeing the potential of the slice. As the wave function of the electron passes through the slice it gains a phase that is related to the slice potential. The transmission function can be written as

$$t(x, y) = \exp \left[\int_z^{z+\Delta z} i\sigma V(x, y, z') dz' \right] \quad (1.54)$$

where σ is an interaction parameter related to the energy of the electrons and their mass. The integral in this equation is the potential that the electrons interact with in the slice $z \rightarrow z + \Delta z$, called the *projected potential*. Once the electrons have interacted with the slice the next step is to propagate the electron through vacuum to the next slice. To do this a propagator function, $p(x, y, z + \Delta z)$, is defined which is related to the energy of the beam and the slice thickness Δz ,

$$p(x, y, z + \Delta z) = \frac{1}{i\lambda\Delta z} \exp \left[\frac{i\pi}{\lambda\Delta z} \cdot (x^2 + y^2) \right] \quad (1.55)$$

It should be noted that Δz in Eqn 1.55 is the distance (in vacuum) between slices, whereas Δz in Eqn 1.54 was the finite width of the potential layer. The propagation is in reciprocal

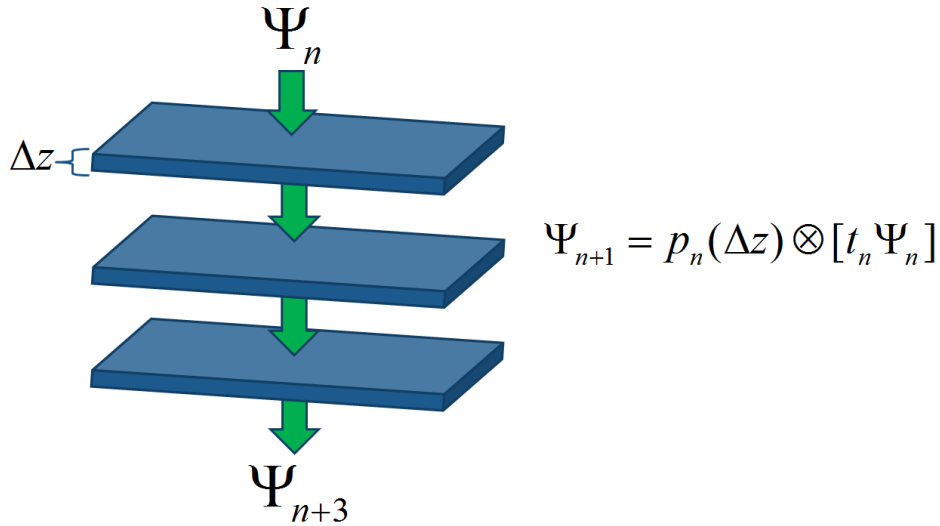


Fig. 1.17 Schematic of the Multislice method. In this method a crystal is divided into potential slices in the direction of propagation the effects of each slice are calculated individually and then the wavefunction is propagated through free space.

space so the multiplication of $t_n(x,y)\Psi_n(x,y)$ by $p_n(x,y,\Delta z_n)$ in reciprocal space becomes a convolution in real space. In a compact form the full multislice algorithm can be written

$$\Psi_{n+1}(x,y) = p_n(x,y,\Delta z_n) \otimes [t_n(x,y)\Psi_n(x,y)]. \quad (1.56)$$

1.9 Outline of Thesis

The remainder of this thesis is broken into three main sections. First we begin by detailing the potential of electrons as probes of chiral metamaterials in Chapter 2. This is done in the context of electron energy loss spectroscopy, where the feature of importance is the change in momentum of the electron probe as it scatters in a material. We study experimental data of a plasmonic nanoparticle and its counterpart hole structure. In Chapter 3 we present simulations of realistic and ideal plasmonic nanoparticles to show the role of imperfections in structure on the plasmonic response of the nanoparticles. Chapter 4 details the potential of chiral electron probes as probes of chiral materials. Here we are looking at elastic scattering in the form of diffraction. We exploit the chiral phase profile of the probing electron in order to create enantiospecific scattering. This serves as a first step towards using a chiral probe to probe chiral metamaterials which is discussed in the outlook chapter.

Chapter 2

Experimental Comparison of Gold Chiral Plasmonic Nanoparticles.

2.1 Introduction

Embedded nanoparticulates have been used in glass and artwork to generate bright colours since classical times. Gold nanoparticles of varying shapes and sizes have been found in stained glass windows and glass cups made in Roman times and were used to manipulate the colour of light including that of the famous Lycurgus Cup shown in Figure 2.1. This cup,



Fig. 2.1 The Lycurgus Cup is one of the oldest examples of the exploitation of the unique interaction of nanoparticles with light. The cup appears a) green in colour when seen by reflected light and b) red when lit from within the cup. Printed with permission from the British Museum [3].

which dates back to the 4th century, undergoes a brilliant colour change when illuminated with light and is amongst one of first known examples of the exploitation of the unique interaction of nanoparticles with light. The cup appears green when seen with reflected light and appears

red when light is transmitted through the cup. Roman glass makers often used scrap metal, gold and silver, to make their works more colourful and electron microscopy of the Lycurgus cup reveals nanoparticles of gold around 70 nm in size. It is these nanoparticles which are responsible for this unique colour change in the cup, as the nanoparticles resonantly reflect green light making the cup appear red when illuminated with white light. This resonance is caused by surface plasmons (SPs) and for this reason the Lycurgus cup is now commonly used to illustrate the phenomenon of light interacting with SPs. The unique interaction with light caused by the nanoparticles in the cup wasn't explored until the early part of the 20th century, despite many artists and craftsmen exploiting this phenomenon over the last millennium. Theoretical studies of surface plasmons began with the mathematical description of surface waves by Zenneck and Sommerfeld when they developed a basis which used solutions to Maxwell's equations which had the form of a vertically polarized electromagnetic plane wave [55]. Also at this time work was being done to look at intensity drops of reflected light from metallic diffraction gratings by Wood [56] which was later explained in terms of "polarized quasi-stationary waves" at the surface of a metal [57]. Wood noted that this effect was only present for p-polarized light, meaning it was a result of the interaction of the light field with the grating. Parallel to this work, Richie began a study of similar losses of high energy electrons in thin films [58], with Richie being the first to use the term surface plasmon. Richie used surface plasmon losses to explain valence losses of fast electrons passing through thin foils, with peaks seen at different energies to the bulk plasmon. This "low-lying loss" proposed by Richie was confirmed using EELS a few years later [59] and was followed by work showing the optical excitation of SPs by Kretschmann and Otto [60, 61].

Alongside experimental realization of surface plasmons theories were also being devised to explain scattering of light by metallic nanoparticles [62, 63]. In his work on the absorption of light by gold colloids, Gustav Mie developed the groundwork of the scattering theory which would later bear his name. Mie studied the scattering and attenuation of light by gold colloids and produced the first observation of plasmon resonance absorption and the first such study that considered light interacting with particles with dimensions much smaller than its wavelength.

Of the two types of plasmonic excitation discussed in Sections 1.3.1 and 1.3 the work in the next two chapters will focus on localized SPs. These are non-propagating excitations which usually appear on the surface of metallic nano-structures and are sensitive to changes in the local dielectric environment. As a result of this sensitivity to fields they have found applications in areas such as biological and chemical sensors [64]. The range of applications of surface plasmons has led to a great research interest in the 50 years. Applications include probes of material interfaces [65], gas detection [66] with most research interest focusing on the use of surface plasmon resonance sensing [67, 64]. The use of SPs as sensors relies on their sensitivity to changes in the local dielectric environment and the strongly enhanced local electric fields produced around the surfaces in which they exist [68].

Although surface plasmons have been known to exist for some time the influence of a particle's boundary on the properties of the SPs is an emerging field of research. It has been found in the past that the shape and size of a nanoparticle can effect the spatial distribution and energy at which SPs appear at a particle boundary.

Surface plasmons can be probed by a variety of different methods including optical spectroscopy, reflective and Raman scattering techniques [69]. In this work localized surface plasmons are probed using EELS where electrons with kinetic energies of a few hundreds of keV penetrate through a metal particle and excite surface and bulk plasmons. The resonance frequencies of these plasmons can then be directly interpreted from the energy loss spectra as shown in the previous chapter. In STEM the electron beam is scanned across the surface of plasmonic nanoparticle and loss maps can show both resonances and spatial distribution (loss maps) of the particles plasmons. EELS has been used in this way to study plasmon modes of nano-triangles, nano-disks, coupled nanoparticles and a number of other simple geometries [19, 20]. Studies have also found that modes can split due to the interaction with a substrate [70]. This opens up a new area of research which has applications in tunable materials. By attaching a substrate which shifts the energy of a mode by a given energy, the plasmonic response of a nanoparticle can be tuned. One of main areas of interest in this work is when metallic particles have a chiral shape, or form part of a chiral metamaterial. As discussed in Section 2.6, a particularly interesting aspect of these prototype sensors is the potential to use chiral plasmonic resonances to probe the intrinsic chirality of a variety of biological molecules.

In this chapter we will outline the use of the electron energy loss spectroscopy in studying both a chiral plasmonic nanostructure and a hole structure. We will first introduce why there is research interest in plasmonic hole structures and introduce the concept of Babinet's Principle, which tells us the link between the positive structure and its hole counterpart. We will discuss how this principle manifests in our results and give a simple example. We will also discuss the applications of hole structures in the context of chiral metamaterials and the prospects of nanoscale optical circuits. We will then study experimental data for both structures and compare and contrast the modes seen. To analyse these modes we will first have to process the experimental data, details of which will be given in Sections 2.8 and 2.9. We complete this chapter with a thickness calculation on the experimental data which will be used to create a mesh so that we can simulate a more accurate comparison between the two structures in the next chapter.

This chapter will use a real experimental data set to illustrate the key concepts and processes required for its complete analysis. It is natural to also explore the results of that analysis, which is here done by providing a direct comparison of experimental data sets for a complementary 'particle' and 'hole' structures.

2.2 Plasmonic Hole Structures

A negative plasmonic nanoparticle, sometimes called a templated plasmonic substrate [71] or inverse plasmonic nanoparticle, is a hole (or series of holes) in a plasmonic material. The structures that will be of interest in this chapter are a sixfold shuriken (throwing star) shaped gold nanoparticle and an equivalently shaped hole. Inverse plasmonic structures have gained as much research interest as their solid nanoparticle counterparts since the observation that subwavelength hole arrays in thick opaque metal films led to increased optical transmission in 1998. Ebbesen et al. explained this increased optical transmission in holes by the coupling of light with plasmons [72]. More recently it was also shown that modulated surfaces, perforated with sub-wavelength holes, could suppress transmission of light, and thus increase absorption [73]. Following this a number of studies have focused on the role of surface plasmons on the transmission and absorption of light due to arrays of holes on metals [74]. This was accounted for by the short range surface plasmon excitation. This excitation generates large fields due to the incident light energy being converted into plasmonic energy that can then be transferred through the small hole and re-radiated at the far side. This means light can cross small distances which would usually be below the diffraction limit. Manipulating and directing light on such a small scale is one of the more interesting applications of surface plasmons, leading to the development of surface-plasmon based circuits where research into electronics and optics merge at the nanoscale. Arrays of plasmon holes which couple to light also have applications in the field of metamaterials. With recent advances in experimental design such as injection molding, arrays of holes can be easily fabricated. Thus if holes can be shown to have similar properties to their solid counterpart then the design of plasmonic circuits could be made cheaper and easier.

As was discussed in the introduction chapter, it has been found that the shape and size of a plasmonic nanoparticle effects the modes which can be supported on its surface, which is also true of the dimensions of a hole in a plasmonic nanoparticle. It has been found that a decrease in the size of a hole in a metal can blue-shift the spectral peaks in the transmission spectra [75]. Shape has also been shown to have an effect on the transmission of light, with it being shown that a shape change from circular to rectangular increases the overall intensity transmitted despite a decrease in the overall area of the hole [76]. All these properties of transmission of light derive from the SPs bound to the edges of the holes just as for the solid nanoparticle.

In this chapter we examine the modes which are supported by both a negative plasmonic particle and its solid counterpart, by processing an experimental data set. EELS studies of negative plasmonic structures are few, with those that exist in the literature focusing on simple geometric structures such as circles [77] or rings [78]. These studies found that the inverse structure was similar to its counterpart, but for simple 2D shapes which lack the coupling between modes that will be seen in our results. The structures which are examined in this work are complex 3D shapes which deviate from simple planar shapes as are commonly

found in the literature. For this reason we study, in the following chapter, the effects of this 3D shape verses and idealised structure.

2.3 Localised Surfaces Plasmons in Coupled Nanospheres

As was mentioned in the Section 1.3.2, the size of a nanosphere can impact on the plasmonic modes which it can exhibit. Plasmon response has also been studied in relation to coupling between nanoparticles. Some of the earliest studies of plasmons using EELS has studied the interaction of two neighbouring spheres [79][80]. It was found that individual plasmon modes couple, leading to hybridization. In terms of EELS this was explained by the coupling of an electron to the two particles, and shown by the change in loss spectra, depending on the particle size and interparticle distance [81]. The coupling of individual particles is important in more complicated nanoparticle geometries where different regions of the nanoparticle may interact with each other if close enough. Figure 2.2 shows the effect of introducing a secondary sphere to a system with one sphere. As was shown in Figure 1.6, we see a shift in wavelength (energy) of the mode corresponding to the single sphere, which indicates that the spheres are interacting and the individual modes in the two spheres are coupling. This type of coupling has applications in the field of metamaterials where assemblies of nanoparticles can be used as elements in an array, due to the interaction of localised plasmons between the nanoparticles in the array. Figure 2.2 was calculated using the MNPBEM toolbox as discussed in Section 1.3.3. This effect would decrease as the distance between the nanospheres was increased, until only the single peak shown in Figure 1.6 remained.

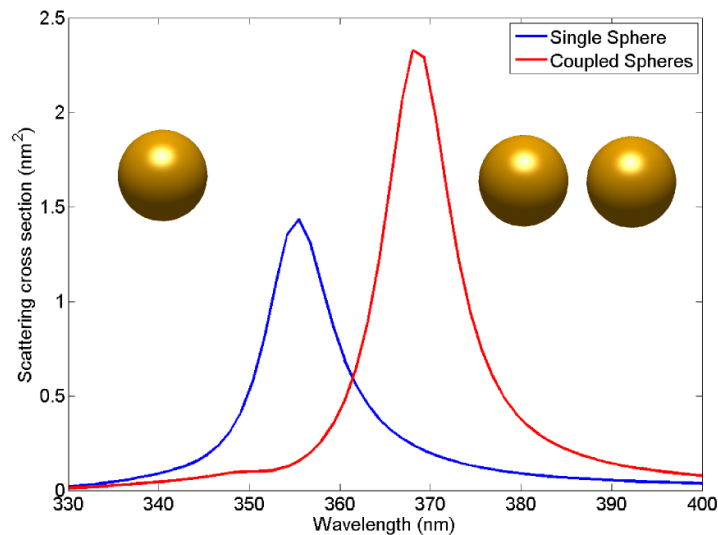


Fig. 2.2 Coupling effects between nanospheres, calculated using the MNPBEM toolbox as discussed in Section 1.3.3. We see that when a second sphere is added there is a shift in wavelength and thus in energy of the plasmon mode, by about 15 nm (80 eV) and an increase in the overall intensity.

2.4 Optical and Electron Spectroscopies

It has been discussed up till now the effect of the plasmonic response of nanoparticles due to scattered light. However current work also studies nanoparticles using Electron Energy Loss Spectroscopy. The workings of EELS was shown in the introduction chapter, as well as the basics of spectrum imaging. Here we will highlight the benefits of EELS over optical methods and show the differences in the two methodologies. Far field optical microscopes are limited by the diffraction limit to a spatial resolution of about half the wavelength of light, however electron microscopes, as discussed in the introduction chapter, can reach sub angstrom resolution [82]. Using both EELS and a scanning transmission electron microscope allows precise structural information to be obtained simultaneously with the resonance modes. EELS also has the advantage over light based techniques that so called dark modes, within optical measurements, can be detected [26]. A dark mode is a mode which has no (or a very small) net dipole moment, and thus does not couple to light, thus appears "dark" or non-existent when light is the probing radiation. This means optical techniques are not sensitive to non-dipolar modes. Plasmonic modes can thus be categorised as either radiative (a bright mode) or sub-radiant (a dark mode), depending on the probing radiation. By calculating the dipole moment of a mode we can assess whether such a mode would be dark or not, and thus whether it would couple to light [83].

Figure 2.3 shows a typical example of EELS data from a simple plasmonic structure. In EELS measurements a high energy electron beam passes through a sample and the energy lost by these electrons is measured as a function of frequency of occurrence (see the introductory EELS Section 1.5). By scanning a highly focused electron beam across the surface of a nanoparticle, a 2D map can be obtained with each position consisting of a loss spectra, Figure 2.3a. In this example we have shown three spectra obtained by positioning the electron beam at three different positions on a triangle, the tip (blue), middle (green) and base (red) (Figure 2.3a inset). In the low loss region ($< 10\text{eV}$) peaks appear as a result of the plasmonic resonance but, importantly, not all peaks appear to be excited at all positions. This shows the need for scanning the electron beam across the surface of the nanoparticle in order to probe all possible modes. By scanning, our data consists of a 3D data cube with a loss spectra at each pixel. Thus a 2D intensity map showing the spatial distribution of a plasmonic mode can be generated, as shown in Figures 2.3b, 2.3c, 2.3d, (see Section 1.5.2 on spectrum imaging). In this example we see two distinct modes, one concentrated at the tips of the triangle, Figure 2.3a, and the other in the middle of each of the vertices, Figure 2.3c. The middle mode is a hybridization of the other two. This simple example shows the power of EELS to study surface plasmons, however there are some disadvantages of EELS over optical methods. EELS does not give a measure of the photonic density of states and can be insensitive to coupling modes, like those seen in the previous section 2.3. However both the spatial and energy resolution both make it the ideal method to probe structural effects in this work.

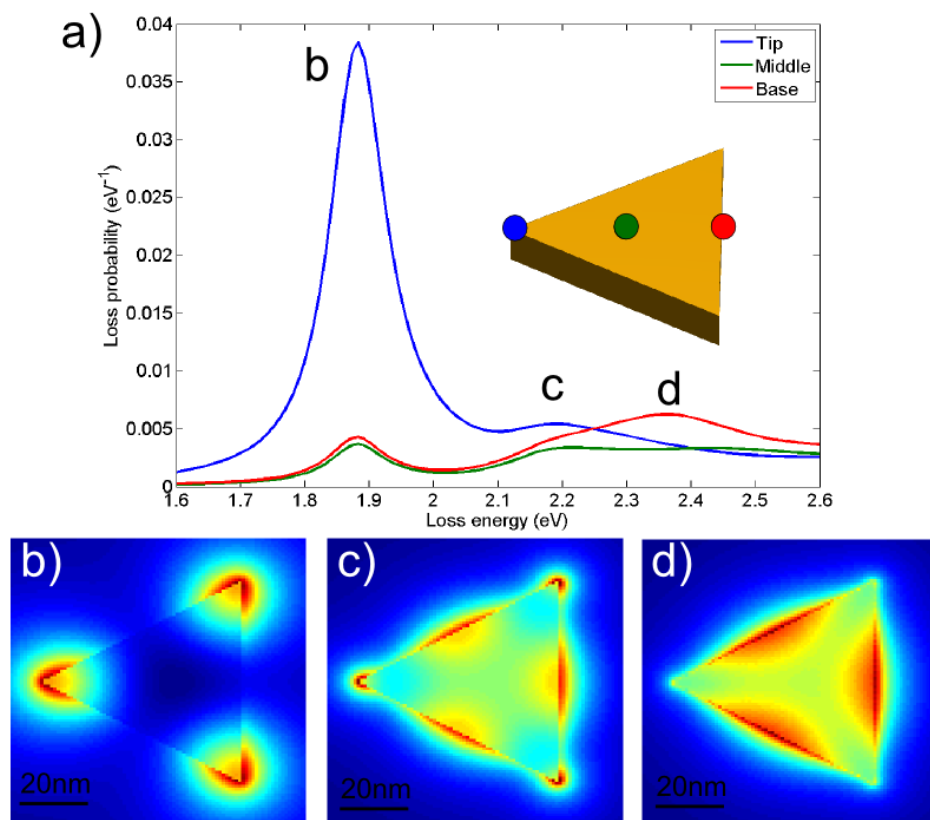


Fig. 2.3 a) Typical EELS spectrum showing the three resonant modes of a gold patterned nanotriangle of width 80nm. The electron beam is positioned on the points shown in the inset. The 2D loss maps produced at each of the three resonant modes in the EELS loss spectra are shown at energies of b) 1.87 eV, c) 2.19 eV and d) 2.36 eV.

2.5 Babinet's Principle

Babinet's principle is a classical concept based on the diffraction of light. It states that diffraction from a hole should be the same as from its solid counterpart [84, 85]. Applied to plasmonics this means that the modes observed in a metallic nanoparticle should be similar to those seen in a hole of the same shape [86]. However this is only true for 2D materials, and as will be shown in the proceeding sections, due to the fabrication process our nanoparticles have 3D shape. Figure 2.4 shows an example of Babinet's principle for a triangle and triangular hole. We see similar modes appear for both the positive and hole structure however they appear at different energies. The mode for the positive structure, Figure 2.4a, appears at 1.7eV whereas the same mode for the hole, Figure 2.4a, is shifted to 2.1eV . These two modes would be expected to be closer in a simulation than experimentally. In a simulation of a hole it is the boundary of the material that the hole is in that may effect the energy the mode appears in the spectrum. Ideally the hole would be in an almost infinite medium, however this is not possible in a simulation. If there is a triangular hole in a square material then the triangular modes from the hole, at a particular energy, can couple and shift with the square modes from the boundary at a different energy, similar to what was shown for the coupled spheres in Section 2.3. To overcome this a hole could be put in a material which has dimensions much greater than the dimensions of the hole, however this would require much greater computational time. As an example, a hole with a boundary which was ten times the dimensions of the hole, took 12 hours to run.

In an experiment it is difficult to get the shape and size of a hole and a nanoparticle identical and as such similar modes seen in a experimental nanoparticle and its hole counterpart will vary in energy and shape due to the shape variations, with coupling and breaking of 2D symmetry as will be examined in this chapter. The positive and negative nanoparticles being

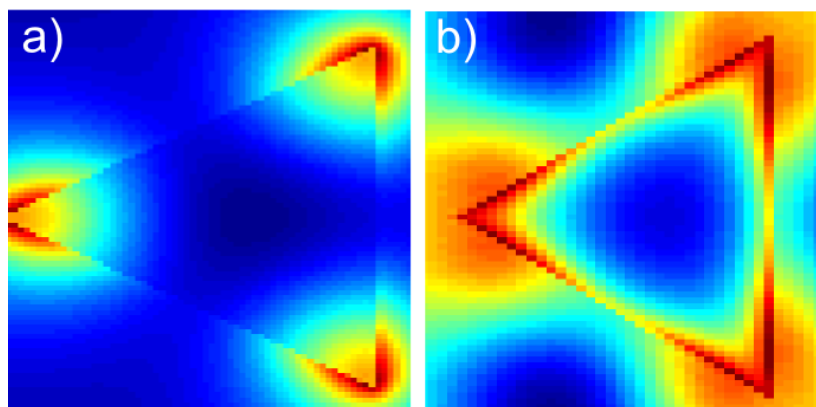
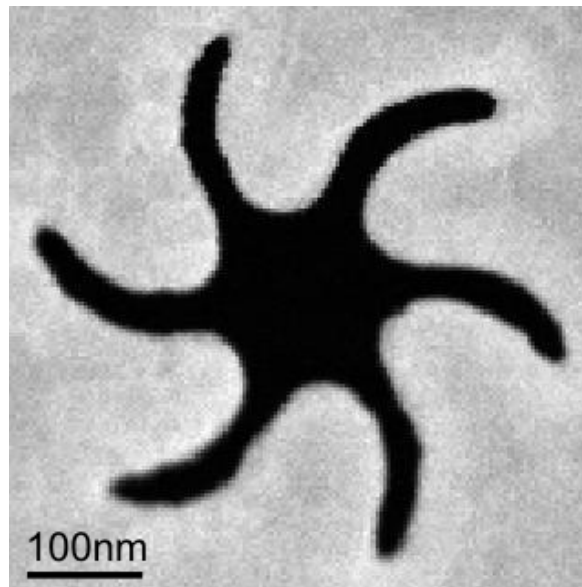


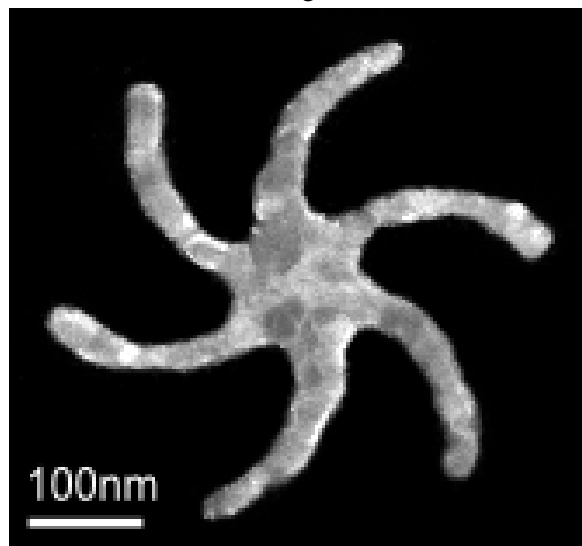
Fig. 2.4 An example of Babinet's principle for a) a nano-triangle and b) atriangular hole. Similar modes appear for both the positive and hole structure however they appear at different energies. The mode for the positive structure appears at 1.7eV whereas the same mode for the hole is shifted to 2.1 eV .

studied in this work are shown in Figure 2.5. They are made from the noble metal gold and have a sixfold shuriken, “nanoswirl”, shape. They are both approximately 60 nm thick and

have a diameter of around 500 nm. They are patterned using electron beam lithography and e-beam evaporation onto a silicon nitride (SiN) substrate (not shown in the figures).



(a) Negative



(b) Positive

Fig. 2.5 The a) negative and b) positive nano-swirl structures which are being studied in this work. Each swirl is approximately 60 nm thick and has a diameter of around 500 nm. Deviations in the actual structure, including the surface roughness and edge imperfections are the result of the fabrication process and will be studied in this chapter.

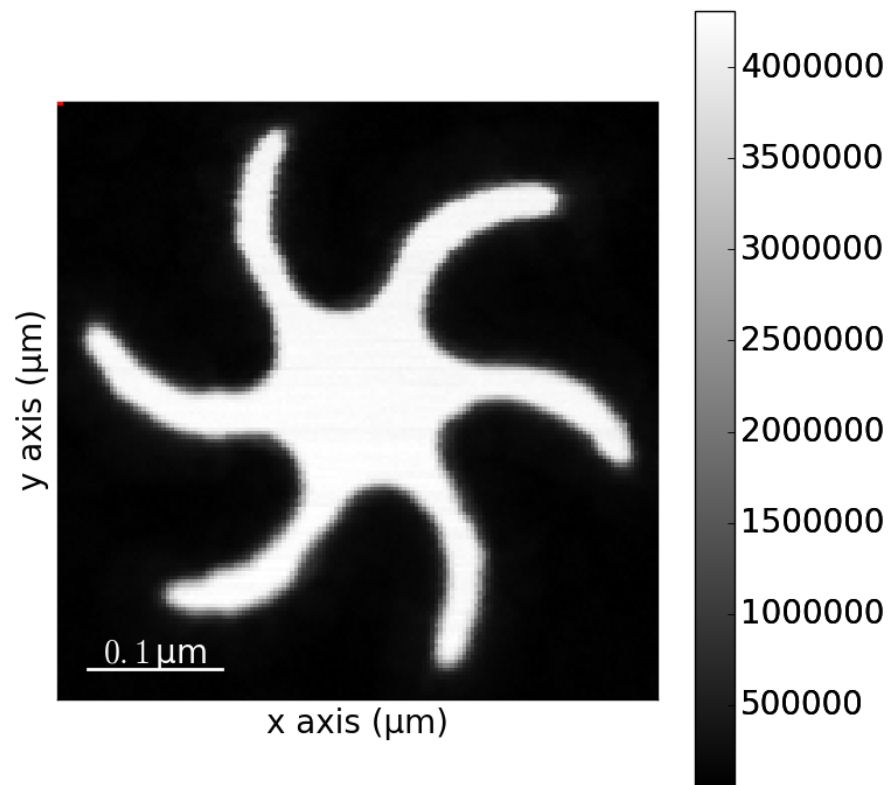
2.6 Chiral Metamaterials

Metamaterials are artificial structures which have been engineered to possess electromagnetic properties that do not exist in such a material in nature. Such materials have been used to make bulk properties appear in a material as a result of small effects on the nanoscale for

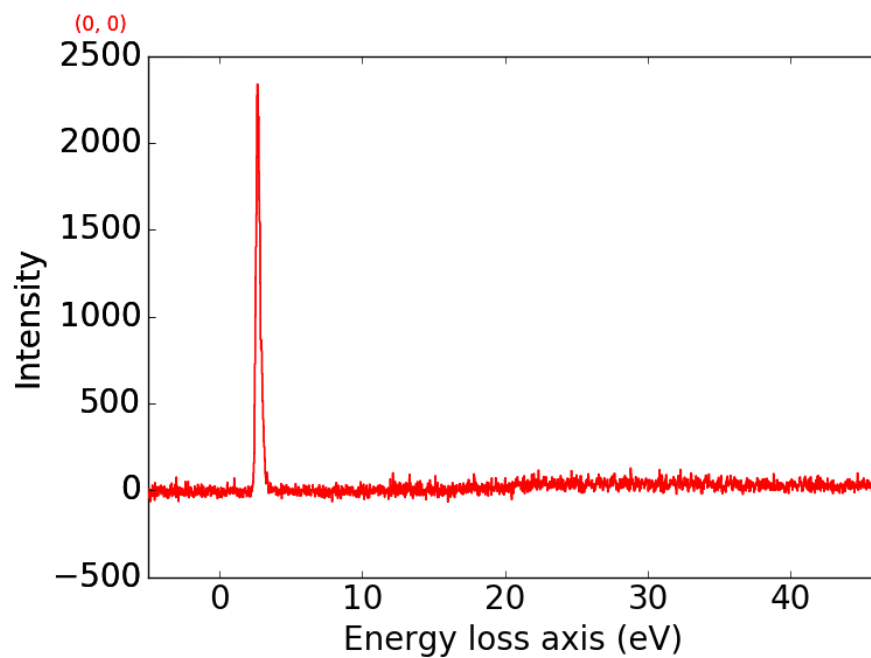
example using surface plasmons to manipulate a metamaterials optical response. An array of holes, with a unit cell much smaller than the wavelength of light, on a material which supports surface plasmons could transmit or absorb light differently from the bulk as a result of the SPs it supports. With this idea comes the ability to tune the optical properties of a metamaterial, simply by controlling the surface plasmon modes it supports and thus its interaction with light. Babinet's Principle would suggest that a hole structure can support similar modes to those seen in a positive structure, however an array of holes is easier to template and mass produce than solid structures. For these reasons it can be reasoned that hole structures are the ideal candidates for use of SPs in metamaterials. One of the main goals of engineering metamaterials is to develop negative refractive index materials which have a unique interaction with light. It has been found that a negative refractive index can arise in a 3D chiral metamaterial made up of planar chiral metal sheets [87].

2.7 Experimental Details

In the next few sections we will study data sets obtained experimentally. The nanoparticles studied were made using electron beam lithography and e-beam evaporation. They should be of similar size, however the relatively small feature sizes of the nanoparticles make it difficult to obtain a precise shape. The experimental EELS data was taken on a JEOL ARM200F scanning transmission electron microscope operated at 80 keV. Our scanning transmission electron microscope is fitted with a cold field emission electron gun, the benefits of this type of gun has been discussed in Section 1.4.1. It is also fitted with a GIF Gatan Quantum ER spectrometer which performs the Electron Energy Loss Spectroscopy. The EELS data in this section was collected at a dispersion of 0.025 eV/channel and spatial resolution of 3 nm. The dwell time was 50 ms and the convergence and collection semi-angles were 29 and 36 mrad. Figure 2.6 shows an example of a typical data set that will be studied. It is a spectrum image, made up of two parts as discussed in Section 1.5.2. The as acquired data consists of the 2D spectrum image (Figure 2.6a) which is the integrated intensity of the energy loss profile (Figure 2.6b) at each pixel. The spectrum image appears bright inside the hole and dark outside, this is due to the electrons which lose very little to no energy as they pass unaffected through the hole. These zero-loss electrons are the dominant feature in every pixel, and the next few sections will discuss post acquisition techniques which will seek to remove this dominant effect to reveal the small features typical of plasmonic losses due to this hole. As acquired only two features can be seen in the loss spectrum Figure 2.6b, but we expect post processing to reveal more modes. The first step in processing the data will be to deconvolve the data to remove the dominant zero-loss.



(a)



(b)

Fig. 2.6 An example of a typical spectrum image obtained using the experimental conditions given in the text, showing a) the 2D spectrum image showing the integrated intensity of the energy loss at each pixel and b) a typical loss spectrum at a single pixel. We can see that the high intensity zero-loss peak dominates the spectrum.

2.8 Richardson-Lucy Deconvolution of Experimental Data Set

Richardson-Lucy deconvolution is a method of deconvolution that began with applications in astronomy and has expanded to most 2D image processing techniques [88][89]. In terms of EELS the Richardson-Lucy method has been used to improve energy resolution of EELS data acquired using a CCD detector [90], correct the point spread function of a CCD detector [91] and has been used to improve the resolution of EELS in order to map surface plasmons [20]. As discussed in the introduction chapter it can be difficult to probe the low energy range related to optical excitations as the plasmonic signal can lie too close to the zero-loss peak. Due to inherent energy spreading of the electron source, despite the source being a cold field emission electron gun, these signals can be lost and will be present in any instrument. Thus post processing techniques are required in our analysis. The R-L method is an iterative procedure for deblurring by a known point spread function, ρ_{ij} . In our dataset the point spread function is a zero-loss spectrum obtained under the same experimental conditions as our plasmon data, but from an image taken in a vacuum with no sample. A typical point spread function, or vacuum spectrum, will appear as in Figure 2.6b with the intense zero-loss peak, without any further peaks caused by the presence of the sample. This spectrum will thus have the same inherent energy spreading as any data set we take but will not have any features due to plasmonic losses associated with the sample and can be used simply as a background. This point spread function is deconvolved from each of the energy loss spectra at each pixel in the spectrum image. By iteratively solving

$$p_i = \sum_j \rho_{ij} q_j, \quad (2.1)$$

where p_i is the observed intensity at pixel i and q_j is the actual value at pixel j . The number of iterations used in the calculation of q_j determines the accuracy of the R-L method. Too few will not sharpen spectral features by much but too many will introduce noise in the data which will iteratively become worse. Thus a compromise will be made between having enough iterations to reduce the energy spread of our gun but not too many as to introduce anomalies. The importance of the R-L method in our work is shown in Figure 2.7. This shows an experimentally obtained spectrum showing the decrease in FWHM of the zero-loss peak from around 0.32 eV for the spectrum before R-L deconvolution (green) to around 0.10 eV after 60 iterations of an R-L algorithm (blue). With this decrease in width also comes the visibility of another modes, at an energy of 0.9 eV, which was previously lost due to its proximity to the zero-loss peak, merely appearing as a blip in the shoulder of the curve before the deconvolution. This mode, which was at first obscured by the zero-loss, will be present in many of the pixels in the spectrum image, although not a dominant feature, like the zero-loss.

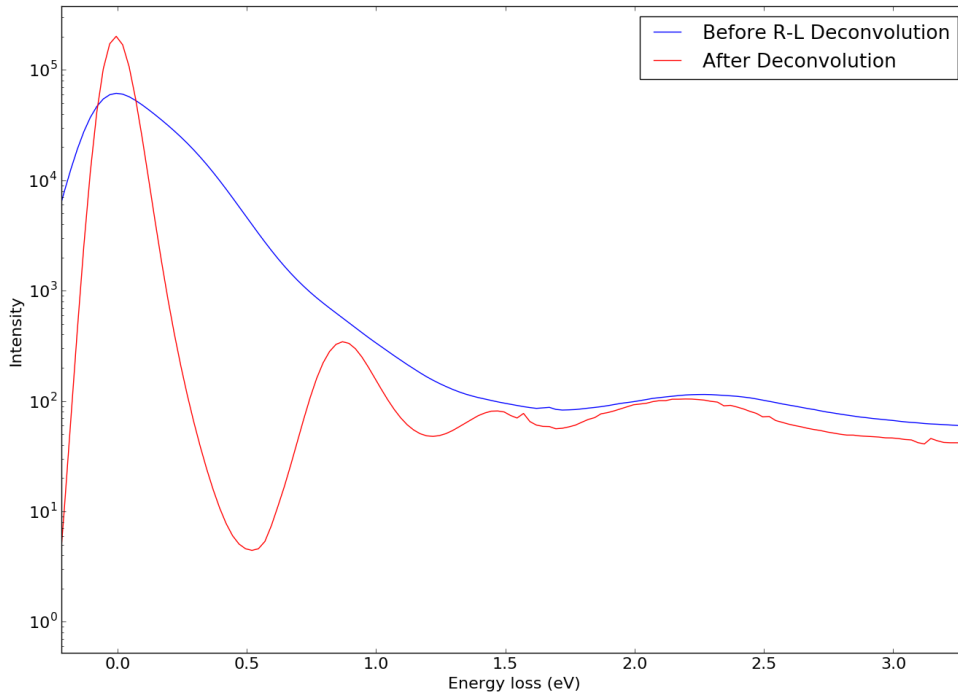


Fig. 2.7 Mean spectrum before (blue curve) and after (red curve) performing Richardson-Lucy deconvolution. The width of the mean zeroloss peak before deconvolution is 0.321 eV and the width after is 0.103 eV. We see after deconvolution the appearance of peaks which were obscured by the zeroloss in addition to some noise at higher energies.

2.9 Matrix Factorization of Experimental Data Set

A further post processing technique which is used to extract useful information from our EELS data is matrix factorisation or decomposition, where it is assumed our data set is made up of linearly independent factors. Matrix factorization is a common linear algebra technique used to denoise EELS data sets. It works on the assumption that a data set consists of factors which can be decomposed in order to show the modes which make up a set. The method used in this work is non-negative matrix factorisation (NMF) [92] [93], where the components separated from the data set are set the strict condition that they must be non zero, i.e. made up of non zero matrices. This ensures that the components are made up of real features, as negative intensity has no physical meaning in our work. Thus NMF has an advantage over other spectral decomposition methods, such as single value decomposition and principle component analysis, in our work as the results are constrained to be physically real, a condition the former two techniques do not stipulate. NMF has being used for varying data analysis techniques ranging from text data mining to spectral unmixing [94]. In terms of EELS NMF has also been used to reduce noise and extract plasmonic modes in nanoparticles [95] which highlights its suitability in our work. Figure 2.8 shows the results of performing NMF on the positive nanoparticle shown in Figure 2.5b. The black curve shows the data

after R-L deconvolution has been performed but before we have performed the NMF. For convenience we have cut off the data after the zero loss to better show the plasmonic modes. By running an NMF algorithm we extract four factors, labeled DF0-3. Each of these modes, and those of the negative particle will be discussed in the next section.

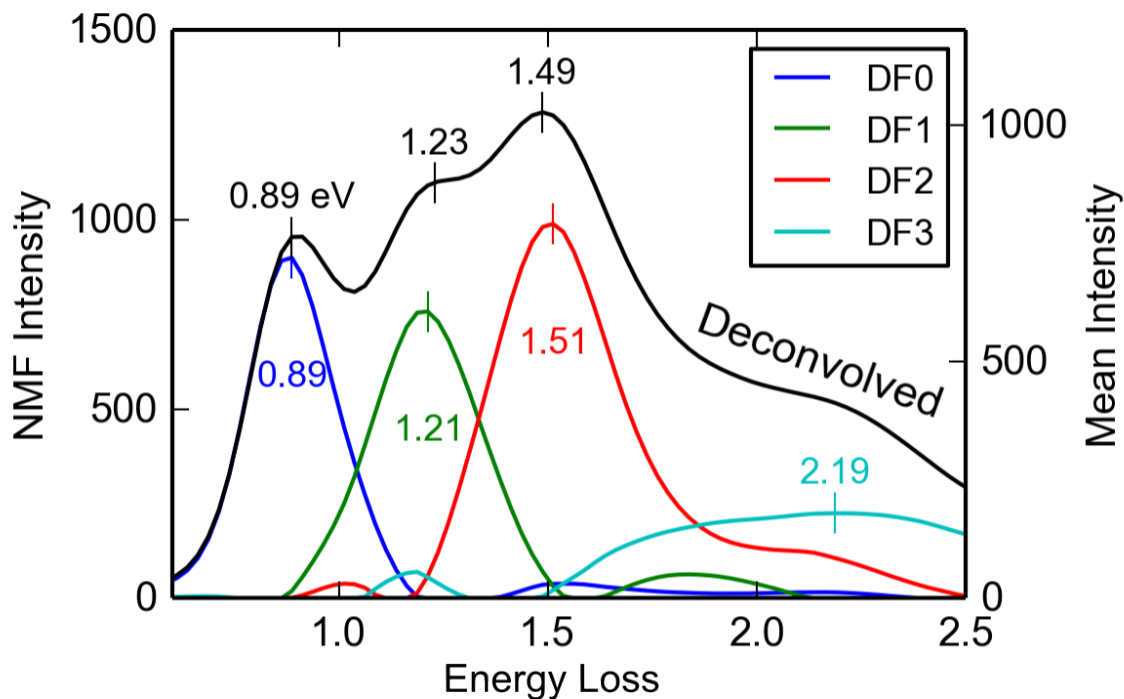


Fig. 2.8 Example showing the four factors found after applying non-negative matrix factorisation on the experimental positive nanoparticle. The black curve is the deconvolved data before the factorization is performed.

2.10 Experimental Modes

Figure 2.9 shows the spatial modes which correspond to the peaks shown in Figure 2.8. We see the first mode, DF0, corresponds to a mode with a peak energy of 0.89 eV. It has a spatial intensity which is concentrated on the tips of arms of the nanoparticle. An important point to note is that the intensity is inhomogeneous and we see a higher intensity on two of the arms when compared with the others. This is due to structural imperfections which will be discussed in the next chapter and represents a splitting of a mode. The second mode, DF1, corresponds to a mode with a peak energy of 1.21 eV. The mode has intensity which is localised around the base of the shuriken and not along the arms. The third mode, DF2, corresponds to a mode with a peak energy of 1.51 eV and is the first example of a breathing mode, where we see a node appearing along the arm, where the intensity peaks twice, half way along the arms and at the tips. The final loading, DF3, corresponds to a mode with a peak energy of 2.19 eV and is almost homogeneous about the nanoparticle: this is a bulk mode.

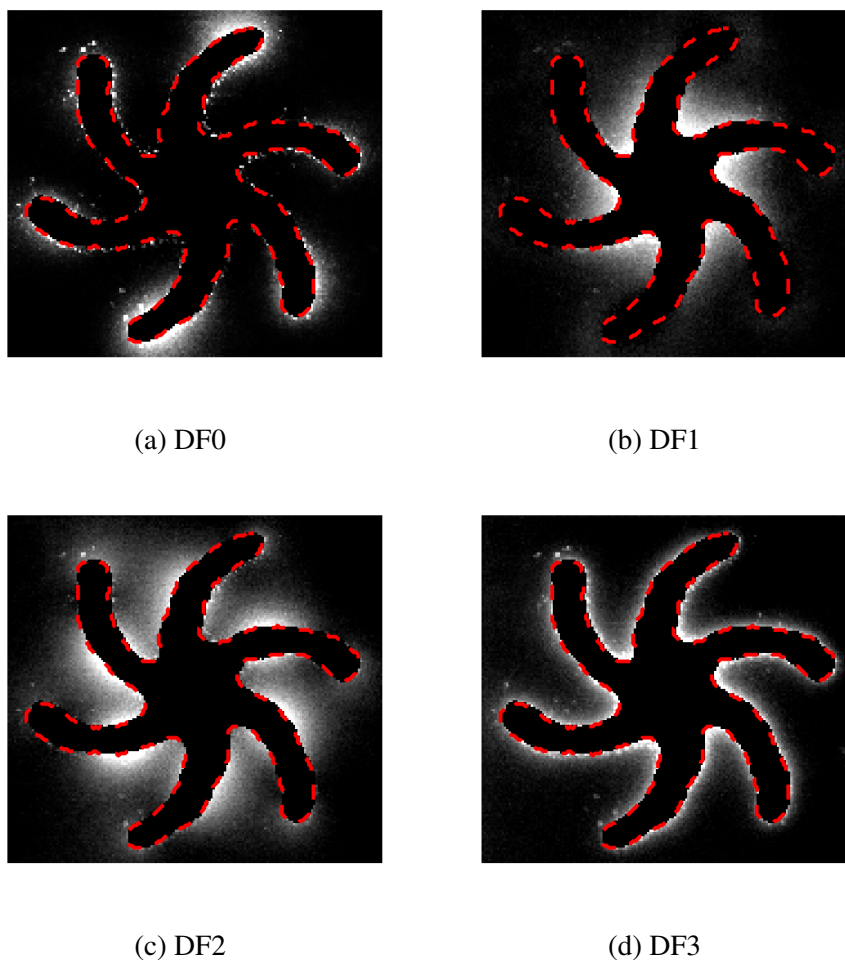


Fig. 2.9 The decomposition loadings from the NMF decomposition corresponding to spatial distributions of bound charge on the surface of the positive nanoparticle. The red dashed line indicates the location of the particle boundaries, which have been masked to better show the intensity variations. The energies are a) 0.89 eV, b) 1.21 eV, c) 1.51 eV and d) 2.19 eV.

We can contrast the positive modes with those obtained after performing NMF on the negative particle. Figure 2.10 shows the results of NMF performed on the EELS data set from Figure 2.5a. The figure shows five components. The first component 2.10a shows a high intensity around the edge of the hole structure, and is isotropic along each of the arms. This mode appears at 0.87 eV and is the first mode seen in the spectrum Figure 2.7. It is comparable in energy to the first mode seen for the positive structure, however the intensity does not appear to be as inhomogeneous in the negative structure. The second factor 2.10b shows a high intensity around the central region, however in this case there is a node along each of the arms. This appears at 1.47 eV and again it is similar in shape to the mode seen at 1.21 eV in the positive structure however there is a 0.26 eV shift in energy.

This similarity in energy and spatial distribution of the modes of the two opposite nanoparticles shows evidence that our structures are related and show similar plasmonic response, though there is a shift in the energies of the modes. The next mode is intense around the edges and due to the appearance of a higher intensity in the gold around the arms, it's clear this mode is due to the bulk gold and isn't confined spatially to the edge of the hole. The next factor Figure 2.10d is intense around the central region with a node along each of the arms shows a similar intensity distribution as the mode seen at 1.51 eV in the positive nanoparticle, however these appear to be two different breathing modes. The positive breathing mode has a trough at the centre of the nanoparticle, whereas the negative mode has a peak. These factors show fine structure that is within our experimental data set, and not only shows the ability of EELS to study negative plasmonic nanoparticles, but also shows the ability of EELS to quantify individual modes. It also shows the importance of NMF in our work to display features that are not easy seen in the acquired data set. These modes which can be extracted using NMF can be obscured in the experimental data, as they can lie close together or overlap. Despite some similarities in the modes observed, we can see that there are shifts and changes in the spatial intensity of the modes that exist on the positive structure and negative structure. It was shown in the introduction section that size plays an important role in what modes can be supported on a plasmonic nanoparticle, thus deviations in the size between the two nanoparticles could play a role in the differences observed in the results. There is also a difference in the structures caused by the fabrication processes, the nanoparticles have complex three dimensional shape which can play a role in what modes will be observed. This will be studied in the next chapter where we will simulate EELS data for two identical positive and negative nanoparticles, and also investigate the role of structural imperfections in the modes can exist on these structures.

2.11 Thickness Calculation of Negative Nanoparticle

This section uses the nanoparticles studied in this chapter to obtain an accurate thickness profile to be used in the simulations in the next chapter. In the next chapter we will simulate EELS data of positive and negative nanoparticles, which have the same three dimensional shape as those studied here. In order to simulate a realistic plasmonic nanoparticle a thickness calculation must first be done on our experimental data. In this work we chose to use the log-ratio method to calculate a thickness from an EELS dataset [96]. For this we use the ratio

$$\frac{t}{\lambda} = \ln \frac{I_0}{I_t} \quad (2.2)$$

where I_0 is the elastic intensity, made up of the area under the zero-loss peak and I_t is the total integrated intensity over the energy loss axis. For our experimental data this equation must be broken down into the three regions shown in Figure 2.11a, labeled I_0 , I_{t1} and I_{t2} . First the zero-loss intensity, I_0 is calculated from the EELS spectrum image, this will be the

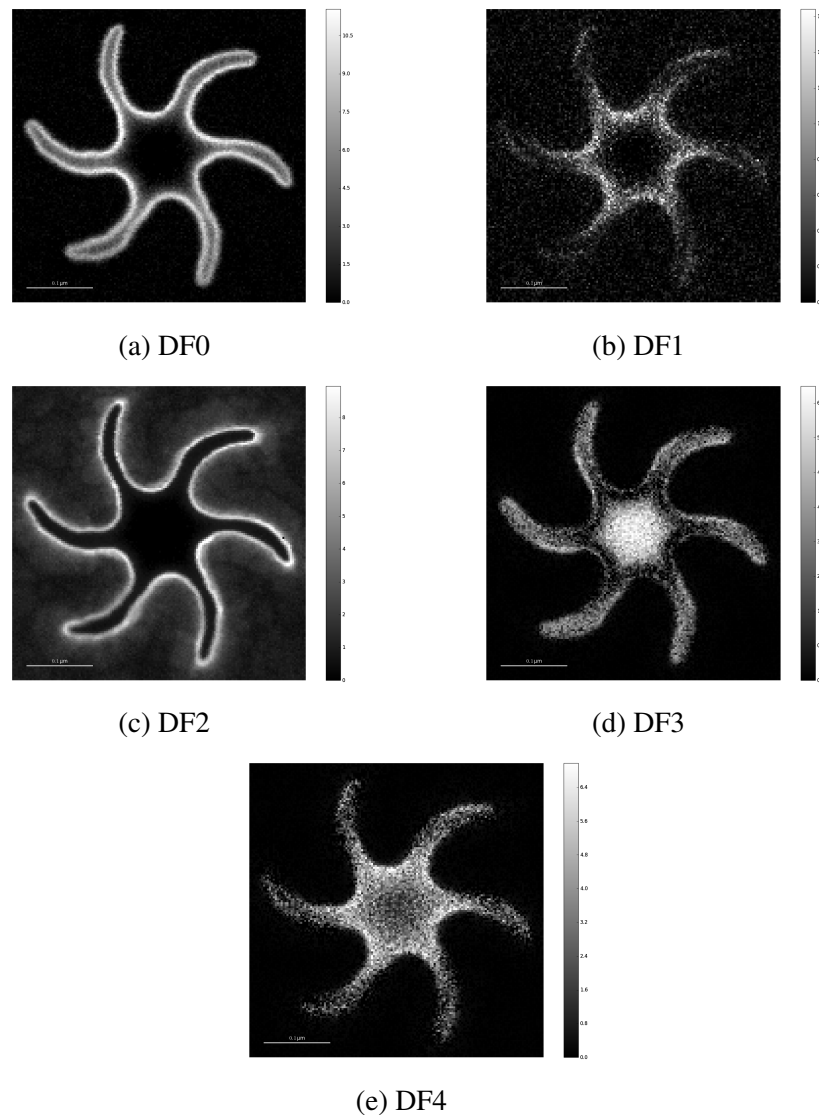


Fig. 2.10 The decomposition loadings from the NMF decomposition corresponding to spatial distributions of bound charge on the surface of the negative nanoparticle. The energies are a) 0.9 eV, b) 1.32 eV, c) 2.21 eV, d) 2.34 eV and e) 2.45 eV.

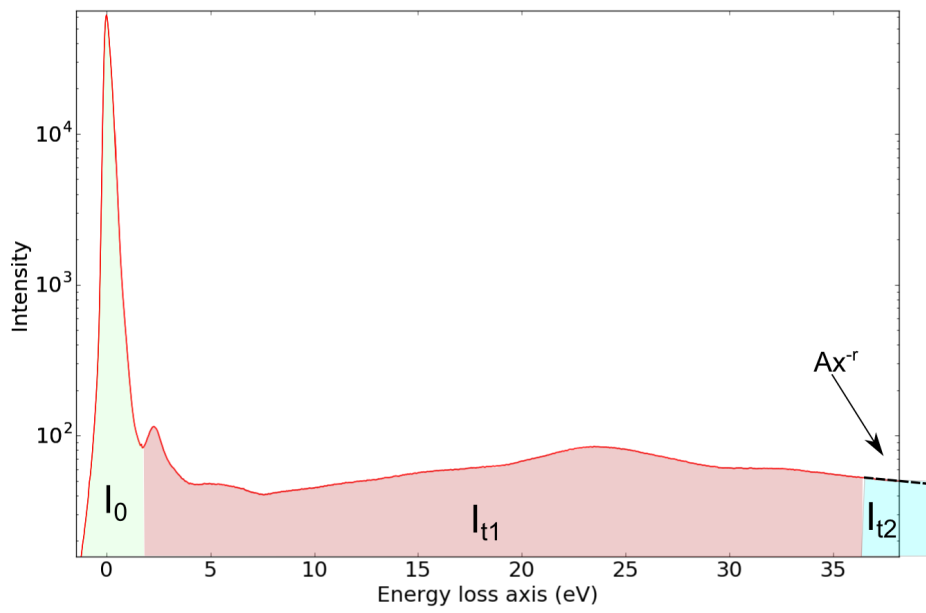
most intense feature and thus have the highest value, as can be seen in Figure 2.11b. To do this the inflection point is calculated in each pixel of the spectrum image, which is the energy at which the spectra change from the elastic region to the inelastic region. This threshold energy is the boundary between the I_0 and I_{t1} regions. The overall intensity is then calculated in two parts, the zero-loss intensity plus the inelastic intensity. This inelastic intensity, made up of I_{t1} and I_{t2} can be calculated by taking the area under the curve past the elastic threshold. However, our datasets are limited to a maximum loss of 40 eV where the intensity of the electron energy loss has not yet reached zero. This means the integrated intensity will be lower due to this cut off not include any high loss data. To compensate for this, a power law taking the form Ax^{-r} , corresponding to the background fall off, is calculated for the latter part of the loss data. This is done in post processing by fitting a model curve at a point in

the spectra past which the data begins a fall off, which is also past any further plasmonic features. This region is indicated with an arrow in Figure 2.11a and would extend far past the edges of the data to where the intensity falls to zero. The two inelastic regions I_{t1} and I_{t2} , shown in Figure 2.11c and d respectively, are most intense about the edge of the hole, as these energies represent scattering events in the gold. I_{t2} also begins to show the grain structure of the gold, this is due to the powerlaw extrapolating and including the bulk gold effects. Figure 2.11e shows the values for $\frac{t}{\lambda}$ calculated from Eqn 2.2 using the regions I_0 , I_{t1} and I_{t2} . An important feature of values in Figure 2.11e is the intensity variation around the arms in the gold. This gradual, rather than sharp, thickness decrease as we approach the hole is a feature of the electron beam lithography patterning. This thickness calculation is used to make both the negative and positive meshes which will be used to simulate EELS data in the next chapter in order to better test Babinet's principle for our nanoparticles.

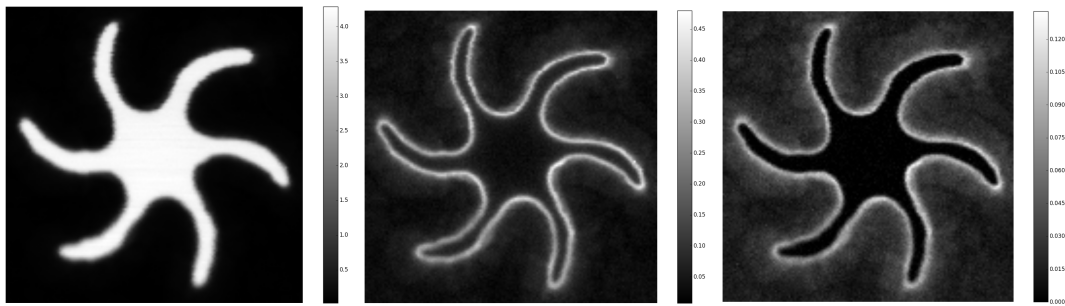
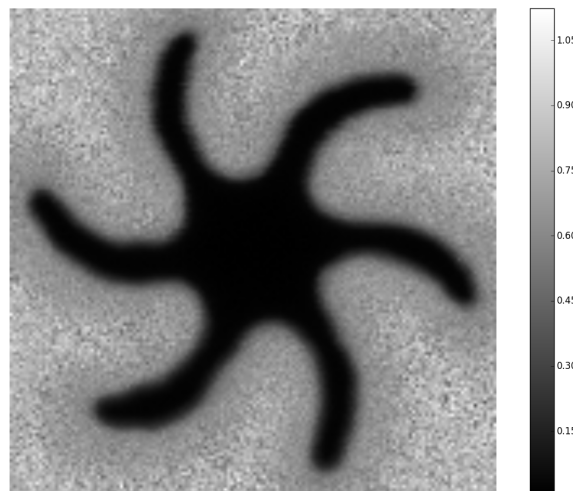
2.12 Conclusion

In this chapter we have studied the modes which can be supported by two related plasmonic nanoparticles, a positive and negative structure. It was identified that post processing would be required to the exact the plasmonic modes as they lay near the intense zero-loss region in the EELS data. Deconvolution was shown in Figure 2.7 to reveal modes which were close in energy to the zero-loss which were obscured before deconvolution. The second processing technique used was to decompose the data into non negative factors using NMF which revealed distinct modes with spatial intensity variations. These processing techniques were performed on a real data set in order to highlight real improvements which could be made to the data.

In order to study if Babinet's principle agreed with our work we studied the modes in two plasmonic nanoparticles, a hole and a positive nanoparticle. Figures 2.10 and 2.9 showed a comparison of the modes which could exist on the negative and positive nanoparticles respectively. We saw that while the intensity distribution of the modes was similar, there were shifts in energy of around 0.2 eV for some of the modes. The shifts can be seen to be the result of complex 3D structure. As discussed in the experimental details the small features of these nanoparticles means they are never going to be exact in shape or size. Small deviations in the structure (as will be seen in the next chapter) lead to the shifts in energy of the modes. The fact that the modes of the positive and negative had similar spatial distributions proves that Babinet's principle works for our results.



(a)

(b) I_0 (c) I_{t1} (d) I_{t2} 

(e) tol value

Fig. 2.11 a) Regions of the spectrum used in the thickness calculation. b) I_0 : elastic intensity, which includes the zero loss. c) I_{t1} : inelastic region before the loss falls off at as a power-law. d) I_{t2} : To includes losses past the upper cut off of the image a power law is used to extrapolate the region and summed. e) The final values of $\frac{t}{\lambda}$

Chapter 3

Simulated Comparison of Chiral Gold Plasmonic Nanoparticles.

3.1 Introduction

This chapter outlines the work carried out in simulating EELS data of plasmonic nanoparticles. It was seen in the previous chapter that the nanoparticles studied in this work have a complex 3D shape thus they deviate from the simple planar structures more commonly found in the literature. In this work we simulate EELS data of realistic structures. We begin by studying the effects of edge imperfections on three shuriken shaped gold nanoparticles, one of which has an idealised shape, with sixfold symmetry and in-plane symmetry whilst the other is an experimentally realistic particle, which has neither in-plane nor sixfold symmetry. These two nanoparticles are taken to show the realistic effects of shape imperfections when studying real plasmonic particles, where fabrication limitations are accounted for. We will show that the two particles differ in the resonant energies and spatial distribution of surface plasmons due to these structural differences. We will show that differences in bound surface charge which result from the different plasmon modes give rise to a difference in local electric fields which these particles produce. This difference is important as one of the exciting applications of plasmonic nanoparticles is as sensors of chiral molecules. Thus the shape and strength of the electric fields created by the nanoparticles will be an important detail to be studied.

The third nanoparticle studied in this chapter is an exact counterpart to the hole structure studied in the previous chapter. We have taken the experimental hole from the previous chapter and simulated both it and the positive nanoparticle which is an exact template of it. Fabrication effects were present in the positive and negative nanoparticles studied in the previous chapter, leading to differences in shape and size which likely played a role in the differences seen in the modes. This third nanoparticle will be used to given an accurate comparison between the hole and nanoparticle and will improve our understanding of the role of Babinet's principle in our work and the modes which are supported by both a positive and negative nanoparticle and complement the results of the previous chapter.

This chapter is organised as follows; first we detail the nanoparticles which will be studied in this work and details of the mesh used. We will then perform a symmetry analysis of the structures, both for the positive and negative cases and this symmetry analysis will allow us to predict the modes which will be seen in structures. The first simulation we will perform in Section 3.5 will involve calculating the eigenmodes of the surface charge on our nanoparticles. This will give a quantitative grouping of the modes in our structures and highlight differences due to the imperfections in terms of dipole moment and local electric field strength. In Section 3.6 we perform a full BEM calculation for each of the structures and compare the mode's spatial distributions, intensities and energies. We complete the chapter with a study of the effect of adding a substrate to the positive nanoparticle as a further 3D effect which has an impact on the modes observed.

3.2 Edge Imperfections and Roughness in a Realistic Nanoparticle

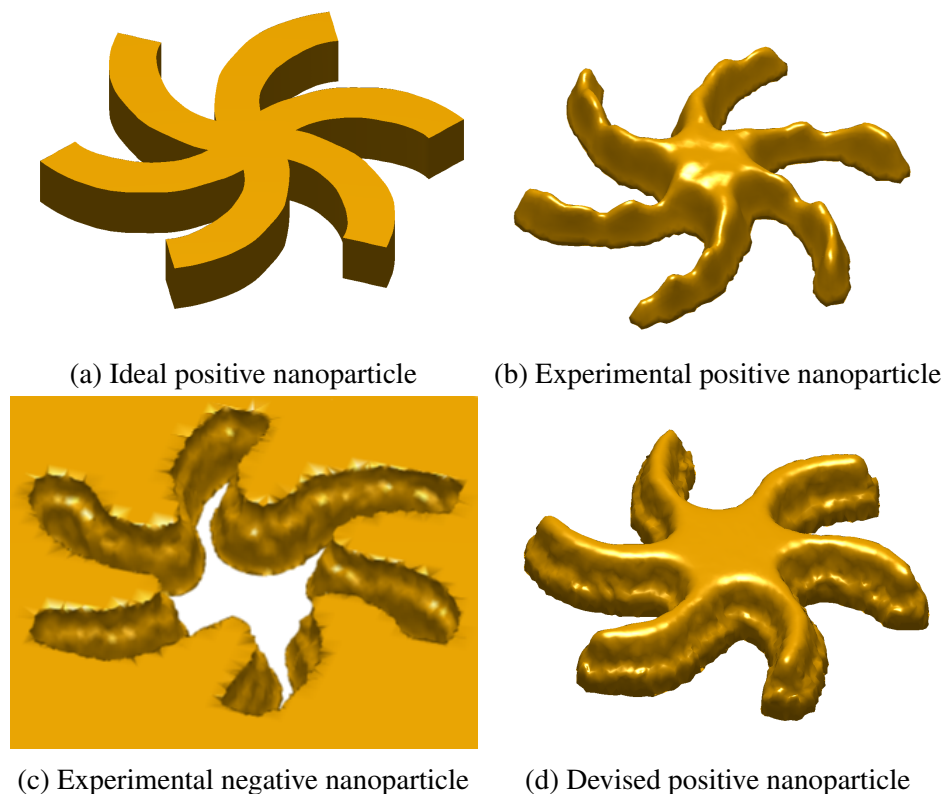


Fig. 3.1 The gold plasmonic nano-swirl structures which are being studied in this work. Details of each shape are given in the text. Each swirl is approximately 60 nm thick and has a diameter of around 500 nm. Deviations in the actual structure, including the surface roughness and edge imperfections are the result of the fabrication process.

The nanoparticles studied in the introductory sections in this work were idealised, simple structure which were free from the roughness and imperfections which exist in real nanopar-

ticles studied experimentally. Much of the literature on plasmonic nanoparticles deals with simple structures, with few studies on the effects of surface roughness and edge imperfections. This work will focus on what happens when nanoparticles deviate from this ideal structure. The particles being studied are shown in Figure 3.1. There are notable differences between the structures which form the base of this study, which are as follows.

1. An ideal positive nanoparticle.

This structure is an ideal case, which is not experimentally realistic. It has 2D planar symmetry, six fold symmetry and no roughness or defects. Any nanoparticle which could currently be fabricated would have some breaking of symmetry caused by roughness and defects during the fabrication process which is unavoidable due to the small features being patterned.

2. An experimentally realistic positive nanoparticle.

This structure has been modeled using the $\frac{t}{\lambda}$ data from Section 2.11 for an actual experimental dataset, thus is experimentally realistic. There are thickness variations along the arms, 3D roughness and the only symmetry element the nanoparticle has is the identity element (rotation by 360 degrees).

3. An experimentally realistic negative nanoparticle.

This structure has been modeled using the $\frac{t}{\lambda}$ data from Section 2.11 for an actual experimental hole dataset, thus is experimentally realistic. The hole has varying thickness, wider at the top and narrower at the bottom with 3D roughness along the walls of the hole.

4. Devised positive nanoparticle.

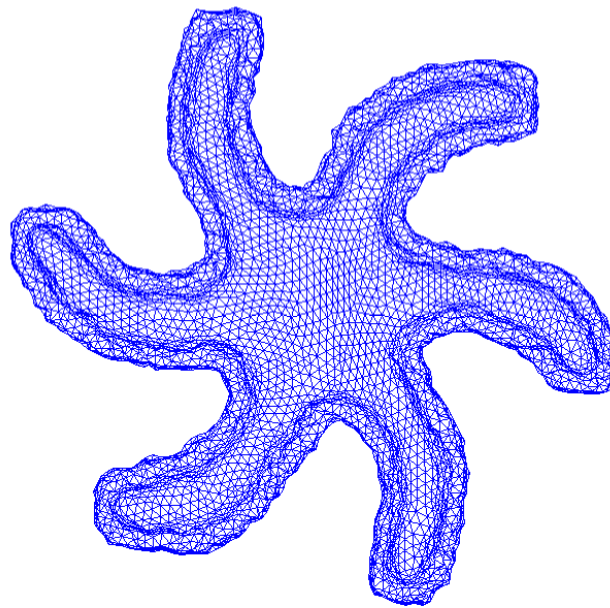
This devised structure is used to simulate a direct comparison with the hole structure. Due to the fabrication processes involved the experimentally realistic positive and experimentally realistic negative particles will differ. In order to investigate if Babinet's principle holds even for these non-ideal shapes (without larger changes in the overall shape being to blame) we have devised this inverse nanoparticle which is simply the structure that would be left after the hole was cut. Thus this structure and the experimentally realistic hole are perfect inverses of one another.

Previous studies have shown the effect of shape variations in plasmonic nano antennas. In these studies it was found that the "ideal" and "fabricated" nanoparticles, due to varying fabrication processes, differed in their optical response and in the near fields, a feature deriving from their different geometric shapes [97][98][99]. It is thus expected that the shapes under study in this chapter should differ in the properties of their SPs and will be used

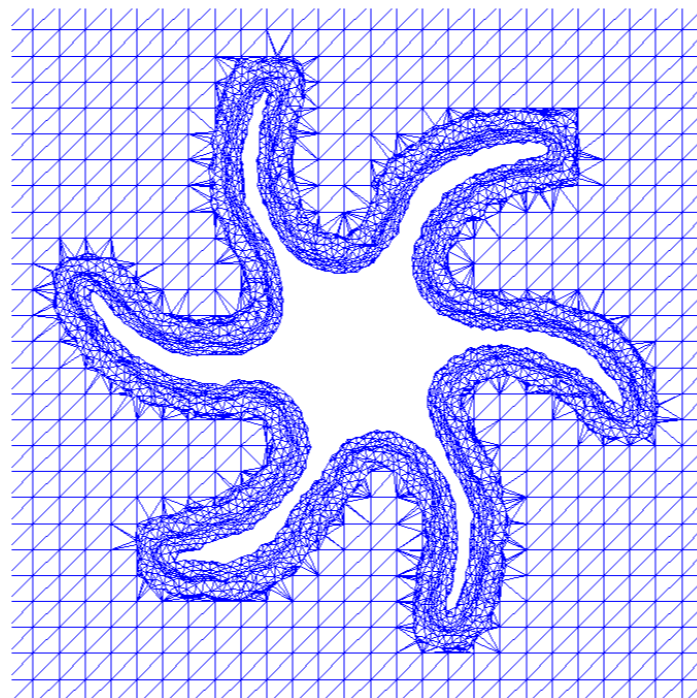
to quantify the effects of the structural differences on the SP Resonance Modes on the surface of nanoparticles. These effects are studied using the BEM method discussed in section 1.3.3. To carry out this method Maxwell's equations must be solved at each point in a mesh which has the shape of the nanoparticle under study. In order to generate an appropriate mesh, experimental data was used to make the realistic particles and ideal shapes used to make the ideal particles. The t over λ method discussed in the previous chapter was used on experimental data to obtain an accurate mesh for our calculations.

3.3 Creating a Mesh

Using the $\frac{t}{\lambda}$ ($\lambda = 4.86\text{pm}$, $E = 80\text{keV}$) values from the previous chapter a mesh is created that will be used in the numerical simulations. The simulations used are part of the MNPBEM toolkit in MatLab. This approach relies on using a triangular mesh to solve Maxwell's equations at each node and compute the surface charge at each point in the mesh (as discussed in Section 1.3.3). It is carried out by considering the nanoparticles by local and isotropic dielectric functions inside and outside the particle, which are separated by a boundary. Making the mesh has some considerations, including the number of points used in the calculation. Figure 3.2 shows the two meshes created to model the experimental negative and devised positive nanoparticles, Figures 3.1c and d respectively. The process of creating the meshes involves creating a mesh of points representing the value t from the $\frac{t}{\lambda}$ values. This mesh is then either closed to create the devised positive nanoparticle or inverted to make the experimental negative nanoparticle. Choosing the right number of nodes to sample is one of the first stages of the simulation. Too few nodes can create artifacts in the data due to under sampling. However, the solution to this is not to simply maximize the sampling points, as too many sampling points can lead to the simulation taking too much time, as the time to run goes with the number of nodes cubed. Thus the first stage of simulation involved a careful selection of the optimum parameters which give rise to both an accurate simulation in a reasonable time. This is done by examining a convergence of the modes to a fixed value and choosing the lowest necessary number of mesh points. The meshes shown in Figure 3.2 each have around 8000 mesh points, which was found to give an accurate solution to the BEM which changed very little as the number of mesh points increased. When comparing simulations to experimental data there are a number of techniques required to process the data to a quality that is comparable with the simulations. This will be discussed below. The first analysis of these nanoparticles is to employ symmetry analysis.



(a) Devised positive nanoparticle mesh



(b) Experimental negative nanoparticle mesh

Fig. 3.2 The meshes used for the MNPBEM calculation. The meshes are for a) the devised positive nanoparticle shown in Figure 3.1d and b) the experimental negative nanoparticle shown in Figure 3.1c.

3.4 Symmetry Analysis

3.4.1 Symmetry Analysis of a Positive Plasmonic Nanoparticle

One of the ways to derive the physical properties of these shapes of nanoparticles is to consider symmetry arguments. The ideal positive shuriken shaped nanoparticle belongs to the C_{6h} point group [100]. This means there is a six fold axis of symmetry which would run through the centre of the nanoparticle. This also means there is a plane of symmetry in the plane parallel to the top face of the shuriken. By knowing the point group of the nanoparticle one can make up a list of symmetry elements, as shown along the top of table 3.1, which is known as a character table for the point group C_{6h} . To build up such a table one simply calculates the set of all symmetry elements which leaves the nanoparticle unchanged (or in an indistinguishable state). With a choice of a basis, such as a Cartesian set, one can build up the table by acting on this basis by each symmetry operation in the point group. This is made simple by using matrices which represent the symmetry operations. The trace, or character χ , of the product of the symmetry operation acting on the basis is then input into the character table, as in Table 3.1. Here the notation used is the Schönflies notation. From this the plasmonic resonance modes can be found by examining the character table and by calculating the irreducible representation. The point group shows how the symmetry operations transform any basis, regardless of which basis is chosen. Thus our choice of basis can be specific to the property which we wish to study. This basis can then be described in terms of irreducible representations, which are the smallest such terms which can describe this basis. In our table there are 4 symmetry species which are given the Mulliken symbols A , B , E_1 and E_2 . Here A defines an irreducible representation which is symmetric with respect to the principle symmetry axis, C_6 in our case. Conversely B defines an irreducible representation which is anti-symmetric with respect to the principle symmetry axis. E_1 and E_2 define irreducible representations which are symmetric and anti-symmetric, respectively, with respect to a vertical mirror plane perpendicular to the principle axis of symmetry. Using these arguments all the plasmonic modes of the structure can be identified using simple geometric arguments and group theory. In this section we will use a basis $|n\rangle$ which describes the plasmon modes as n interacting localized states on each of the six arms in the ideal structure, drawing from a comparison with the tight-binding model used in solid-state physics [101][102]. So we must write the reducible representation described by our basis in terms of irreducible representations. To do this we must calculate the characters of this representation, for each symmetry operation. For example, the identity element has a character 6 as shown

Table 3.1 The character table for the point group C_{6h} , where $\varepsilon = \exp(i\pi/3)$.

	E	C_6	C_3	C_2	C_3^2	C_6^5	i	S_3^5	S_6^5	σ_h	S_6	S_3
A_g	1	1	1	1	1	1	1	1	1	1	1	1
B_g	1	-1	1	-1	1	-1	1	-1	1	-1	1	-1
E_{1g}	1	ε	$-\varepsilon^*$	-1	$-\varepsilon$	ε^*	1	ε	$-\varepsilon^*$	-1	$-\varepsilon$	ε^*
		ε^*	$-\varepsilon$	-1	$-\varepsilon^*$	ε	1	ε^*	$-\varepsilon$	-1	$-\varepsilon^*$	ε
E_{2g}	1	$-\varepsilon^*$	$-\varepsilon$	1	$-\varepsilon^*$	$-\varepsilon$	1	$-\varepsilon^*$	$-\varepsilon$	1	$-\varepsilon^*$	ε
	1	$-\varepsilon$	$-\varepsilon^*$	1	$-\varepsilon$	$-\varepsilon^*$	1	$-\varepsilon$	$-\varepsilon^*$	1	$-\varepsilon$	$-\varepsilon^*$
A_u	1	1	1	1	1	1	-1	-1	-1	-1	-1	-1
B_u	1	-1	1	-1	1	-1	-1	1	-1	1	-1	1
E_{1u}	1	ε	$-\varepsilon^*$	-1	$-\varepsilon$	ε^*	-1	$-\varepsilon$	ε^*	1	ε	$-\varepsilon^*$
	1	ε^*	$-\varepsilon$	-1	$-\varepsilon^*$	ε	-1	$-\varepsilon^*$	ε	1	ε^*	$-\varepsilon$
E_{2u}	1	$-\varepsilon^*$	$-\varepsilon$	1	$-\varepsilon^*$	$-\varepsilon$	-1	ε^*	ε	-1	ε^*	ε
	1	$-\varepsilon$	$-\varepsilon^*$	1	$-\varepsilon$	$-\varepsilon^*$	-1	ε	ε^*	-1	ε	ε^*

by

$$E|n\rangle = \begin{pmatrix} n'_1 \\ n'_2 \\ n'_3 \\ n'_4 \\ n'_5 \\ n'_6 \end{pmatrix} = \begin{pmatrix} 1 & 0 & 0 & 0 & 0 & 0 \\ 0 & 1 & 0 & 0 & 0 & 0 \\ 0 & 0 & 1 & 0 & 0 & 0 \\ 0 & 0 & 0 & 1 & 0 & 0 \\ 0 & 0 & 0 & 0 & 1 & 0 \\ 0 & 0 & 0 & 0 & 0 & 1 \end{pmatrix} \begin{pmatrix} n_1 \\ n_2 \\ n_3 \\ n_4 \\ n_5 \\ n_6 \end{pmatrix}$$

$$\chi_n(E) = 6 \quad (3.1)$$

Where we have acted on each basis element by the symmetry operation. Similarly we can write the character for each of the other symmetry elements in Table 3.1. Thus the characters representing the basis set $\{|n\rangle\}$ are,

$$\chi_n(E) = 6, \quad \chi_n(C_6) = 0, \quad \chi_n(C_3) = 0, \quad \chi_n(C_2) = 0, \quad \chi_n(C_3^2) = 0, \quad \chi_n(C_6^5) = 0, \quad (3.2)$$

$$\chi_n(i) = 0, \quad \chi_n(S_3^5) = 0, \quad \chi_n(S_6^5) = 0, \quad \chi_n(\sigma_h) = 6, \quad \chi_n(S_6) = 0, \quad \chi_n(S_3) = 0. \quad (3.3)$$

We know from group theory that the square of the characters of any irreducible representation equals the number of symmetry elements in the group,

$$\sum_R \chi_i(R)^2 = g \quad (3.4)$$

where R are the symmetry operations of the group g with character χ for the irreducible representation i . Since the sum of the products of any symmetry operation in two different irreducible representations is zero, we can write

$$\sum_R \chi_i(R)\chi_j(R) = g\delta_{ij} \quad (3.5)$$

Table 3.2 SALCs for the point group C_{6h} .

C_{6h}	E	C_6	C_3	C_2	C_3^2	C_6^5	i	S_3^5	S_6^5	σ_h	S_6	S_3
$ n_1\rangle$	$ n_1\rangle$	$ n_2\rangle$	$ n_3\rangle$	$ n_4\rangle$	$ n_5\rangle$	$ n_6\rangle$	$ n_4\rangle$	$ n_5\rangle$	$ n_6\rangle$	$ n_1\rangle$	$ n_2\rangle$	$ n_3\rangle$

where δ_{ij} is the Kronecker delta, which is equal to 1 only when $i = j$ and zero otherwise. Considering a reducible representation χ , we can decompose this representation into irreducible representations via

$$\chi(R) = \sum_q a_q \chi_q(R) \quad (3.6)$$

where q is the number of times the irreducible representation χ_q appears in the reducible representation, and the sum is over all irreducible representations. Now multiplying by the character of the irreducible representation χ_p and summing over all symmetry operations R gives

$$\sum_R \chi(R) \chi_p(R) = \sum_q \sum_R a_q \chi_p(R) \chi_q(R) = a_q \delta_{qp}. \quad (3.7)$$

Therefore the only term which doesn't vanish is

$$\sum_R \chi(R) \chi_p(R) = a_q g \quad (3.8)$$

which gives the reduction formula for reducing a reducible representation χ into irreducible representations χ_p , where the number of times an irreducible representation appears in a reducible representation is given by,

$$a_p = \frac{1}{g} \sum_R \chi(R) \chi_p(R). \quad (3.9)$$

Using equation 3.9 and table 3.1 we can reduce this reducible representation $|n\rangle$ in terms of irreducible representations. Thus our representation reduces as

$$|n\rangle = A_g + E_{2g} + B_u + E_{1u}. \quad (3.10)$$

We can thus define our basis in a symmetric way as defined by the irreducible representation, by using Symmetry Adapted Linear Combinations (SALCs) and a projection operator,

$$[P^p]_{\mathbf{x}} = \left[\sum_R \{ \chi_p(R) \cdot R \} \right]_{\mathbf{x}}. \quad (3.11)$$

Using equation 3.11 our basis vectors transform as shown in table 3.2. Using tables 3.3 and

Table 3.3 The character table for the irreducible representation, where $\varepsilon = \exp(i\pi/3)$.

	E	C_6	C_3	C_2	C_3^2	C_6^5	i	S_3^5	S_6^5	σ_h	S_6	S_3
A_g	1	1	1	1	1	1	1	1	1	1	1	1
E_{2g}	1	$-\varepsilon^*$	$-\varepsilon$	1	$-\varepsilon^*$	$-\varepsilon$	1	$-\varepsilon^*$	$-\varepsilon$	1	$-\varepsilon^*$	ε
	1	$-\varepsilon$	$-\varepsilon^*$	1	$-\varepsilon$	$-\varepsilon^*$	1	$-\varepsilon$	$-\varepsilon^*$	1	$-\varepsilon$	$-\varepsilon^*$
B_u	1	-1	1	-1	1	-1	-1	1	-1	1	-1	1
E_{1u}	1	ε	$-\varepsilon^*$	-1	$-\varepsilon$	ε^*	-1	$-\varepsilon$	ε^*	1	ε	$-\varepsilon^*$
	1	ε^*	$-\varepsilon$	-1	$-\varepsilon^*$	ε	-1	$-\varepsilon^*$	ε	1	ε^*	$-\varepsilon$

3.2 we can write our irreducible representations in terms of our SALCs.

$$\begin{aligned}
A_g &= (|n_1\rangle \times 1) + (|n_2\rangle \times 1) + (|n_3\rangle \times 1) + (|n_4\rangle \times 1) + (|n_5\rangle \times 1) + (|n_6\rangle \times 1) \\
&\quad + (|n_4\rangle \times 1) + (|n_5\rangle \times 1) + (|n_6\rangle \times 1) + (|n_1\rangle \times 1) + (|n_2\rangle \times 1) + (|n_3\rangle \times 1) \\
&= 2|n_1\rangle + 2|n_2\rangle + 2|n_3\rangle + 2|n_4\rangle + 2|n_5\rangle + 2|n_6\rangle \quad \text{monopolar} \quad (3.12)
\end{aligned}$$

$$\begin{aligned}
E_{2g} &= (|n_1\rangle \times 1) + (|n_2\rangle \times -\varepsilon^*) + (|n_3\rangle \times -\varepsilon) + (|n_4\rangle \times 1) + (|n_5\rangle \times -\varepsilon^*) + (|n_6\rangle \times -\varepsilon) \\
&\quad + (|n_4\rangle \times 1) + (|n_5\rangle \times -\varepsilon^*) + (|n_6\rangle \times -\varepsilon) + (|n_1\rangle \times 1) + (|n_2\rangle \times -\varepsilon^*) + (|n_3\rangle \times -\varepsilon) \\
&= 2|n_1\rangle - 2\varepsilon^*|n_2\rangle - 2\varepsilon^*|n_3\rangle + 2|n_4\rangle - 2\varepsilon^*|n_5\rangle - 2\varepsilon|n_6\rangle \quad \text{quadrupolar} \quad (3.13)
\end{aligned}$$

$$\begin{aligned}
E_{2g} &= (|n_1\rangle \times 1) + (|n_2\rangle \times -\varepsilon) + (|n_3\rangle \times -\varepsilon^*) + (|n_4\rangle \times 1) + (|n_5\rangle \times -\varepsilon) + (|n_6\rangle \times -\varepsilon^*) \\
&\quad + (|n_4\rangle \times 1) + (|n_5\rangle \times -\varepsilon) + (|n_6\rangle \times -\varepsilon^*) + (|n_1\rangle \times 1) + (|n_2\rangle \times -\varepsilon) + (|n_3\rangle \times -\varepsilon^*) \\
&= 2|n_1\rangle - 2\varepsilon|n_2\rangle - 2\varepsilon^*|n_3\rangle + 2|n_4\rangle - 2\varepsilon|n_5\rangle - 2\varepsilon^*|n_6\rangle \quad \text{quadrupolar} \quad (3.14)
\end{aligned}$$

$$\begin{aligned}
B_u &= (|n_1\rangle \times 1) + (|n_2\rangle \times -1) + (|n_3\rangle \times 1) + (|n_4\rangle \times -1) + (|n_5\rangle \times 1) + (|n_6\rangle \times -1) \\
&\quad + (|n_4\rangle \times -1) + (|n_5\rangle \times 1) + (|n_6\rangle \times -1) + (|n_1\rangle \times 1) + (|n_2\rangle \times -1) + (|n_3\rangle \times 1) \\
&= 2|n_1\rangle - 2\varepsilon|n_2\rangle + 2|n_3\rangle - 2|n_4\rangle + 2|n_5\rangle - 2|n_6\rangle \quad \text{hexapolar} \quad (3.15)
\end{aligned}$$

$$\begin{aligned}
E_{1u} &= (|n_1\rangle \times 1) + (|n_2\rangle \times \varepsilon) + (|n_3\rangle \times -\varepsilon^*) + (|n_4\rangle \times -1) + (|n_5\rangle \times -\varepsilon) + (|n_6\rangle \times \varepsilon^*) \\
&\quad + (|n_4\rangle \times -1) + (|n_5\rangle \times -\varepsilon) + (|n_6\rangle \times \varepsilon^*) + (|n_1\rangle \times 1) + (|n_2\rangle \times \varepsilon) + (|n_3\rangle \times -\varepsilon^*) \\
&= 2|n_1\rangle + 2\varepsilon|n_2\rangle - 2\varepsilon^*|n_3\rangle - 2|n_4\rangle - 2\varepsilon|n_5\rangle + 2\varepsilon^*|n_6\rangle \quad \text{dipolar} \quad (3.16)
\end{aligned}$$

$$\begin{aligned}
E_{1u} &= (|n_1\rangle \times 1) + (|n_2\rangle \times \varepsilon^*) + (|n_3\rangle \times -\varepsilon) + (|n_4\rangle \times -1) + (|n_5\rangle \times -\varepsilon^*) + (|n_6\rangle \times \varepsilon) \\
&\quad + (|n_4\rangle \times -1) + (|n_5\rangle \times -\varepsilon^*) + (|n_6\rangle \times \varepsilon) + (|n_1\rangle \times 1) + (|n_2\rangle \times \varepsilon^*) + (|n_3\rangle \times -\varepsilon) \\
&= 2|n_1\rangle + 2\varepsilon^*|n_2\rangle - 2\varepsilon|n_3\rangle - 2|n_4\rangle - 2\varepsilon^*|n_5\rangle + 2\varepsilon|n_6\rangle \quad \text{dipolar} \quad (3.17)
\end{aligned}$$

Figure 3.3 shows the sign of each of the arms as found in the solutions above. We see first

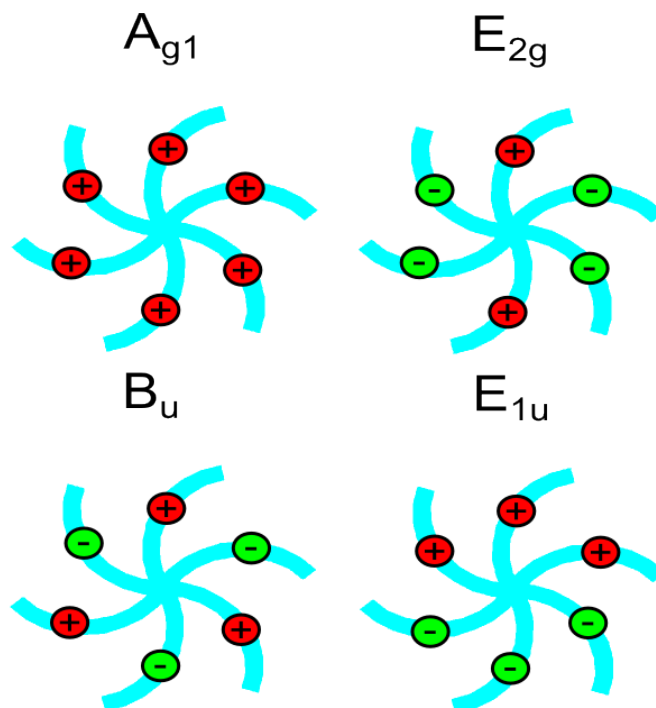


Fig. 3.3 The symmetry allowed modes of the positive ideal structure as calculated from the point group of the structure. Group theory arguments allowed the modes to be determined in terms of an irreducible representation.

all $|n\rangle$ have a positive sign for the irreducible representation A_{g1} , this has the appearance of a monopolar type mode. Next, only two of the arms have a positive sign with the other four having a negative sign, which appears as a quadrupolar type mode. There is also a second quadrupolar type mode, but only differs from the first in the imaginary part due to the ϵ and ϵ^* terms. The next mode displays a hexapolar type intensity due to having opposite signs on neighboring arms. The last modes which come from the symmetry analysis are dipolar like modes, with two modes coming from the analysis, again only different in their imaginary components. Finding these modes involved using a basis which was chosen as a localized state on each of the arms. Due to this choice nodes or peaks along the arms will not appear in the analysis, which would require a basis which described the arms broken down into a smaller basis set. The next sections will detail the simulations of our nanoparticles.

3.5 Eigenmode Analysis

3.5.1 Eigenmodes of an Ideal Positive Plasmonic Nanoparticle

When an electron beam, such as in a transmission electron microscope, interacts with a metallic nanoparticle the time-dependent field of the electron can be considered to be an external perturbation to the electronic states of the nanoparticle. If we consider our nanoparticle to have dielectric function ϵ_1 and assume it is embedded in a local environment

with dielectric function ε_2 we can calculate the induced electromagnetic field due to the interaction of field of the electron and the nanoparticle [103]. Starting with Poisson's equation for the electrostatic potential,

$$\nabla[\varepsilon(r, \omega)\nabla\phi(r, \omega)] = -4\pi\rho^{ext}(r, \omega) \quad (3.18)$$

where ρ^{ext} is the charge density for the external electron and,

$$\varepsilon(r, \omega) = \begin{cases} \varepsilon_1 & \text{inside the nanoparticle} \\ \varepsilon_2 & \text{outside the nanoparticle.} \end{cases}$$

The electrostatic potential, ϕ can be written in terms of a charge distribution σ located at a boundary $\delta\Omega$, using the free-space Green function [104],

$$G(r, r') = \frac{1}{4\pi|r - r'|},$$

which gives

$$\phi = \frac{1}{\varepsilon_0} \int_{\delta\Omega} \overbrace{G(r, r')\sigma da'}^{\text{induced}} + \overbrace{\phi_{ext}}^{\text{external}}. \quad (3.19)$$

If we introduce a surface derivative F of G, we get

$$\lambda\phi - \int_{\delta\Omega} F(s, s')\sigma da' = \varepsilon_0 \frac{\delta\phi_{ext}}{\delta\hat{n}} \quad (3.20)$$

where,

$$\lambda = \frac{\varepsilon_2 + \varepsilon_1}{\varepsilon_2 - \varepsilon_1}.$$

This equation can be solved by for eigenvalues λ_k , and surface charge eigenvectors, σ_k . Thus for a known shape of nanoparticle with known dielectric constant in a known dielectric environment one can calculate the surface charge modes from this equation. Using the MNPBEM MatLab toolkit this eigenmode analysis was carried out for each of the shapes of the nanoparticles shown in Figure 3.1, both the experimental and devised structures. The results for the structure in Figure 3.1a are shown in Figure 3.4.

The first eigenmode Figure 3.4a and its associated surface charge distribution has a monopolar intensity, which agrees well with the prediction from the symmetry analysis in Section 3.4 and corresponds to the mode for the A_g irreducible representation and has an eigenvalue of $\lambda = -6.2832$. Though this mode is the first to appear in both the symmetry analysis and the eigenmode analysis, such a mode is not physically realistic, as it is a monopole, so would not appear in experiments. A lower eigenvalue corresponds to a lower energy thus a higher likelihood of being observed in EELS data, as there is an exponential intensity fall off as loss energy increases. The absolute value of the eigenvalue is not important but the relative values indicate the relative energies of each mode, with increasing energy corresponding to increasing lambda. The second eigenmode Figure 3.4b has a hexapolar

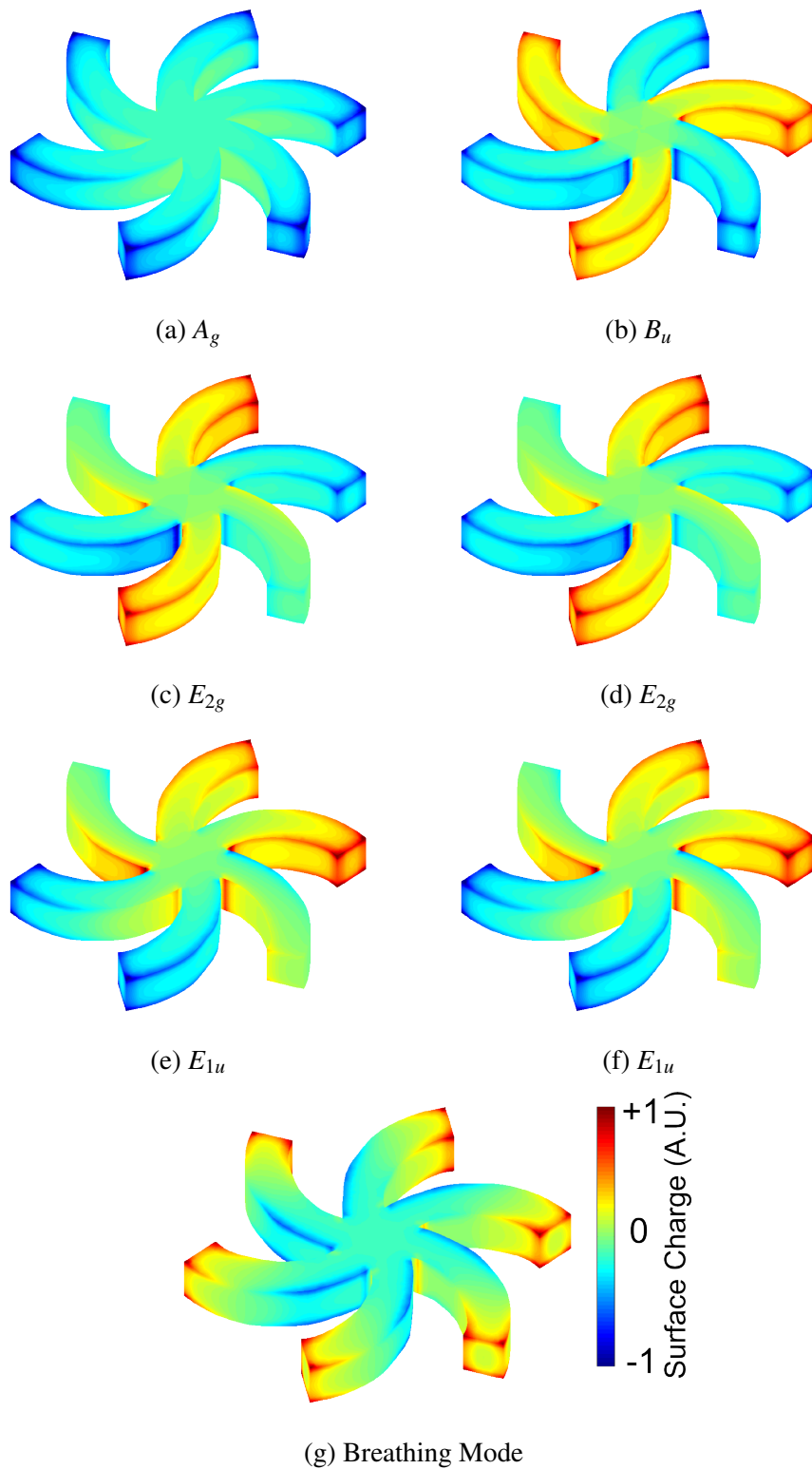


Fig. 3.4 The surface charge eigenvectors, σ_k , of the ideal positive plasmonic structure from Figure 3.1a. The colourmap represents the intensity of the surface charge, calculated using Eqn 3.20. Only the real part is shown. (c) and (d) have similar real component however they would differ in imaginary component, as shown in the equations in section 3.4. Similarly with (e) and (f).

intensity and agrees with the B_u mode found from the symmetry analysis, and it has a purely real eigenvalue of $\lambda = 6.0411$. The second two eigenmodes Figures 3.4c and 3.4d have quadrupolar like intensity features and the same real part of either eigenvalue $\lambda = -6.0205$ however their (small) imaginary part of the eigenvalues differ in sign, again as predicted by the symmetry analysis displaying the characteristics of the irreducible representations E_{2g} . The fourth and fifth eigenmodes Figures 3.4e and 3.4f display a dipolar intensity pattern and again differ in eigenvalue only in the sign of the imaginary part. The final eigenmode Figure 3.4g displays something not predicted by the symmetry analysis, which is a higher order breathing mode. This was not predicted as it displays a change in intensity along the arms and given our basis was chosen as a localised state on each arm, which is indivisible this mode was not predicted. These eigenmodes confirm what was predicted in the symmetry analysis, but more importantly the eigenvalues tell us about what would be seen experimentally.

3.5.2 Eigenmodes of an Experimentally Realistic Positive Plasmonic Nanoparticle

When considering the experimentally realistic positive nanoparticle, shown in Figure 3.1b, we know from symmetry analysis that the lack of symmetry leads to no modes as there would only be the identity element. However as can be seen in Figure 3.5 this is not the case. Following the same eigenmode analysis for the previous nanoparticle, Figure 3.5a shows a first eigenmode again with a monopolar intensity but in this case the spatial distribution is inhomogeneous. This is true both around the base and tips of the arms, and between the different arms themselves. This hints towards differences between ideal and actual structures due to the structural differences and inconsistencies in thickness along the arms. The second eigenmode, Figure 3.5b shows again a hexapolar mode, as was seen in the ideal particle, again this mode lacks the symmetry of the ideal nanoparticle. This mode has characteristics similar to the symmetric modes, from this we can see that the higher-order symmetry description is useful because the observed real modes tend to preserve some of the characteristics of the predicted ideal modes. Figures 3.5c and 3.5d show again two quadrupolar modes, however these two modes have a different real part of their eigenvalues, $\lambda = -6.1159$ and $\lambda = -6.0772$ respectively. This splitting of the modes would result in the two modes appearing at different loss energies, if this difference is within the resolution of the probing method. Figures 3.5e and 3.5f show again two dipolar modes, however these two modes again have a different real part of their eigenvalues, $\lambda = -6.0355$ and $\lambda = -5.9951$ respectively. The last mode in Figure 3.5g is again a higher order breathing mode. There are a few important conclusions that can be made from this analysis. The ordering of the eigenmodes (here organised in increasing eigenvalue) shows you the likely modes which will be seen experimentally. As stated previously, the lambda values tells you the relative energy of the modes, thus ordering in this way highlights the low energy modes. Figure 3.6 shows both the ideal (red) and experimentally realistic (blue) eigenvalues. It can be

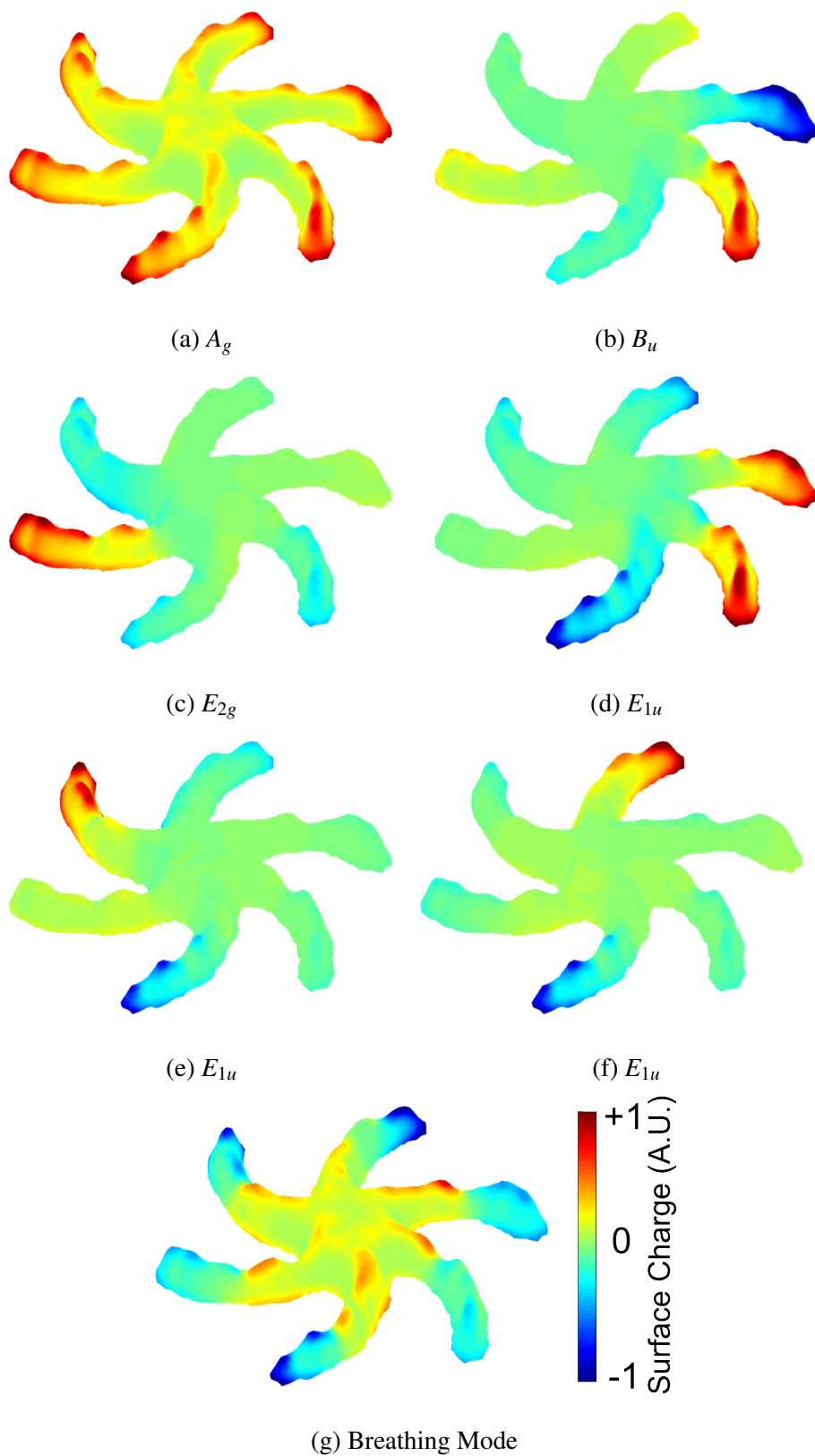


Fig. 3.5 The surface charge eigenvectors, σ_k , of the experimental positive plasmonic structure from Figure 3.1b. The colourmap represents the intensity of the surface charge, calculated using Eqn 3.20.

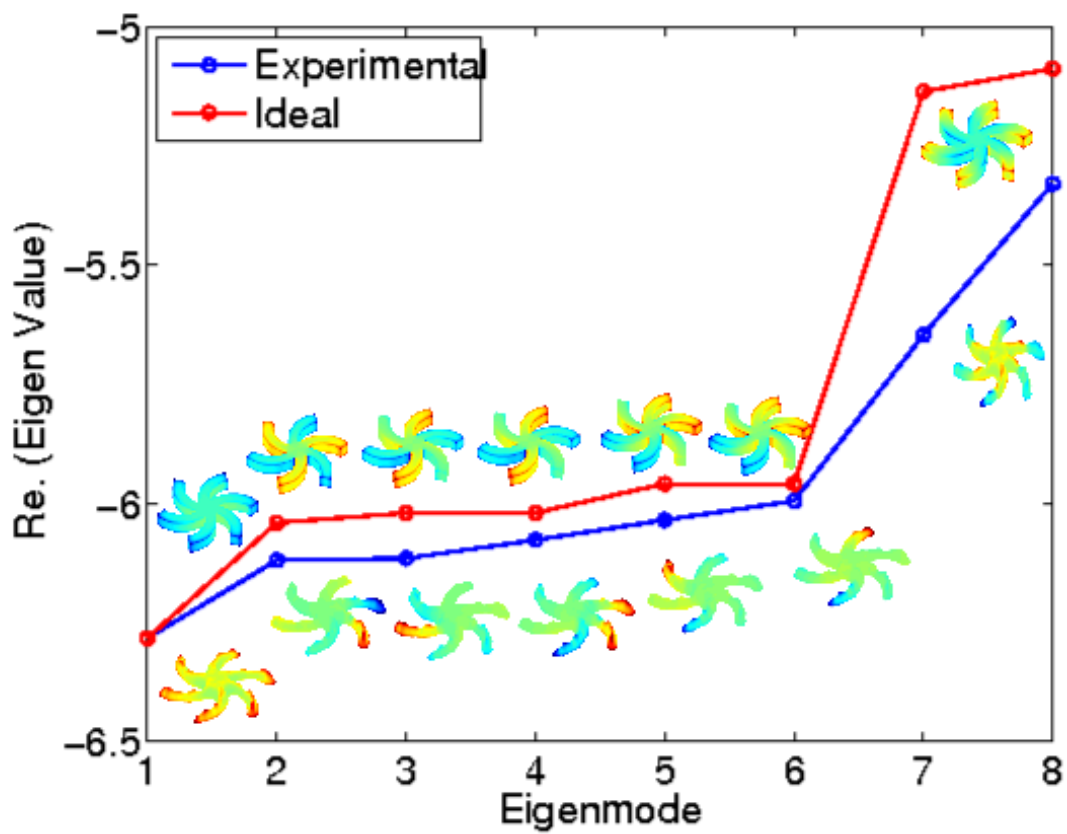


Fig. 3.6 Comparison between the ideal (red) and experimentally realistic (blue) eigenvalues. We see a grouping of the eigenmodes in clusters of similar eigenvalues. We can also see a shift in eigenvalue between the ideal and actual eigenvalues, suggesting a shift in energy.

Table 3.4 The calculated dipole moment for the eigenmodes of the ideal and actual nanoparticle.

Eigenvalue	Ideal	Experiment
1	2.532e-19	2.635e-19
2	5.243e-32	8.109e-20
3	7.020e-32	2.394e-20
4	7.020e-32	3.989e-20
5	5.370e-19	5.794e-19
6	5.370e-19	5.728e-19
7	4.461e-33	3.092e-21
8	5.283e-33	9.870e-22
	dark	bright

seen from the first few points along both curves the proximity of the hexapolar, quadrupolar and dipolar modes. The closeness in eigenvalue will mean these modes will likely overlap in energy. It can also be seen that the experimentally realistic modes appear at a lower eigenvalue, thus will appear at a lower energy. It is also interesting to note the grouping of the eigenvalues, for both nanoparticles they appear in clusters of similar eigenvalue. This clustering comes directly from the symmetry analysis which was discussed in Section 3.4. Table 3.4 shows a comparison of the calculated dipole moment for the eigenmodes shown in Figure 3.6. For the second eigenmode, which has a hexapolar appearance, for the experimentally realistic nanoparticle we see an increase in the dipole moment, when compared to the ideal nanoparticle. This suggests a change in brightness of the mode, a transition from dark to bright. It was discussed in Section 2.4 that the dipole moment of a mode would distinguish whether or not it would couple with light, which determines the brightness of the mode. The change from a dark to bright mode can be highlighted by the similarity in magnitude of dipole moment of this mode when compared to the bright dipolar mode. This is one of the main results of this work, showing that although a deviation in symmetry has not resulted in a stark change in the occurrence or ordering of the modes, it has resulted in a shift in energy and a change from dark to bright modes for hexapolar and quadrupolar modes for the experimentally realistic nanoparticle. Thus these modes would couple to light in the experimental nanoparticle.

3.5.3 Eigenmodes of a Devised Positive Plasmonic Nanoparticle

The next particle considered in this work is the devised positive particle, Figure 3.1d. Again as this is not an ideal shape we know from symmetry analysis that the lack of symmetry leads to no modes. However as can be seen in Figure 3.7 this is again not the case. Following the same eigenmode analysis for the experimentally realistic nanoparticle shows a first eigenmode Figure 3.7a again showing a monopolar intensity but in this case the spatial distribution is inhomogeneous, unlike what was seen in the ideal nanoparticle. It should be

noted that the sign of the monopole is not important. The second eigenmode, Figure 3.7b shows again a hexapolar mode, as was seen in the ideal particle, and again this mode lacks the symmetry of the ideal nanoparticle. Figures 3.7c and 3.7d show again two quadrupolar modes, however these two modes have a different real part of their eigenvalues, $\lambda = -5.8894$ and $\lambda = -5.8730$ respectively. This splitting of the modes would result in the two modes appearing at different loss energies, if this difference is within the resolution of the probing method. Figures 3.7e and 3.7f show again two dipolar modes, however these again have a different real part of either eigenvalues, $\lambda = -5.8346$ and $\lambda = -5.8270$ respectively. The final mode Figure 3.7g is again a higher order breathing mode.

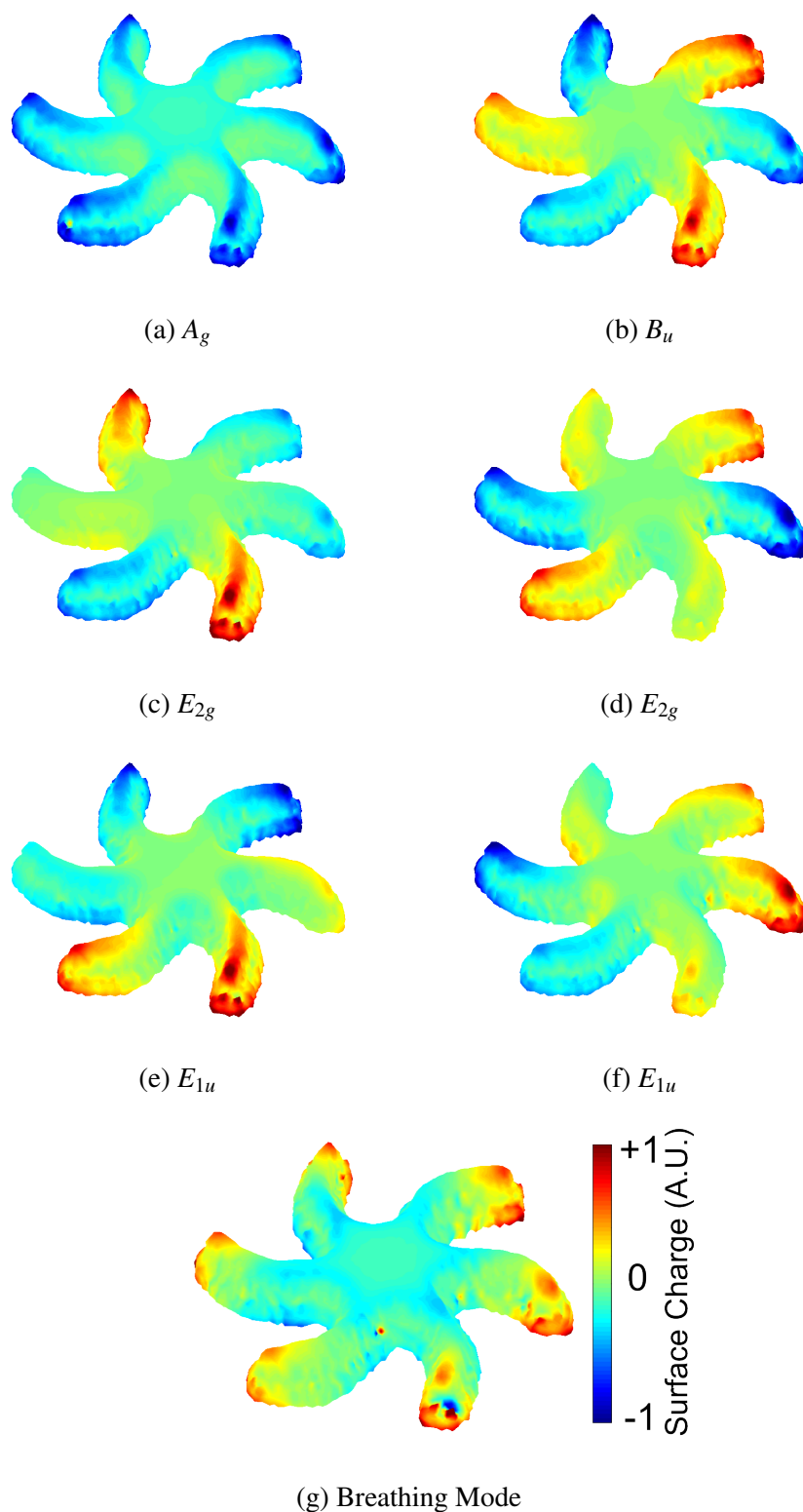


Fig. 3.7 The surface charge eigenvectors, σ_k , of the devised positive plasmonic structure from Figure 3.1d. The colourmap represents the intensity of the surface charge, calculated using Eqn 3.20.

3.5.4 Eigenmodes of an Experimental Realistic Negative Plasmonic Particle

As was done in the previous sections, the MNPBEM toolbox [24] will be used to calculate the bound modes of the nanoparticle using approximations of Maxwell's equations. Figure 3.8 shows the results of the eigenmode analysis for the negative particle shown in Figure 3.1c. The first eigenmode Figure 3.8a shows a monopolar intensity as was seen for all previous examples. The second eigenmode Figure 3.8b and third, Figure 3.8c, eigenmode show dipolar like modes, which is in contrast to the hexapolar mode observed for the complementary positive nanoparticle in the previous section. The fourth and fifth modes Figure 3.8d and Figure 3.8e show quadrupolar like intensities. When examining the character table it can be seen that the first two modes belong to the representation E_1 . This can be confirmed by performing a C_2 rotation on the mode and observing the sign change. By similar arguments the next mode belongs to the E_2 irreducible representation, as there is no sign change on rotation. The final two modes, Figure 3.8f and Figure 3.8g, show hexapolar modes, which belong to the irreducible representation B . By continuing this trend the modes of the particle can be broken down into their irreducible representations and weights,

$$\lambda = A + 2B + 2E_1 + E_2 \quad (3.21)$$

with higher order modes being described by reducible representations which can be factorised into the irreducible representations. A similar grouping of the eigenmodes can be seen when comparing the eigenvalues, λ . The second and third modes have eigenvalues of $\lambda = -6.1254$ and $\lambda = -6.1251$ respectively. The next two have eigenvalues, $\lambda = -5.9987$ and $\lambda = -5.9981$. The final two have eigenvalues, $\lambda = -5.8845$ and $\lambda = -5.8842$. Thus one could arrange the eigenmodes in order and group them together using either the irreducible representations to which they belong or the eigenvalues group by proximity and the results would be the same. When comparing the eigenmodes obtained here with the complementary positive particle in the previous section the first is that the ordering of the modes has changed. The positive particle began with hexapolar, followed by quadrupolar then dipolar modes. In the negative particle, the hexapolar mode has moved to a higher eigenvalue, which means it will be appear at a higher energy in the spectra and thus will be less likely to be present in our experimental data. This is one of the features of Babinet's principle where quadrupolar modes become more dominant in hole structures. Figure 3.9 shows a comparison between the nanoparticles in this and the previous section. We see that although there is a similar grouping of the modes into their irreducible representations the energies (i.e the eigenvalues) do not align.

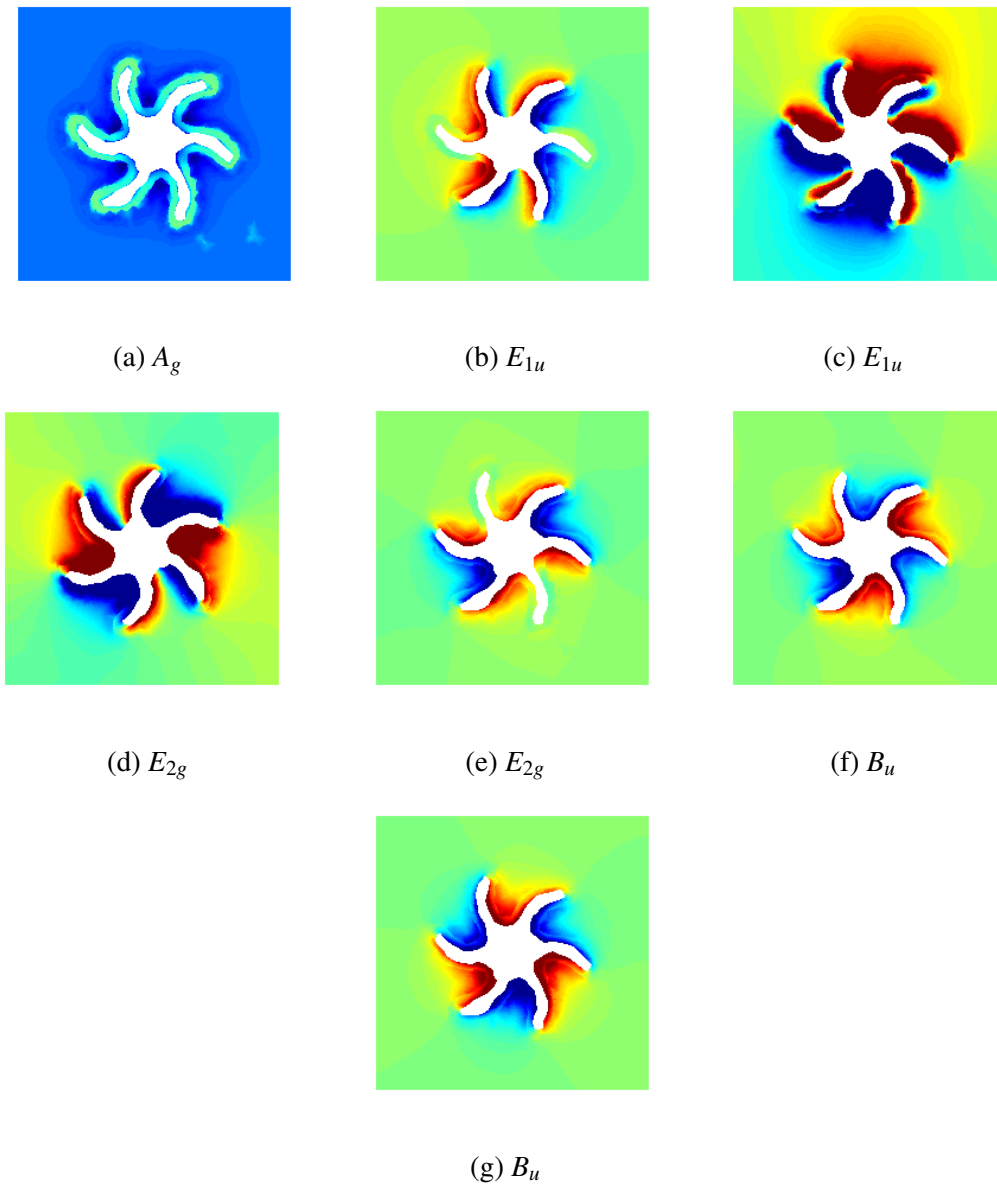


Fig. 3.8 The surface charge eigenvectors, σ_k , of the negative plasmonic structure from Figure 3.1c. The colourmap represents the intensity of the surface charge, calculated using Eqn 1.3 from the previous chapter. The modes are ordered in order of increasing eigenvalue.

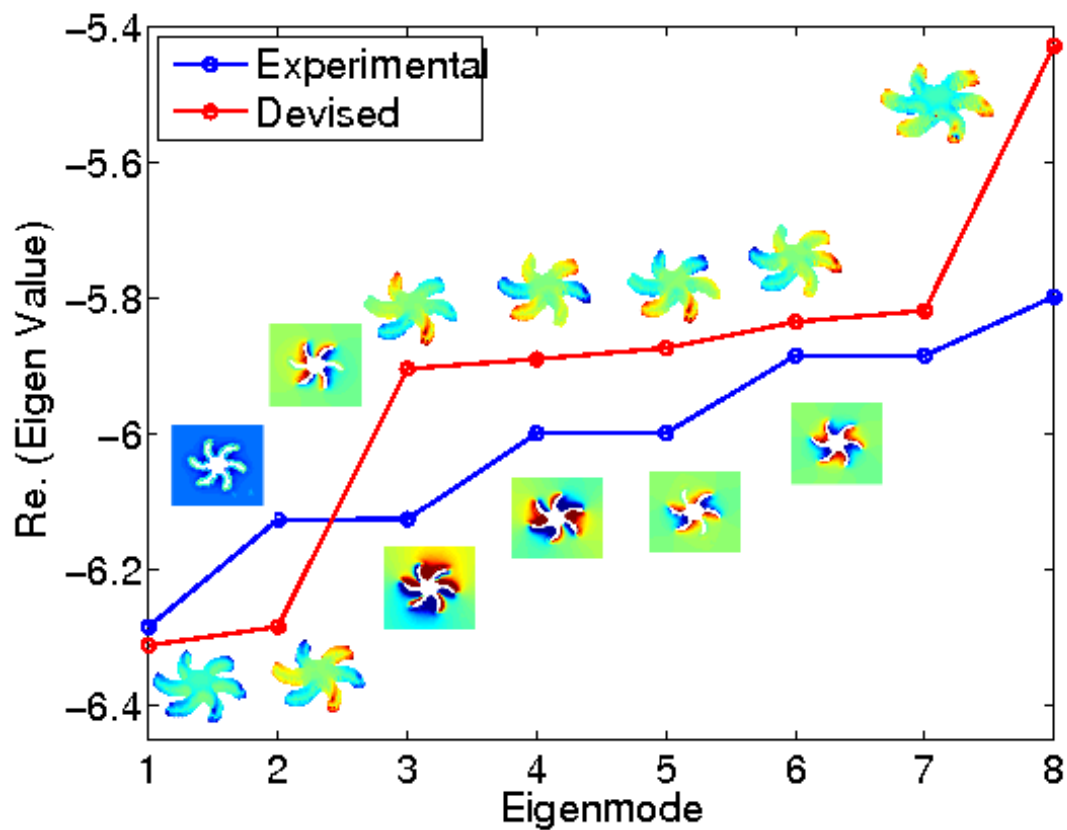


Fig. 3.9 Comparison between the devised positive and experimentally realistic negative nanoparticle's eigenvalues. We see a grouping of the eigenmodes in clusters of similar eigenvalues. We can also see a shift in eigenvalue between the two nanoparticle's eigenvalues, suggesting a shift in energy.

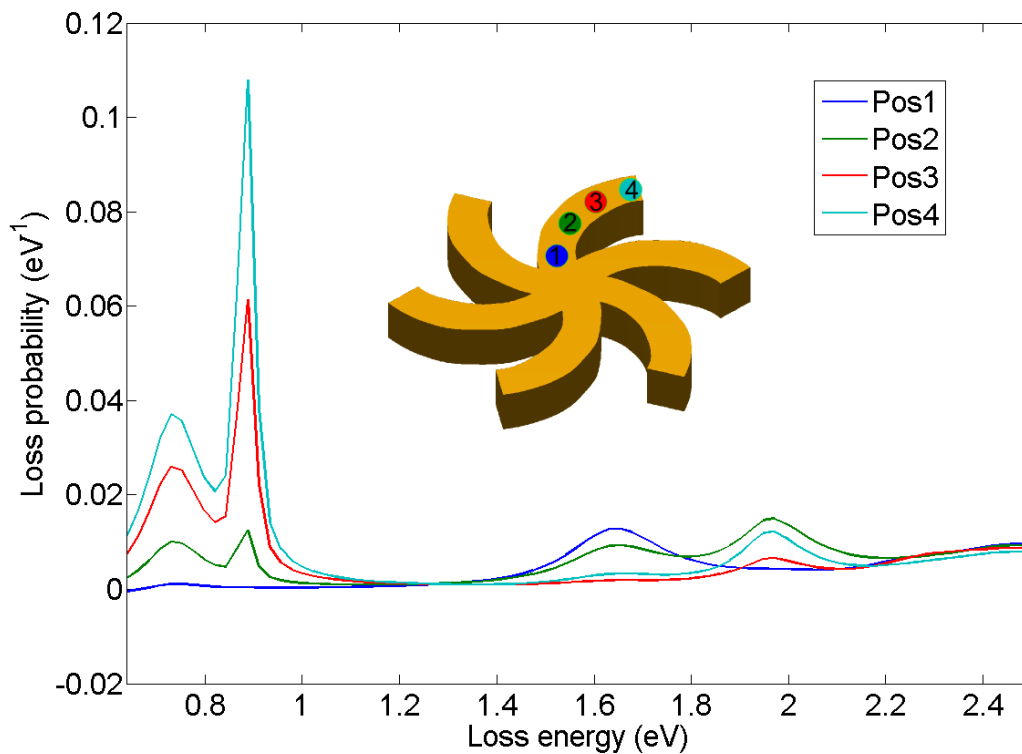


Fig. 3.10 Inset: The impact positions for the electron beam, chosen on the ideal particle from Figure 3.1a. Graph: EELS spectrum for the ideal particle the beam positions indicated with circles in the top panel. In the simulations we assume a kinetic electron energy of 200 keV.

3.6 Electron Energy Loss Maps of the Nanoparticles

3.6.1 EELS Maps of an Ideal Positive Plasmonic Nanoparticle

Using the MNPBEM toolbox the EELS loss maps from the particles shown in Figure 3.1 were calculated. This involves a full solution of Maxwell's equations at the boundaries of a mesh, as discussed in Section 1.3.3. The eigenmode analysis in Section 3.5 shows that even in the ideal structure not all parts of the structures arms are excited in each mode. This shows the need for STEM when probing the plasmonic nature of nanoparticles, as our electron beam must interact with different areas of particle in order to compose a full picture of the plasmonic excitation. This is also something that must be present in our EELS simulations. When setting up an excitation in the MNPBEM toolbox one must first select impact points, where the beam is positioned and where a loss map will be calculated. The inset in Figure 3.10 shows the four positions chosen on the ideal particle to calculate a loss spectra from. The graph in Figure 3.10 shows the loss maps calculated at each of these four positions on the ideal particle. The peaks in the graph shows the plasmonic modes which are being excited by the incident electron. It's clear from the graph that not all modes are excited at all positions, which we would expect from the eigenmode analysis. The first peak in the graph is at 0.73eV and is most intense at positions further along the arm, as you move away from the centre,

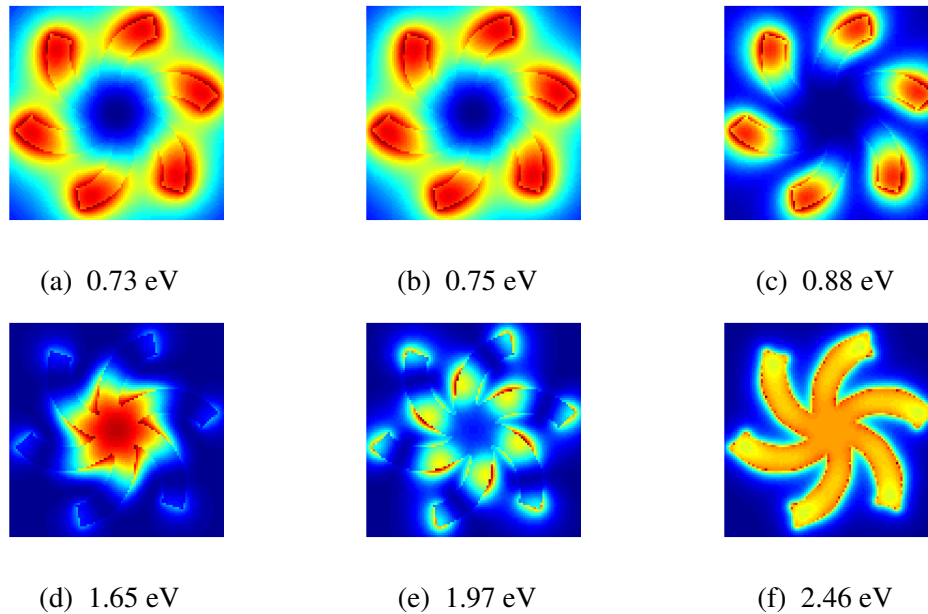


Fig. 3.11 Spatial EELS maps corresponding to the peaks in Figure 3.10 for the ideal particle in Figure 3.1a. The modes (a) and (b) appear to be a single broader mode, as the spatial intensity only slightly changes radially outward from the central region.

this suggests a mode concentrated along the tips. This peak, although the lowest in energy is not the most intense. The second peak in the graph is at 0.88eV and is again most intense at the tips of the arms. The third peak at 1.65eV is intense only around the central region, and slightly the tips. The fourth peak has varying intensity at each point along the arm, suggesting more than one node along the arms. The final peak at the end of the data set appears to show the beginning of the bulk plasmon where all parts are being excited. Once the energies of modes of interest have been found, spatial loss maps can be calculated showing the spatial position where electrons lost the given energy. Figure 3.11 shows the spatial loss maps corresponding to the peaks in Figure 3.10. Figure 3.11a shows the loss map for the first peak, at 0.73eV in Figure 3.10 which confirms that the area being excited in the particle is around the tips. However it is also found that this peak is made up of two closely aligned peaks, with another at 0.75eV . These peaks are very similar and only differ in increased intensity moving radially outward from the centre. These two peaks show an interesting feature of the SPs, shown by the intensity seen between the tips of the arms. This is a coupling effect, similar to the coupled spheres seen in Section 2.3 and explains why this feature, although appearing at the lowest loss energy is not the most intense feature. The next loss map, at 0.88eV is the most intense feature and appears only along the arms and at the tips. This is likely to be a hybridization between the three distinct modes seen in the eigenmode analysis, which when overlapped will appear as all arms having equal intensity and spatial distribution. The next two modes at 1.65eV and 1.97eV are the first which appear with nodes along the arms, the first appearing intense around the base, then dipping to a minimum before peaking at the tips in the first mode, whereas the second has two nodes along the arms. These

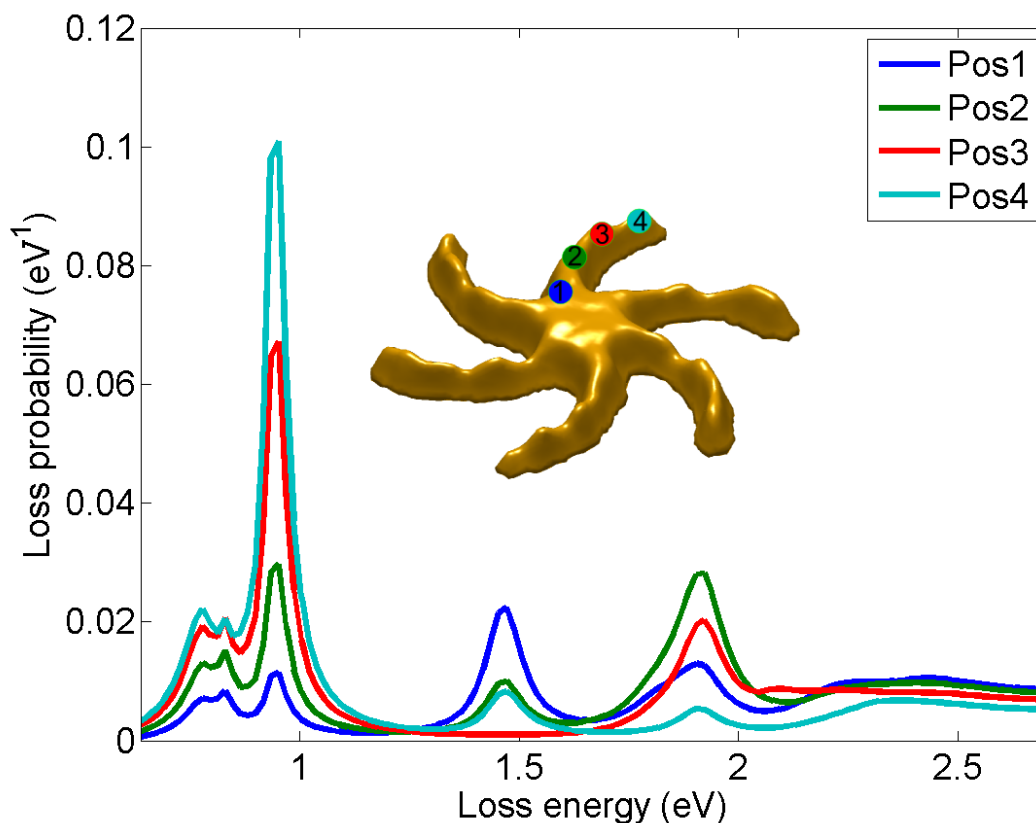


Fig. 3.12 Inset: The impact positions for the electron beam, chosen on the experimental particle from Figure 3.1b. Graph: EELS spectrum for the experimental particle obtained at the beam positions indicated with circles in the top panel. In the simulations we assume a kinetic electron energy of 200 keV.

breathing modes were not predicted by the symmetry analysis, and appear at higher loss energies, decreasing their likelihood of appearing in experimental data. The final loss map is the appearance of the bulk plasmon, where each arm appears equally intense.

3.6.2 EELS Maps of an Actual Positive Plasmonic Nanoparticle

Using the MNPBEM toolbox the EELS loss maps from the particle shown in Figure 3.1b were also calculated. The inset in Figure 3.12 shows the four positions chosen on the experimental particle to calculate a loss spectra from. These positions were chosen by selecting intense regions in the eigenmode analysis as before.

The plots in Figure 3.12 show the loss maps calculated at each of these four positions on the experimental particle. Figure 3.13a shows the loss map for the first peak, at 0.77eV in Figure 3.12, which confirms that the area being excited in the particle is around the tips, but also appears to couple between the arms, the same as was seen in the ideal loss maps. However one important note about this mode is that the intensity does not appear homogeneous. It can be seen by the higher intensity around only a few of the tips that

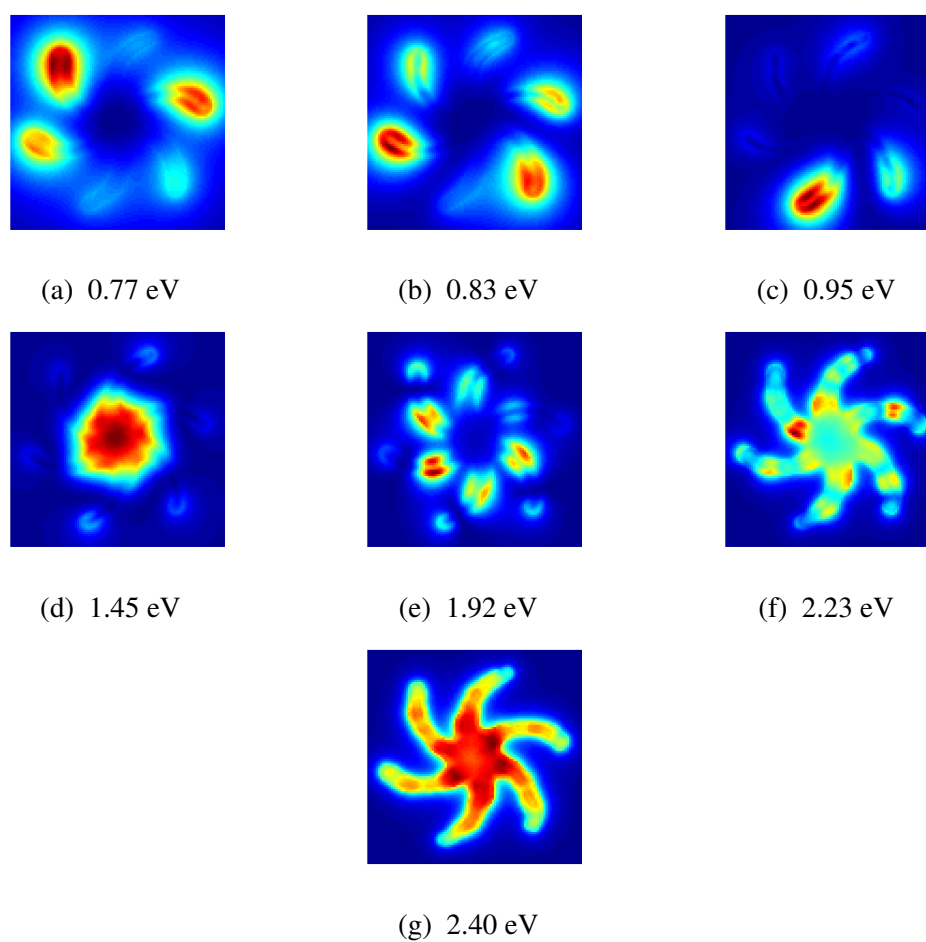


Fig. 3.13 Spatial EELS maps corresponding to the peaks in Figure 3.12 for the experimental particle in Figure 3.1b.

this mode is a result of mode splitting, with the three modes 0.77eV , 0.83eV and 0.95eV appearing to be a single mode which has split in energy. The next mode observed Figure 3.13d observed at 1.45eV has a similar intensity distribution as the mode at 1.65eV in the ideal nanoparticle. Similarly the next two modes observed Figure 3.13e and Figure 3.13g observed at 1.92eV and 2.40eV have a similar intensity distribution as the modes at 1.97eV and 2.46eV in the ideal nanoparticle.

3.6.3 EELS Maps of a Devised Positive Plasmonic Nanoparticle

Using the MNPBEM toolbox the EELS loss maps from the particle shown in Figure 3.1d were also calculated. The inset in Figure 3.14 shows the four positions chosen on the devised particle to calculate a loss spectra from. These positions were chosen by selecting intense regions in the eigenmode analysis as before. The plot in Figure 3.14 shows the loss maps

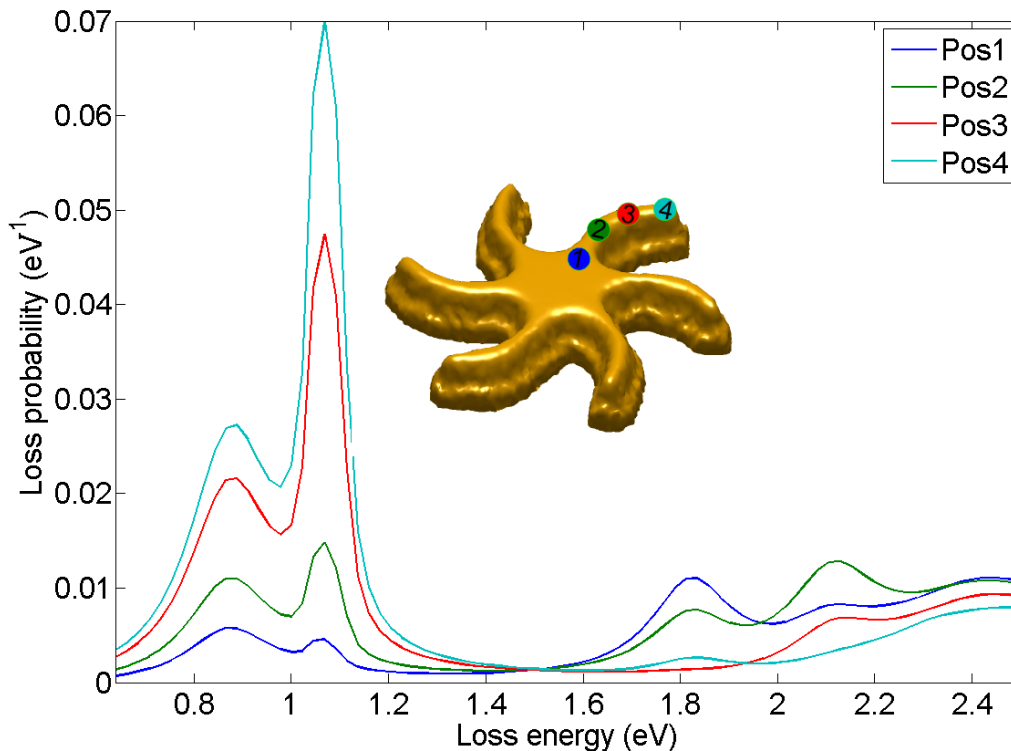


Fig. 3.14 Top: The impact positions for the electron beam, chosen on the devised particle from Figure 3.1d. Bottom: The loss maps corresponding to each impact parameter.

calculated at each of these four positions on the devised particle. The first difference which is apparent when comparing Figures 3.10 and 3.14 is that the first few peaks appear at a lower energy in the ideal structure than in the devised structure, which was expected from the increase in eigenvalues seen in Figure 3.6. Again we see that the first peak at 0.86eV in the actual structure is not the most intense; instead the second peak at 1.06eV appears most intense. The first peak appears most intense at positions away from the central region, in

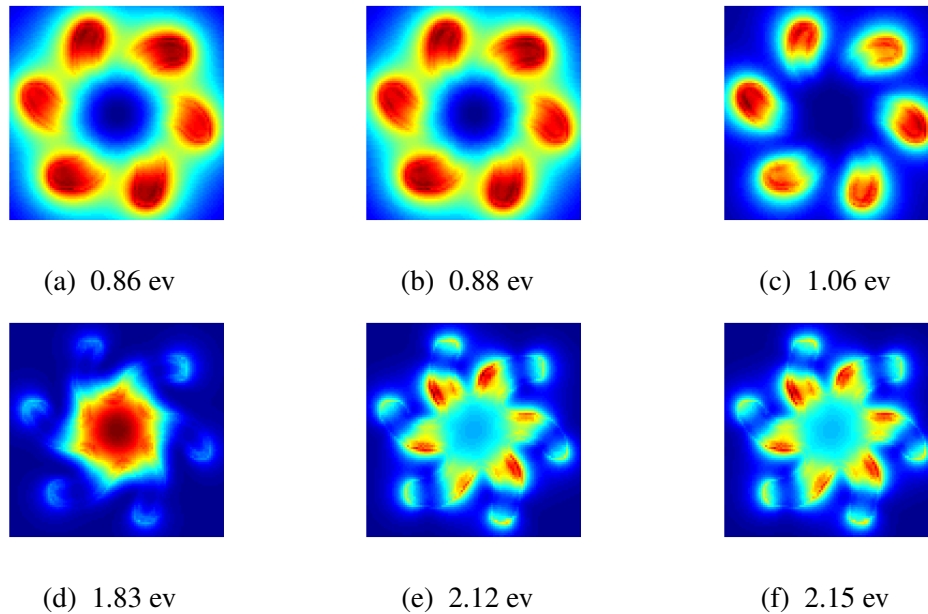


Fig. 3.15 Spatial EELS maps corresponding to the peaks in Figure 3.14 for the actual particle in Figure 3.1d.

the arms, as does the second peak suggesting they are similar. Again, the next two peaks appear to show intensity differences which go up and down suggesting nodes along the arms with the final peak starting to appear at the end of the data set likely being the bulk plasmon. Figure 3.15 shows the spatial loss maps corresponding to the peaks in Figure 3.14. Figure 3.15a shows the loss map for the first peak, at 0.86eV in Figure 3.14 which confirms that the area being excited in the particle is around the tips, but also appears to couple between the arms. The same as was seen in the ideal loss maps. In this nanoparticle mode intensity does appear more homogeneous around the arms, however it is not as symmetric as the ideal. This is due to the thickness of the arms being wider. It can be seen by the darker color around a few of the tips that this mode is a result of mode splitting, with the two modes 0.86eV and 0.88eV being more intense around tips which are less intense in the mode 1.06eV . Such a difference would give rise to a different electric field as will be discussed in a later section. The mode at 1.06eV is markedly similar to that seen in the ideal structure but with a shift in energy of around 1.2eV , a similar energy shift as each of the other modes. The mode at 1.83eV again shows the first nodes along the arms, but again the intensity at the tips of the arms is affected by the surface roughness and leads to an inhomogeneous intensity distribution. The last two modes arise from the splitting of a single mode of the parent structure. One can conclude from these results that local surface roughness has a large impact on the spatial distribution and intensity of the plasmon modes. It would appear the nanoparticle in this section which has less roughness than the positive nanoparticle in the previous section, has less splitting of modes and is closer to the ideal shape. This can also be explained by the larger central region and thicker arms, which mean local roughness has less of an impact on the global shape.

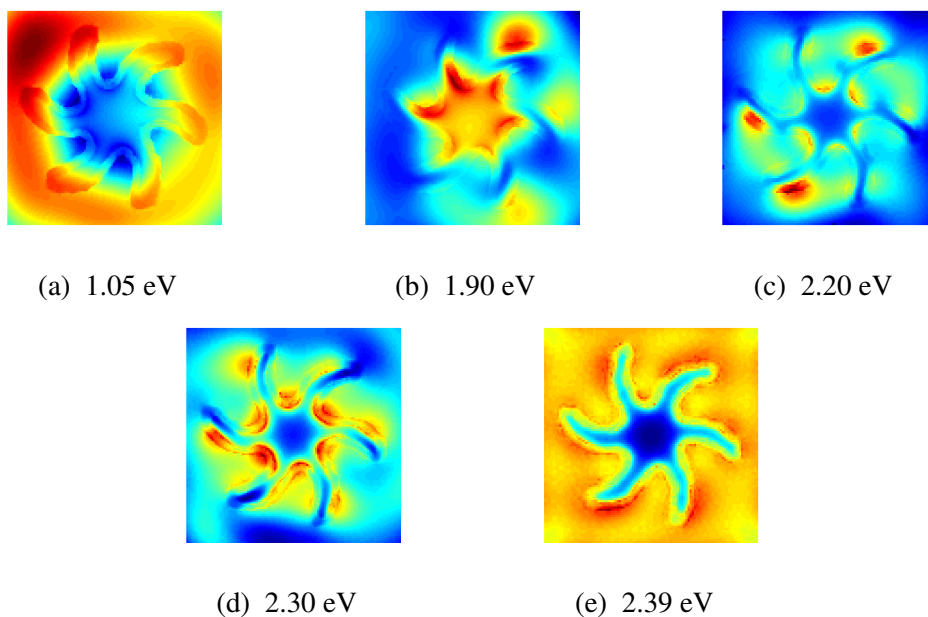


Fig. 3.16 Spatial EELS maps corresponding to the experimental negative particle in Figure 3.1c.

3.6.4 EELS Maps of an Experimentally Realistic Negative Plasmonic Nanoparticle

Using the MNPBEM toolbox the EELS loss maps from the particle shown in Figure 3.1c were also calculated. Figure 3.16 shows the spatial loss maps for the experimental negative particle. Figure 3.16a shows the loss map for the first mode at 1.05eV which shows, as was seen in the previous examples, that the area being excited in the particle is around the tips, but also appears to couple between the arms of the hole. Again the intensity does not appear homogeneous, this can be seen by the more intense region in the upper right hand of the image. This mode appears at 1.05eV in the negative nanoparticle, Figure 3.16a, however it appears at 0.88eV in the corresponding positive particle, Figure 3.15b. The next mode at 1.90eV has an intensity distribution peaking in the centre with a node along the arm. Again not all arms are equally excited and in the centre of the hole there are regions with higher intensity. This mode is similar to the mode at 1.83eV in the positive nanoparticle. The next two modes at 2.20eV and 2.30eV arise from a splitting of a mode as was seen at 2.12eV and 2.15eV in the positive nanoparticle. Again this mode splitting is due to symmetry breaking caused by local roughness around the edges of the hole. In this mode there is a peak in the centre and also one along the arms of the nanoparticle. The final mode for the negative nanoparticle is the bulk plasmon. It is interesting that the first mode in the negative nanoparticle is the furthest in energy from its positive counterpart. It was shown that the ordering of the hexapolar and quadrupolar eigenmodes flipped, these would be the lowest energy modes observed in both nanoparticles thus the change in energy may be accounted by

the change from positive to negative nanoparticle. The next section will calculate the fields created by the localised surface plasmons.

3.7 Electric Fields of the Structures

The variations in the distribution of charge at the resonant loss energies in the nanoparticles also leads to differences in the local E fields. These fields, which decay exponentially with distance from the particle boundary are one of the most interesting applications of SPs and give rise to their applications in areas such a biological and chemical sensors. Figure 3.17 shows the z component of the E fields produced by the ideal nanoparticle, calculated using the eigenmode expansion of Section 3.5. The field is calculated in a plane $30nm$ above the nanoparticle's surface. Figure 3.17a shows the first field, calculated from the monopolar field, and the irreducible representation A_g . Figure 3.17b shows the second field, calculated from the hexapolar eigenvalue, and the irreducible representation B_u . Note the threefold rotation axis and the chirality of the field. Figures 3.17c and 3.17c shows the third and fourth fields, calculated from the quadrupolar eigenvalue, and the irreducible representation E_{2g} . Note the two fold rotation axis, and the chirality of the field. Figures 3.17e and 3.17f shows the fifth and sixth fields, calculated from the dipolar eigenvalue, and the irreducible representation E_{1u} . Note, again the two fold rotation axis, and the chirality of the field. The field chirality can be calculated for these fields. We can compare these results to those for the devised positive nanoparticle. Figure 3.18 shows the z component of the E fields produced by the actual nanoparticle, calculated using the eigenmode expansion in Section 3.5. The field is again calculated in a plane $30nm$ above the nanoparticles surface. Figure 3.18a shows the first field, calculated from the monopolar field, and the irreducible representation A_g , this time the sixfold symmetry is lost and the field is inhomogeneous. Figure 3.18b shows the electric field calculated from the hexapolar eigenmode, and the irreducible representation B_u . Note the threefold rotation axis has gone and the intensity distribution is inhomogenous. The field is also chiral. Figures 3.18c and 3.18c show the fields calculated from the quadrupolar eigenvalues, and the irreducible representation E_{2g} . The two fold rotation axis again has disappeared, and the fields now have a chirality. Figures 3.18e and 3.18f show the fields calculated from the dipolar eigenvalues, and the irreducible representation E_{1u} . Note, again the two fold rotation axis which is present. The field chirality can be calculated for these fields as will be done in the next section.

3.7.1 Field Chirality

As mentioned in the previous sections it is the chiral nature of the fields produced by the plasmonic nanoparticles that give them applications in a number of areas. To quantify what effect structural imperfections have the chiral nature of the fields we will calculate the chirality of the fields around both nanoparticles. We can calculate the chirality of an electric field, ξ ,

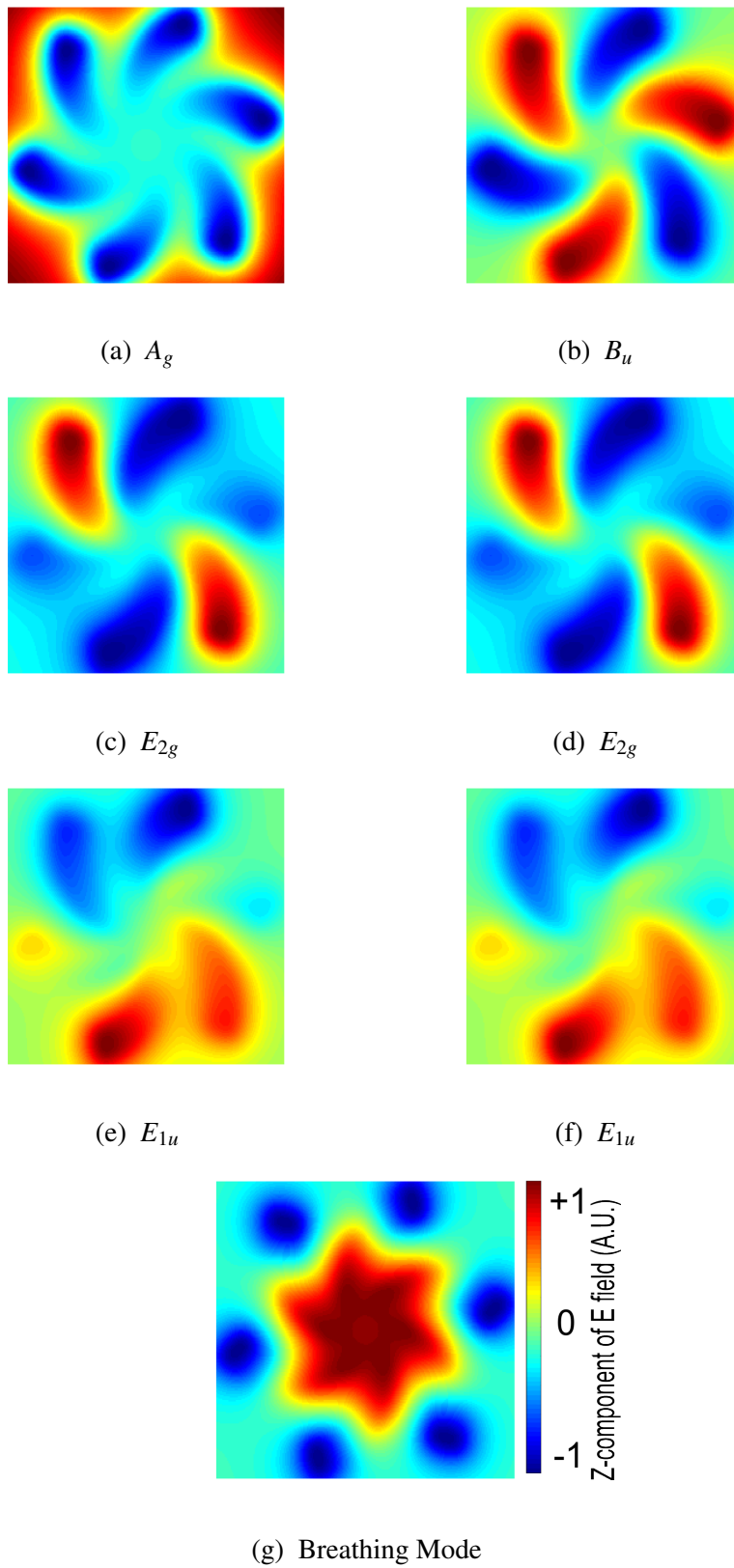


Fig. 3.17 Z- component of E field around the ideal nanoparticle, calculated using an eigenmode expansion. Symmetry terms are used to quantify the loss and group similar terms.

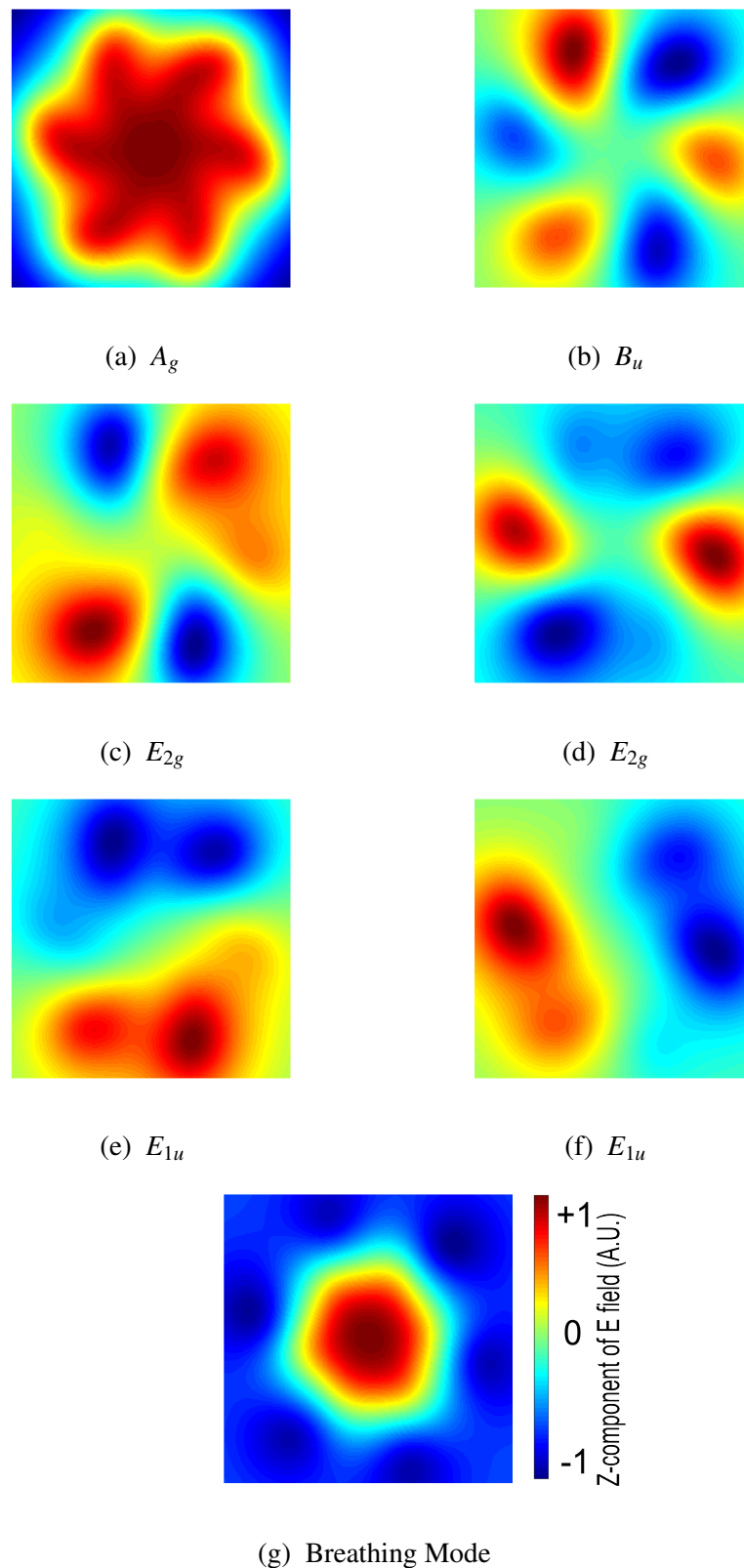


Fig. 3.18 Z- component of E field around the experimentally realistic nanoparticle, calculated using an eigenmode expansion. Symmetry terms are used to quantify the loss and group similar terms.

Table 3.5 The change in E field chirality between an ideal and experimentally realistic plasmonic nanoparticle.

Eigenvalue	$(\xi \cdot \nabla \times \xi)_{Ideal}$	$(\xi \cdot \nabla \times \xi)_{Experiment}$	$(\xi \cdot \nabla \times \xi)_{Ideal}/(\xi \cdot \nabla \times \xi)_{Experiment}$
1	-7.150e-06	5.680e-08	-7.944e-03
2	-3.871e-06	-4.352e-07	1.124e-01
3	-2.318e-06	-1.237e-06	5.335e-01
4	-2.318e-06	7.254e-07	-3.129e-01
5	-7.199e-06	5.362e-07	-7.449e-02
6	-7.199e-06	-8.517e-07	1.183e-01
7	1.833e-07	-1.966e-12	-1.073e-05
8	1.694e-07	1.619e-11	9.555e-05

given as

$$\xi \cdot \nabla \times \xi. \quad (3.22)$$

Table 3.5 shows a comparisons between the chirality of the fields for the ideal and experimentally realistic nanoparticle, calculated at a plane $30nm$ above the surface of the nanoparticles. We see a decreased chirality of the field for the hexapolar and the first quadrupolar modes however the second quadrupolar mode sees an increase in E field chirality. We have seen from the previous sections that these two quadrupolar modes will appear at similar energies however their fields may differ. This means there would an increased sensitivity to chiral fields at this mode, due to the experimentally realistic plasmonic structures shape. This also occurs for one of the dipolar modes. Thus these decreases in symmetry caused by the experimentally realistic plasmonic particles shape may have advantages by increased field chirality. There are numerous examples of chirality being induced by imperfections in the literature, such as magnetic vortices developing chirality due to surface roughness [105].

3.8 Effect of Adding a Substrate

As mentioned in the introduction, adding a substrate to a nanoparticle can have an effect on the modes observed. Which is due to a decrease in symmetry and breaking the planar modes. We can again use symmetry arguments to predict the modes that will be seen. We observe that a reduction in symmetry from C_6h to C_6 by removing the horizontal mirror plane still leads to the same modes appearing when a substrate is added. Figure 3.19 shows the eigenvalues for the ideal nanoparticle when a substrate is added to our calculations. The first eigenmode Figure 3.19a and its associated surface charge distribution has a monopolar intensity, which agrees well with the prediction from the symmetry analysis in Section 3.4 and corresponds to the mode for the A_g irreducible representation. This mode has an eigenvalue of $\lambda = -6.2728$ and when compared to the eigenvalue for the same mode without a substrate, $\lambda = -6.2832$, this represents an increased shift in loss energy. However there is no change in the intensity of the mode; there is still the same shape and distribution. However when

Table 3.6 The calculated dipole moment for the eigenmodes of the ideal nanoparticle with and without a substrate.

Eigenvalue	Without Substrate	With Substrate
1	2.532e-19	7.670e-20
2	5.243e-32	9.065e-21
3	7.020e-32	5.999e-21
4	7.020e-32	5.999e-21
5	5.370e-19	7.096e-19
6	5.370e-19	7.096e-19
7	4.461e-33	3.757e-21
8	5.283e-33	8.360e-22
	dark	bright

looking at the interface of the nanoparticle and the substrate it is clear there is a dipole created at the interface, which leads to an increased dipole moment, and thus modes which would appear dark are now appearing bright. This trend continues for the second eigenmode Figure 3.19b which has a hexapolar intensity and agrees with the B_u mode found from the symmetry analysis, and it has a purely real eigenvalue of $\lambda = -6.035$ which compares to the eigenvalue $\lambda = -6.0411$ without a substrate. The second two eigenmodes Figures 3.19c and 3.19d have quadrupolar like intensity features and the same real part of either eigenvalue $\lambda = -6.0095$ however their (small) imaginary part of the eigenvalues differ in sign, again as predicted by the symmetry analysis displaying the characteristics of the irreducible representations E_{2g} . The fifth and sixth eigenmodes Figures 3.19e and 3.19f display a dipolar intensity pattern and again differ in eigenvalue only in the sign of the imaginary part. The final eigenmode Figure 3.19f again displays something not predicted by the symmetry analysis, which is a higher order breathing mode. This was not predicted as it displays a node along the arms. Our basis was chosen as a localised state on each arm, which is indivisible, thus this mode was not observed. We can compare the eigenvalues seen in both our ideal nanoparticle with and without a substrate and the results are shown in Figure 3.20. We can see that the eigenvalues follow the same trend with and without a substrate, with shifts in eigenvalue showing the shift in energy caused by the addition of the substrate.

Table 3.6 shows a comparison of the calculated dipole moment for the eigenmodes shown in Figure 3.20. For the second eigenmode, which has a hexapolar shape, for the nanoparticle with a substrate we see an increase in the dipole moment, when compared to the simulation without a substrate. This suggests a change in brightness of the mode, again a transition from dark to bright as was seen for the experimentally realistic nanoparticle. Which can be highlighted by the similarity in magnitude of dipole moment when compared to the bright dipolar mode. Thus it can be concluded that when a substrate is added the modes overall do not change, however their brightness does.

Adding a substrate to the ideal nanoparticle also leads to differences in the local E fields. Figure 3.21 shows the z component of the E fields produced by the ideal nanoparticle,

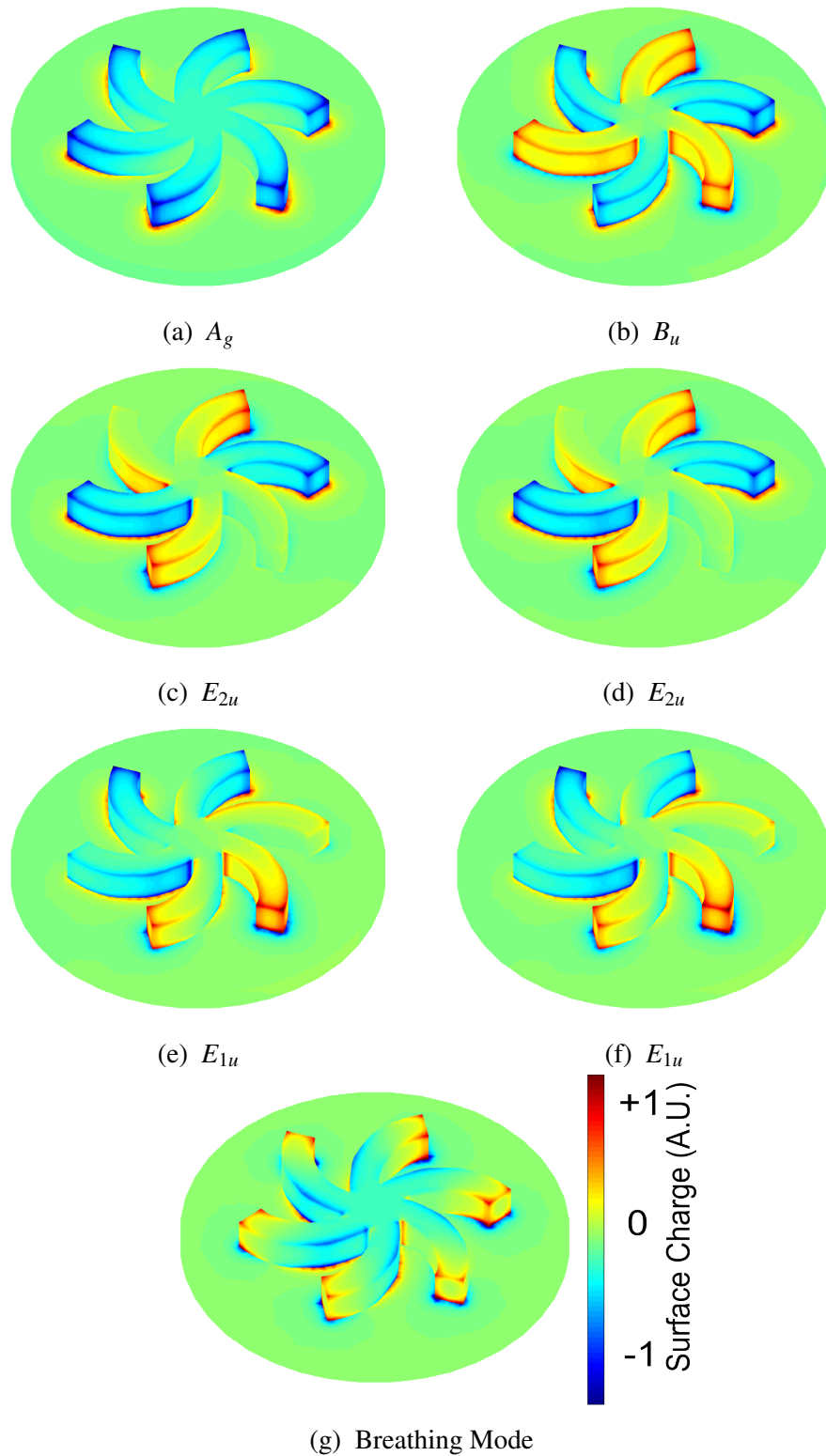


Fig. 3.19 The surface charge eigenvectors, σ_k , of the ideal positive plasmonic structure from Figure 3.1d, with a substrate added. The colourmap represents the intensity of the surface charge, calculated using Eqn 3.20.

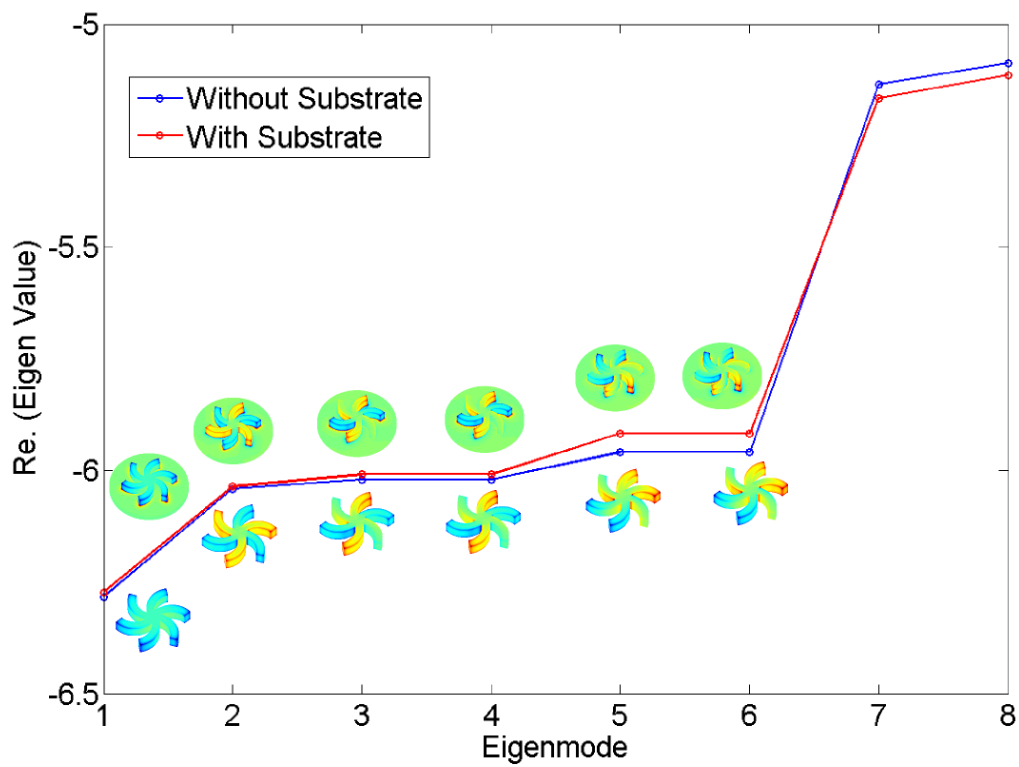


Fig. 3.20 Comparison between the ideal and ideal with substrate eigenvalues. We see a grouping of the eigenmodes in clusters of similar eigenvalues, with only slight shifts in energy shifts until higher order modes.

Table 3.7 The calculated E field chirality for the eigenmodes of the ideal nanoparticle with and without a substrate.

Eigenvalue	$(\xi \cdot \nabla \times \xi)_{WithoutSub}$	$(\xi \cdot \nabla \times \xi)_{WithSub}$	$(\xi \cdot \nabla \times \xi)_{WithoutSub} / (\xi \cdot \nabla \times \xi)_{WithSub}$
1	-7.150e-06	-7.176e-06	1.004e+00
2	-3.871e-06	-2.568e-06	6.634e-01
3	-2.318e-06	-1.002e-06	4.323e-01
4	-2.318e-06	-1.002e-06	4.323e-01
5	-7.199e-06	-3.451e-06	4.793e-01
6	-7.199e-06	-3.451e-06	4.793e-01
7	1.833e-07	1.504e-07	8.205e-01
8	1.694e-07	7.809e-07	4.609e+00

calculated using the eigenmode expansion in Section 3.5. The fields are calculated in a plane 30nm above the nanoparticles surface. Figure 3.21a shows the first field, calculated from the monopolar field, and the irreducible representation A_g . Figure 3.21b shows the second field, calculated from the hexapolar eigenvalue, and the irreducible representation B_u . Note the threefold rotation axis, and the chirality of the field. Figures 3.21c and 3.21d shows the third and fourth fields, calculated from the quadrupolar eigenvalue, and the irreducible representation E_{2g} . Note the two fold rotation axis, and the chirality of the field. Figures 3.21e and 3.21f shows the fifth and sixth fields, calculated from the dipolar eigenvalue, and the irreducible representation E_{1u} . Note, again the two fold rotation axis, and the chirality of the field. The field chirality can be calculated for these fields. There may be a similarity in the field intensity but the magnitude may not be the same.

Table 3.7 shows a comparisons between the chirality of the fields for the nanoparticle with a substrate and without, calculated at a plane 30nm above the surface of the nanoparticles. We see for all modes that the addition of a substrate increases the near-field chirality.

3.9 Conclusion

In this chapter we have shown the effect of variations in the shape and symmetry of four nanoparticles. One highly symmetric ideal particle and an experimentally realistic particle were simulated in order to study the effects of differences in their structures. Eigenmode analysis showed that although there are structural differences the two particles followed the same order of spatial distribution of charge, a calculation purely based on geometric considerations. Simulated EELS maps showed the experimentally realistic particle supported modes which split due to symmetry breaking. The realistic particle also supported bright modes which were dark for the ideal particle. Local variations in roughness was the reasoning behind this mode splitting. However the decrease in symmetry caused by the roughness did not results in a loss of modes, simply a shift in the energy and splitting. The brightness of the modes was observed to change shown by an increase in dipole moment for the hexapolar and quadrupolar modes in the experimentally realistic structure. An increase in near field

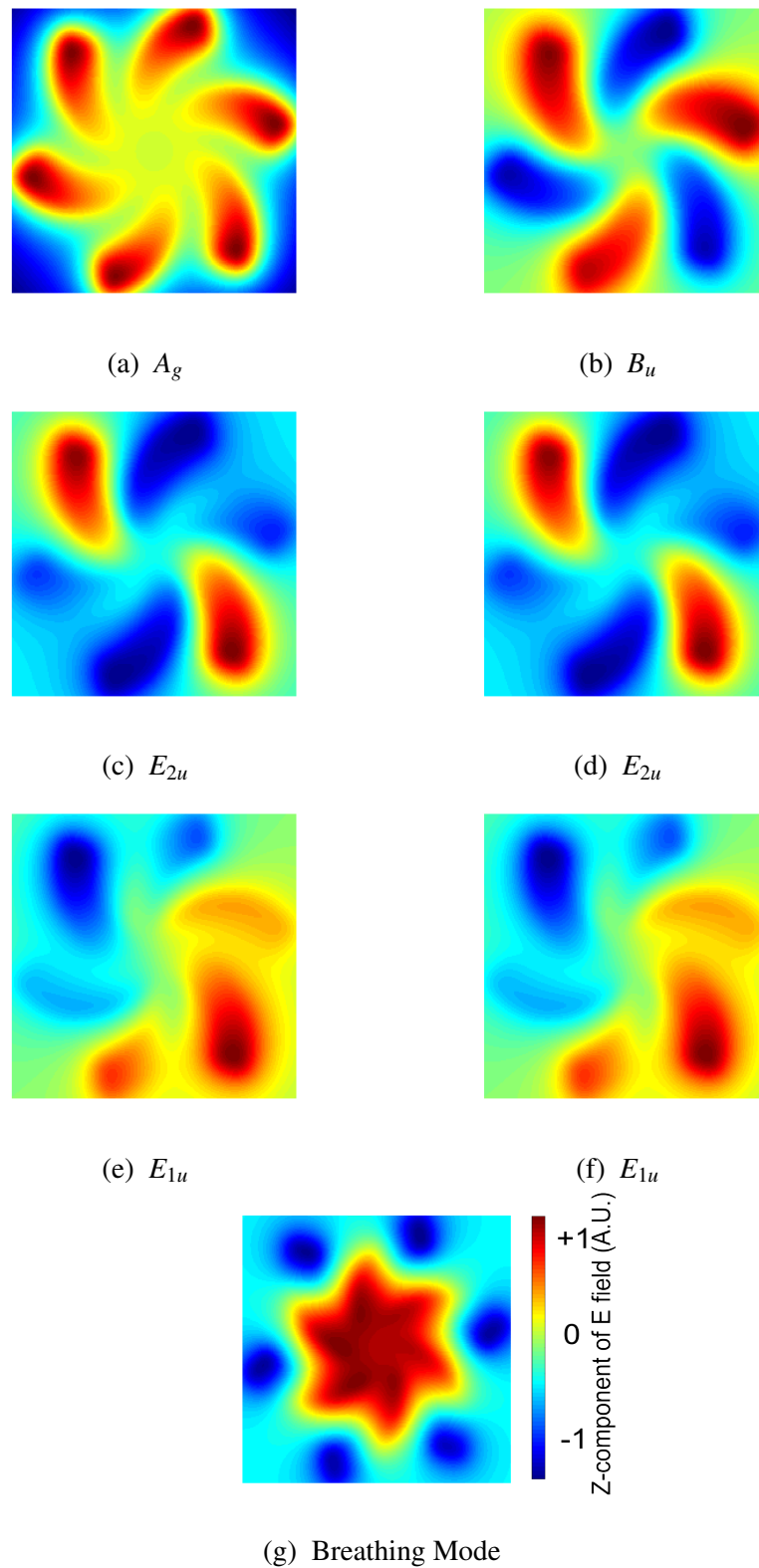


Fig. 3.21 Z- component of E field around the ideal nanoparticle, calculated using an eigenmode expansion. Symmetry terms are used to quantify the loss and group similar terms.

chirality was also observed for some of the modes, showing that a deviation in the shape of a nanoparticle can have an effect on its applications as a sensor of chiral fields. These deviations were compared to the effects of adding a substrate. This also found slight shifts shown by a change in eigenvalue and a change in the brightness of the modes. An increase in near field chirality was also found, which was of the same magnitude as for the effect of structural deviations from an ideal shape.

Two composite nanoparticles were also studied, a hole in a nanoparticle and the positive counterpart. It was found that the two structures had similar modes, in terms of the spatial intensities, however the modes were shifted by up to $0.2eV$ in some cases. This agrees with what was observed in the previous chapter, and highlights that Babinet's principle works in our case. Eigenmode analysis showed a change in the ordering of the lowest energy modes, with a switch from hexapolar to quadrupolar from the positive to the netnegative nanoparticle.

Chapter 4

Convergent Beam Electron Diffraction with Electron Vortex Beams

4.1 Introduction

In this chapter we outline the use of the electron vortex beams as probes of chiral materials. We will begin with a brief review of the history of electron vortex beams, with an emphasis on their production and applications. We will then outline the advances in producing electron vortex beams in the transmission electron microscope as this will be relevant to this work. We will then give a justification of the use of electron vortex beams as probes of chiral materials, highlighting their unique properties which make them a suitable candidate as probes. Then will follow the results of this work where we show enantiospecific scattering in a number of chiral crystals using electron vortex beams.

The study of electron vortex beams began with their optical counterpart. It had been known for some time that single photons could possess a spin, associated with their polarization, but it was only in the last few decades that orbital angular momentum, due to twisted wavefronts, was observed in light [106]. Electrons were also known to possess orbital angular momentum within bound atomic states at the time, but it is only recently that the prospect of free electron beams carrying OAM has been appreciated. Uchida and Tonomura were among the first to produce a free beam of electrons which carried orbital angular momentum [49]. This was achieved by passing a plane wave electron beam through a spiral phase plate which imprinted a spiral phase on the transmitted electron beam. With the production of free beams of electrons carrying orbital angular momentum came the prospect of obtaining electron vortex beams in the electron microscope, something which was soon achieved [46].

In this work the interaction of electron vortex beams with chiral materials is studied by analysis of CBED patterns of chiral potentials related to one another by a mirror plane. The choice of vortex beams was chosen as the current methodology to determine the handedness of a crystal involves taking a series of diffraction patterns through a range of angles which can sometimes require tilt angles which are not easily achievable in some TEMs or by

studying the HOLZ lines which can require thicknesses of a crystal which are undesirable as was discussed in Section 1.6.2. In this work we propose a method by which a pair of electron vortices could be studied by the CBED pattern they produce when scattering through chiral media, which unlike plane waves, can break Friedel's law, which was discussed in Section 1.2.3. The electron vortex beams have a chirality about the axis of propagation, determined by the sign of their OAM, and can be positioned such that their propagation axis is directed along a screw axis of a crystal. Much research has considered the prospects of dichroism in inelastic scattering, which may enable a new form of magnetic imaging [107]. However, elastic diffraction from periodic potentials has not been explored in such detail. Here, we draw inspiration from longstanding structural determinations using photoelectron diffraction, where the OAM of low energy electrons rotates the resulting diffraction patterns by modulating the effective direction of the impinging wavevector [108].

In this chapter we begin by discussing convergent beam electron diffraction, and why this technique will be useful when studying electron vortex beam diffraction. We then introduce electron vortex beam diffraction in an achiral crystal, showing the importance of convergence angles in our work. We will highlight why a Gaussian beam is an insufficient probe to study chiral crystals with an example and will then show why vortex beams are an ideal probe of chiral materials. We will map the location and direction of electrons in a vortex beam passing through a material and investigate how the different OAM values of a vortex beam give rise to different flows of electrons through a material and look at the effect on the entrance and exit beam. To calculate the wavefunction of the beams as they pass through a material the multislice method, discussed in Section 1.8, is used with a modification made by the author. The latter part of this chapter looks at scattering in real crystal structures and compares the results of the simple chiral examples.

During the time of this work a study was published which also used electron vortex beams to study chirality in a similar manner. In their work Juchtmans et al. [109] studied the symmetry of the higher-order Laue zones and were able to identify chirality in an experimental crystal. In their work they did not however consider the effect of the overlapping disks formed in CBED, which marks a difference between our approach and theirs.

4.2 Convergent Beam Electron Diffraction

Convergent beam electron diffraction (CBED) is an experimental technique in which an electron beam, in a TEM, is focused onto a specimen in order to create a nanoscale probe. The technique was first described by Kossel and Mollenstedt in 1939 [110], though it took several decades to become popular as the instrumentation lacked the necessary resolution. Once STEM technology advanced, CBED quickly became one of the most powerful techniques for the determination of crystal structure available to electron microscopists. The difference between conventional diffraction and CBED is shown in Figure 4.1

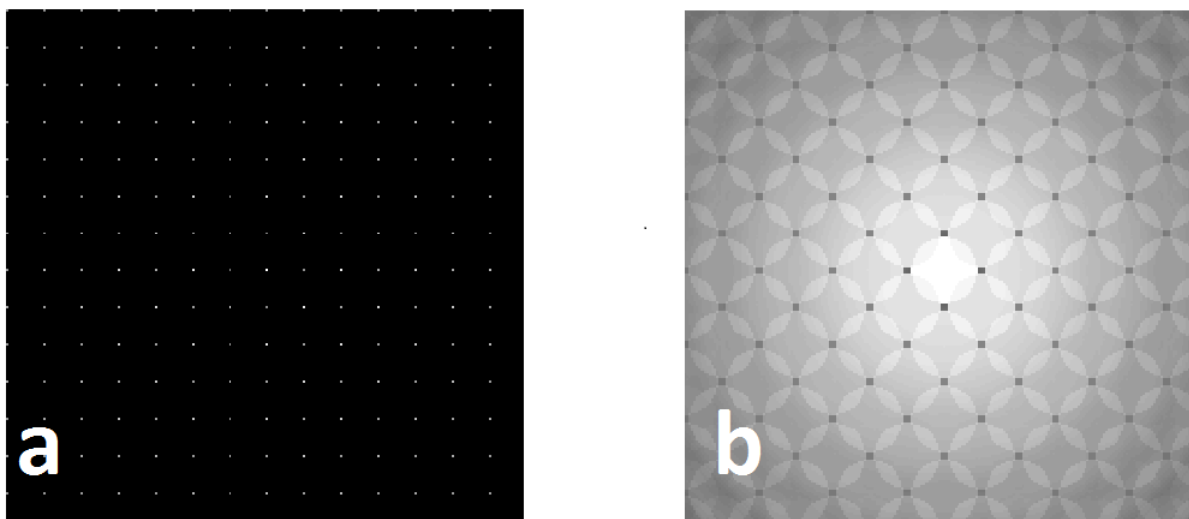


Fig. 4.1 a) Conventional diffraction compared with b) convergent beam electron diffraction (CBED) from a bcc iron crystal oriented along the 100 direction. In conventional diffraction the pattern is made up of sharp spots, whereas in CBED these spots form disks which can overlap.

In a conventional, selected-area electron-diffraction pattern, a parallel beam is used as the probing beam. This results in a diffraction pattern that is formed in the back focal plane made up of sharp Bragg-scattered spots as shown in Figure 4.1a. However in CBED, when a focused beam converges on to a sample, the diffraction pattern is made up of disks whose positions are unchanged but have diameters that depend on the convergence angle of the probe as shown in Figure 4.1b. These disks can either overlap or be spaced apart, which again is dependent on the convergent angle of the probe. We will show in the next few sections that the choice of convergence angle is important for our work, as we find when the disks overlap more information can be obtained from a vortex beam diffraction pattern. Figure 4.2 shows how these overlapping disks occur and one of the features we wish to exploit with vortex beams. The phase of a vortex beam incident on a sample will have points P and Q shown in the figure, which will have a phase difference for a vortex beam, and a constant phase for a planewave. When the diffraction disks from these points overlap for the vortex beam this will result in interference effects which will not be present in conventional diffraction (using planewave illumination). The phase difference for these points will be dependent on how the beam scatters in the crystal, meaning scattering terms with a component parallel to the beam are accessible. It is this region, where the diffraction disks overlap where we will look for chiral determination. This will first be examined for an achiral crystal in the next section.

4.3 Vortex Beam Diffraction in a Achiral Crystal

Using the multislice method two vortex beam wavefunctions and a planewave Gaussian wavefunction are scattered through an achiral bcc crystal of iron. The beam energy is chosen

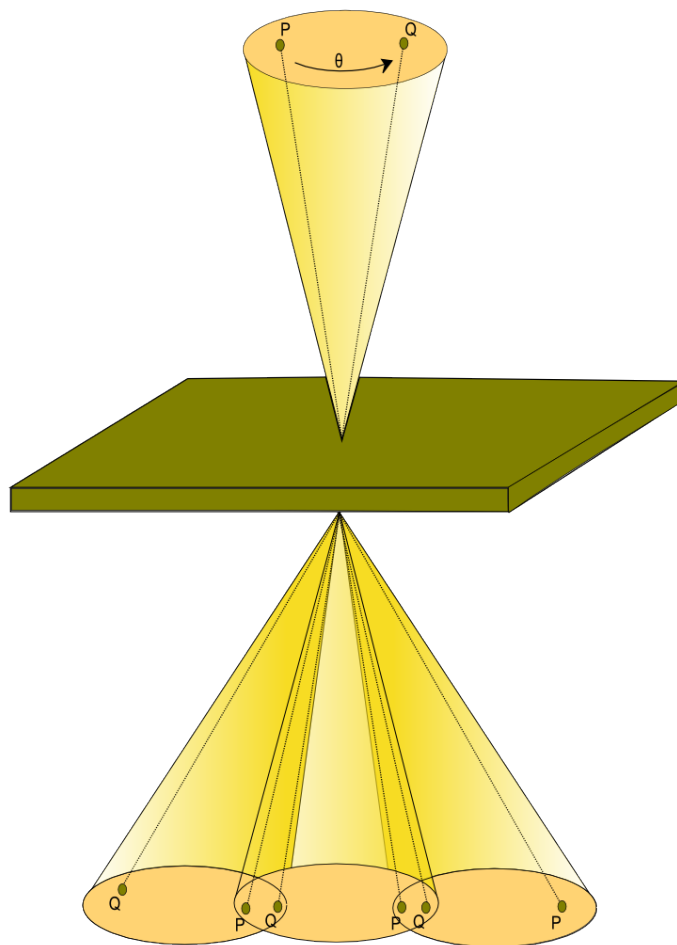


Fig. 4.2 The conventional set up for CBED. In this setup an electron beam originating from point P in the incident beam, will find itself scattered to point P' in the diffraction disks. By adding a phase term to the incident beam (as in a vortex beam) we would expect to see the interference effects in the region where the phase difference is most prominent, this would be in the region of overlap between two disks, as seen in the figure.

to be 200keV and the convergence angle chosen as 8mrad . There are two considerations in selecting the convergence angle. First it must be sufficient to allow the diffracted disks to overlap and interfere. Second it is preferable to ensure the intensity maximum of the vortex beam (an annulus) overlaps with the scattering centres (i.e the atoms) of the crystal unit cell. An 8mrad convergence angle leads to an overlap of the diffraction disks for a bcc iron cell of lattice constant 0.285 nm and also means the probability density disk for the vortex beams lies centered on the unit cell of the crystal. Figure 4.3a-c shows the entrance face probability densities for the three beams and Figure 4.3g-i shows the diffraction patterns after scattering through 10 unit cells of iron. It can be seen (in the overlapping region) that the two vortex beam diffraction patterns are mirror images of one another. If we reflect the diffraction pattern in Figure 4.3g in the mirror plane perpendicular to the page we obtain Figure 4.3i. In the regions of overlapping, indicated by an arrow, the intensity increases in an anticlockwise direction for the pattern in 4.3g and a clockwise direction for the pattern in

4.3i. The two diffraction patterns still possess a fourfold rotation axis, however the planes of symmetry which exist in the diffraction pattern for the Gaussian beam are not present. This difference in the diffraction patterns for the two different signs of vortex beams vanishes when the disks do not overlap. Figure 4.3d-f shows the effect of changing the convergence

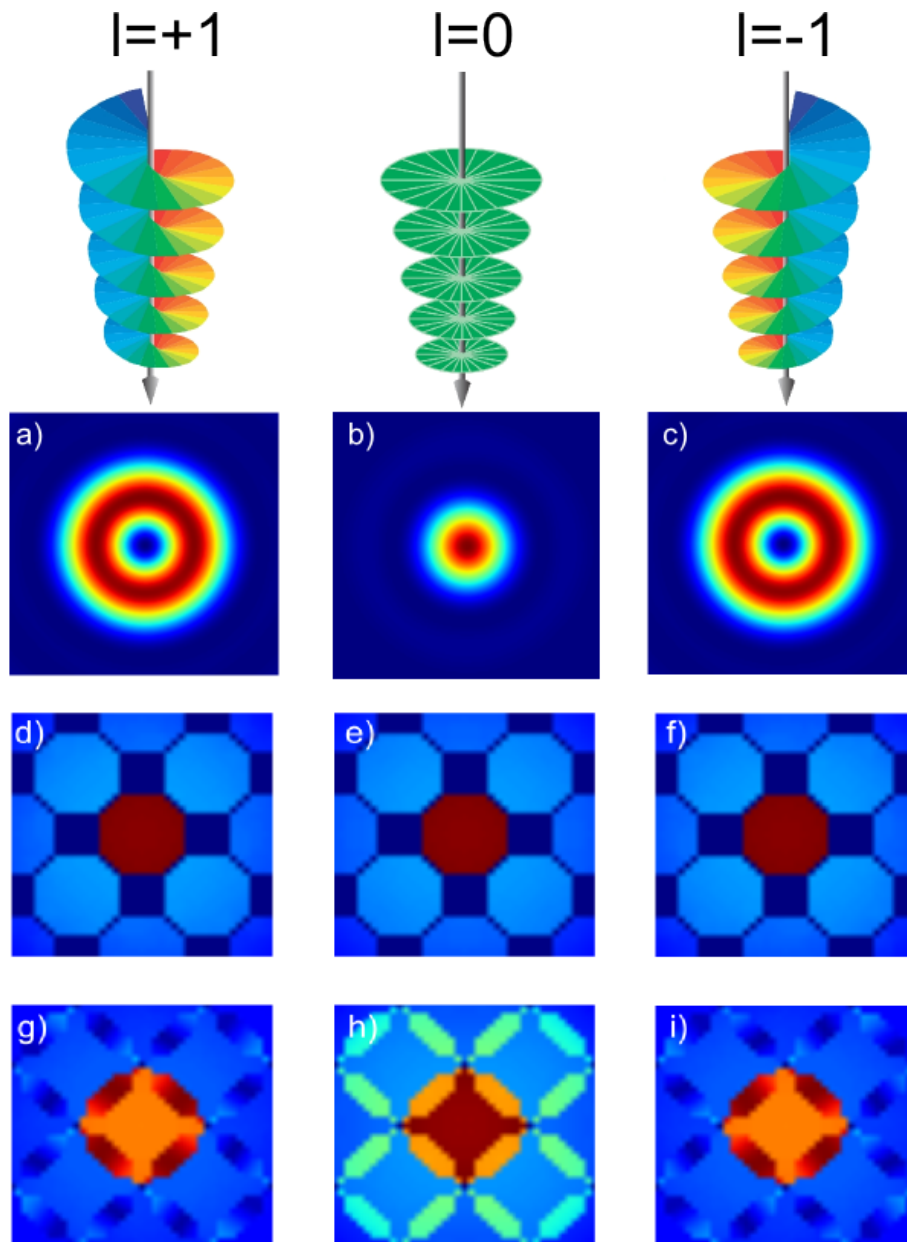


Fig. 4.3 Diffraction patterns for two opposite handed vortex beams a) $|l|=+1$ and c) $|l|=-1$ and b) a Gaussian beam scattering from an achiral bcc iron crystal. The beam energy is 200keV . d-f) show a convergence angle of 6mrad and g-i) the convergence angle is 8mrad . The diffraction patterns are calculated after scattering through 10 unit cells. The simulation was run with 1024×1024 pixels, with real space dimensions of $28.59 \times 28.59 \text{ \AA}$. The intensity scaling in each of the diffraction patterns is the same.

angle. The three panels show the diffraction patterns for a plus (left), Gaussian (middle) and minus (right) beam scattering, as above, through 10 units cells of iron. We see for a

convergence angle of 6mrad the disks do not overlap in the CBED pattern, and the left and right vortex beam patterns are identical. However once the convergence angle is such that the disks overlap, as shown in Figure 4.3g-i, it is here the two patterns have a difference. There are clear, but weak, variations in intensity within the four lozenge-shaped features surrounding the central diffraction disk, the region of overlap with first order diffraction disks. This is an interesting result as it means that with an achiral crystal the handedness of one vortex beam can be distinguished from another. The fact that the differences between the two vortex CBED patterns occurs in the overlap region will form an important part of our study of chiral materials. We explain this difference by considering the schematic shown in Figure 4.2. When the diffraction disks do not overlap the interference effects are not present as we see when the convergence angle is decreased. It is important to note that there may also be intensity differences within the disks themselves, which is why there is a varied intensity distribution within the overlap region.

4.4 Vortex Beam Diffraction in a Square Chiral Crystal

Using the mutlislice program convergent electron beams were propagated through chiral crystals of opposite handedness. The first crystal system studied was a simple (unphysical) square helix, which changes handedness between the two chiral crystals, by reflection in a mirror plane along the propagation direction of the electron beam (the z direction), which is also equivalent to reflection in a plane perpendicular to the page. The potential is chosen to be iron, to compare with other studies in the literature. Figure 4.4 shows the set up for this simulation. The probability density is aligned with the square potential such that the peak intensity of the beam lies on the atomic columns. This is done by choosing a convergence angle of $6mrad$ when the beam energy is $200kev$.

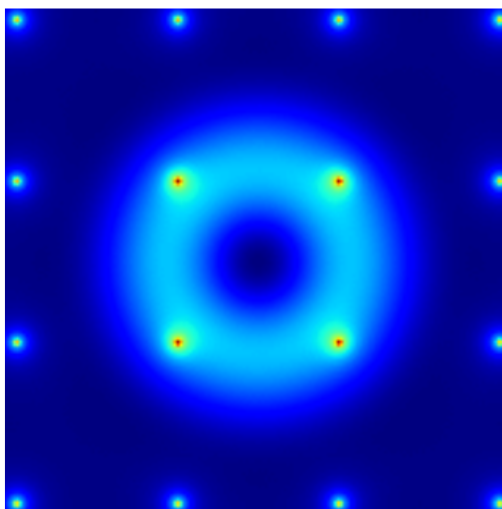


Fig. 4.4 The overlap of the vortex beam probability density with the square chiral potential, looking down the beam direction. The donut shaped intensity is chosen to lie directly over the fourfold helix, this results in overlapping diffraction disks. The radius of the probe is around 1.5 \AA .

Figures 4.5a and 4.5b show the phase fronts of the plus and minus vortex beams incident on the crystal. Figures 4.5c and 4.5d show the projected potential of the crystal looking down the c axis. It is clear when viewed down this axis (the axis of propagation of the beam) that the two crystals are indistinguishable. Figures 4.5e and 4.5f show the atomic positions within the unit cell viewed from the side. We see that the two crystals have opposite twists, with Figure 4.5e having a right handed twist, when viewed down the beam direction. In this case the beam shown in Figure 4.5a and the crystal shown in Figure 4.5e have the same chirality. The CBED patterns obtained from propagating a plus vortex beam ($l = +1$), Gaussian beam and minus ($l = -1$) vortex beam after scattering in the chiral potential in Figure 4.4 are shown in Figure 4.6. The top panel shows scattering in a clockwise crystal and the bottom panel shows scattering in an anticlockwise crystal. We see just by viewing the diffraction

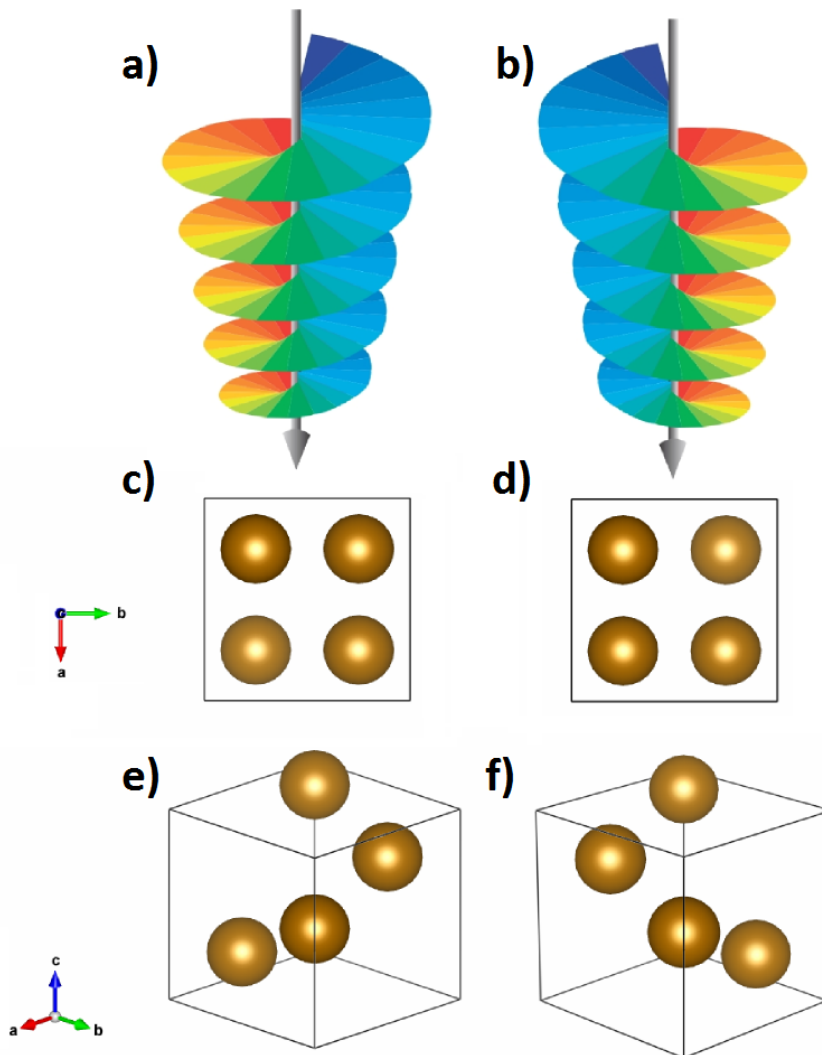


Fig. 4.5 Set up of the simulation for a square chiral crystal showing the (a) plus vortex beam wavefront, (b) minus vortex beam wavefront. (c)-(d) show the entrance face of the crystal viewed along the beam direction. (e)-(f) show the atomic positions within the unit cell.

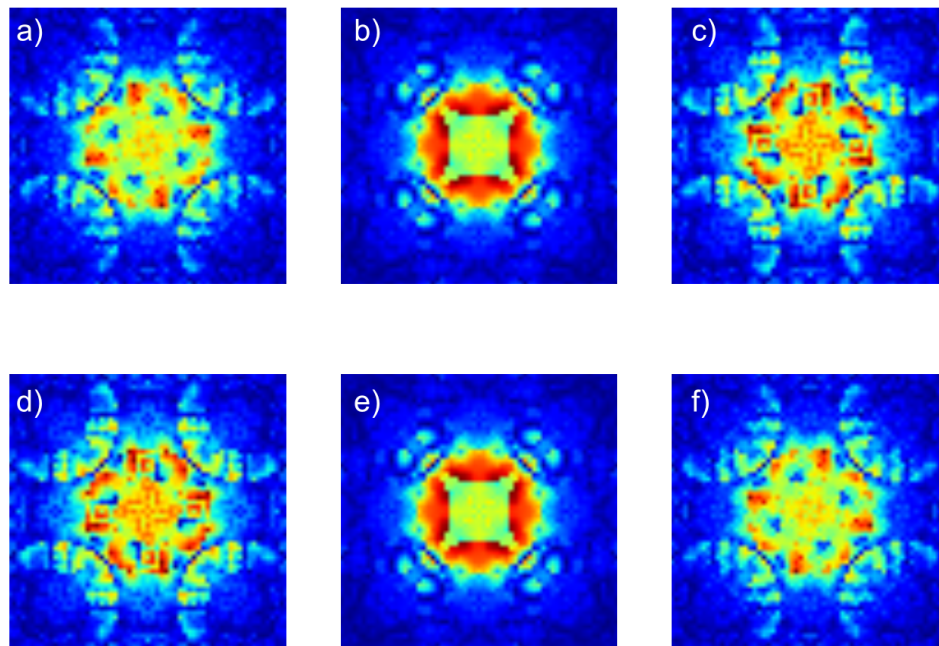


Fig. 4.6 CBED diffraction pattern corresponding to the probability densities shown in Figure 4.7. The differences are shown for a $l=+1$ (left), $l=0$ (middle) and $l=-1$ vortex beam (right) scattering through a left (top) and right (bottom) handed crystal. Notice that several features match between the figures in opposite corners. The thickness of the crystal is 140nm. The simulation was run with 1024×1024 pixels, with real space dimensions of $57.18 \times 57.18 \text{ \AA}$. The beam energy was 200keV and a convergence angle of 6mrad.

patterns that we have enantiospecific scattering. This is highlighted by the similarity of the top left, Figure 4.6a, and bottom right, Figure 4.6f, diffraction patterns and vice versa. The effects are relatively weak but the intensity profiles within the central diffraction disk and particularly within the region of overlapping discs do show systematic differences. A left handed vortex beam scattering in a left handed crystal will be related by a mirror plane (as the diffraction patterns are) to a right handed vortex beam scattering in a right handed crystal. Further, we see that the Gaussian diffraction patterns, shown in the centre panel, do not show an enantiospecific bias; the two Gaussian diffraction patterns, Figure 4.6b and Figure 4.6e, appear identical. We can conclude that the lack of crystal centrosymmetry leads to different scattering which depends on both the beam's chirality and the chirality of the sample. By comparison of the CBED data with simulation, the results of Figure 4.6 demonstrate that it is possible to determine crystal chirality without the need for the collection of a diffraction tilt-series of images. We can explore this difference in scattering further by considering the probability densities at the exit faces.

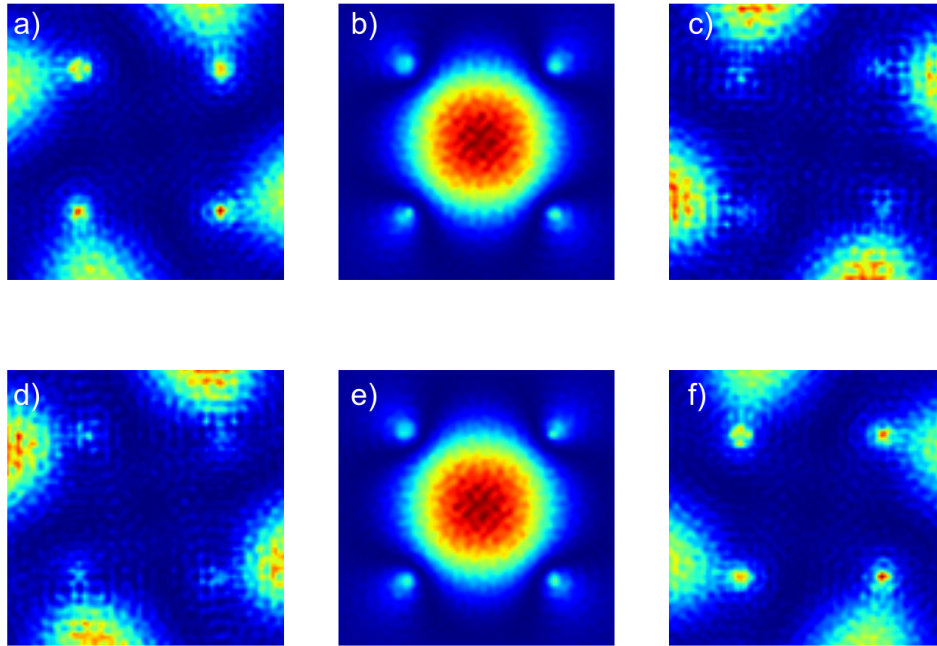


Fig. 4.7 Exit wave probability densities for a $l=+1$ (left), $l=0$ (middle) and $l=-1$ (right) vortex beam scattering through a left (top) and right (bottom) handed crystal. Notice that the intensity distribution within the central disk matches between the figures in opposite corners. The thickness of the crystal is 140nm . The simulation was run with 1024×1024 pixels, with real space dimensions of $57.18 \times 57.18 \text{ \AA}$. The beam energy was 200keV and a convergence angle of 6mrad .

Figure 4.7 shows the probability densities for the exit waves corresponding to the diffraction patterns in Figure 4.6. We see that again we have a matching between the patterns in the opposite corners, Figure 4.7a and Figure 4.7f. While the probability density for the Gaussian beam remains constant between the two crystals, the vortex beams scatter differently, leading to either a channeling effect or a scattering effect. This is shown by the peaked intensity on the four atomic sites where the beam is centered in Figure 4.7a and Figure 4.7f whereas there is a higher probability density outside of the unit cell in Figure 4.7c and Figure 4.7d. If we consider the probability current discussed in the introduction we can imagine the vortex beam scattering from an atom. The current will then flow in the direction of the OAM, which will either be towards or away from the next atom in the chain, depending on the chirality of the crystal. The beam will either be channeled if there is an atom there or scattered outward if there is not. This is why for one crystal the beam appears more intense further from the center of the probe position, than it does for the other crystal. There will be phase associated with each point in the probability density and this will result in the diffraction patterns seen previously. There is a clear forward-scattering intensity lobe from each scattering centre,

directed with sense of rotation that is determined by the incident vortex beam. It is the overlap of this chiral forward-scattering intensity distribution with subsequent scattering centres that gives rise to chiral specificity in the final diffraction patterns.

We now consider what happens in a thinner crystal. Figure 4.8 shows the probability density of the two opposite handed vortex beams after scattering through a thinner crystal, $28nm$ thick, of opposite handedness. The top panel shows the probability densities after scattering through an anticlockwise crystal and the bottom panel shows results for a clockwise crystal. The left panels are a $l = 1$ vortex beam and the right panels are a $l = -1$ vortex beam. We see that in contrast to the previous pattern that the scattering intensity in this case is dominated by the handedness of the beam. This can be seen from the overall shape of the probability density, with the two patterns on the left appearing similar ($l = +1$), and also the two on the right ($l = -1$). However by looking at the intensity centered around the atomic columns we see that already the chiral interaction of the beam is leading to different channeling effects and thus the central intensity (focused around the atoms) is starting to align between the patterns in the opposite corners. This can be seen by comparing the higher intensity located on the two atomic positions in Figure 4.8a and Figure 4.8d, whereas only one atomic position has a high intensity in Figure 4.8b and Figure 4.8c. Thus in this case enantiospecific scattering is not present but is emerging.

Figure 4.9 shows the diffraction patterns relating to the probability densities shown in Figure 4.8. We see that similar to what was seen in the probability density patterns, the diffraction patterns are dominated by the handedness of the beam rather than any immediate effects that can be seen from the interaction of the beam chirality with the crystal chirality. A lower beam energy would be required to enhance the effects at this thickness so that the forward scattering lobe from one layer intersects a scattering centre on the subsequent layer. Figure 4.10 shows the diffraction patterns of the three electron beams after scattering through a thinner crystal of $28nm$ but with a lower beam energy of $60kev$. In order to maintain the same overlap of the probability density and the unit cell the convergence angle was also changed. We see by reducing the energy of the probes that we can obtain enantiospecific scattering at much thinner crystals. This is shown by the similarities between the diffraction patterns on opposite corners. It's important to note that the effects are much more subtle in this case. Comparing Figure 4.10a and Figure 4.10f we see similarities in the central region but, importantly, we also can observe an intensity similarity in the region of overlap of the disks. Figure 4.10a and Figure 4.10f both have a brighter spot in the region of overlap, whereas Figure 4.10c and Figure 4.10d both have a higher intensity across the regions of overlap of the central disk and the four first disks. Overall the diffraction pattern intensity is dominated by the sign of the beam, as was seen before, but intensity differences in the overlapping regions give clues to the difference in scattering due to the handedness of the chiral. Again the Gaussian example does not vary between the crystals at this thickness. Figures 4.11 and 4.12 show the diffraction patterns of the three electron beams after scattering through an even thinner crystal of thickness $11nm$ and with a lower beam energy of $10kev$

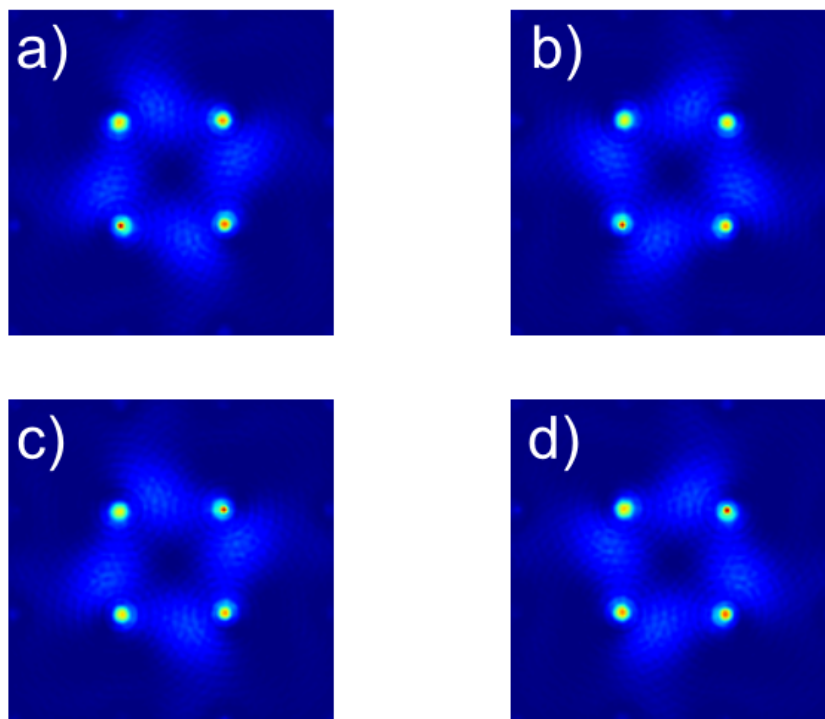


Fig. 4.8 Exit wave probability densities for a $l=+1$ (left) and $l=-1$ vortex beam (right) scattering through a left (top) and right (bottom) handed crystal. Note the similarities of the pattern from beams of the same sign. Features are dominated by the vortex beam sign. The thickness of the crystal is 28nm. The simulation was run with 1024×1024 pixels, with real space dimensions of $57.18 \times 57.18 \text{ \AA}$. The beam energy was 200keV and a convergence angle of 6mrad .

but with two different convergence angles. Figure 4.11 shows results for a convergence angle of $\alpha = 19.46\text{mrad}$ which means the disks do not overlap, and Figure 4.12 shows results for a convergence angle of $\alpha = 29.19\text{mrad}$ which means the disks do overlap. It's clear when comparing the two sets of diffraction patterns the importance of the choice of convergence angle. When the disks do not overlap in Figures 4.11 then it can be difficult to distinguish between the vortex beams scattering in opposite crystals. Figures 4.11a and 4.11f may appear identical at first glance however there is a slight intensity difference when comparing the brightest points on the four disks which surround the central disk. This is evident in the bright spot which appears in the overlap regions of Figures 4.12a and 4.12f. This is similar to what was seen for the 60keV beam in Figure 4.10. It can also be observed that there is a higher intensity (shown by the darker red color) in the region of overlap of Figures 4.12c and 4.12d. Again, for both examples, the Gaussian beam does not vary between the crystals at this thickness as shown by the unchanged diffraction pattern.

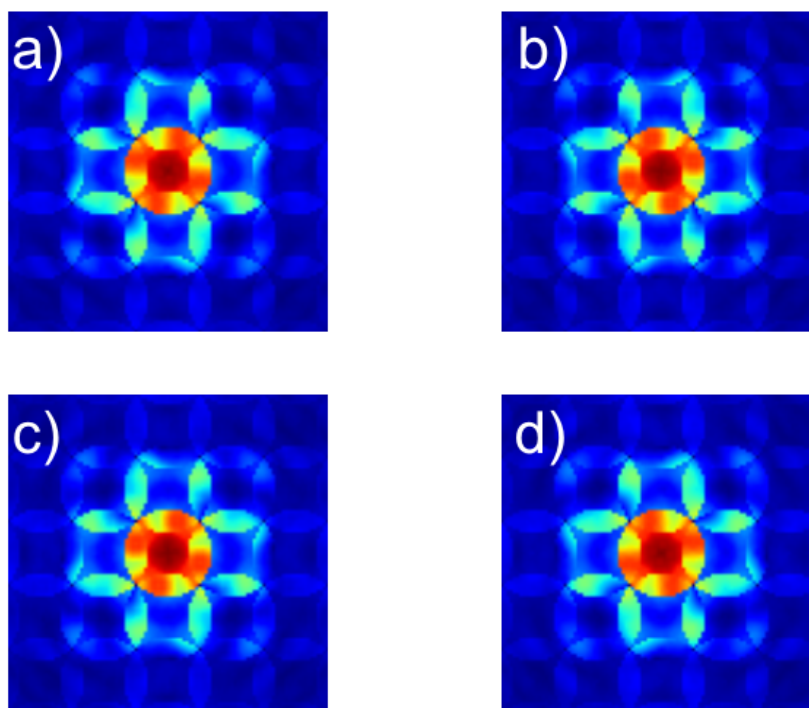


Fig. 4.9 CBED diffraction pattern corresponding to the probability densities shown in Figure 4.8. The differences are shown for a $l=+1$ (left) and $l=-1$ vortex beam (right) scattering through a left (top) and right (bottom) handed crystal. The vortex beam sign is the dominant feature in the patterns. The thickness of the crystal is 28nm. The simulation was run with 1024×1024 pixels, with real space dimensions of $57.18 \times 57.18 \text{ \AA}$. The beam energy was 200keV and a convergence angle of 6mrad.

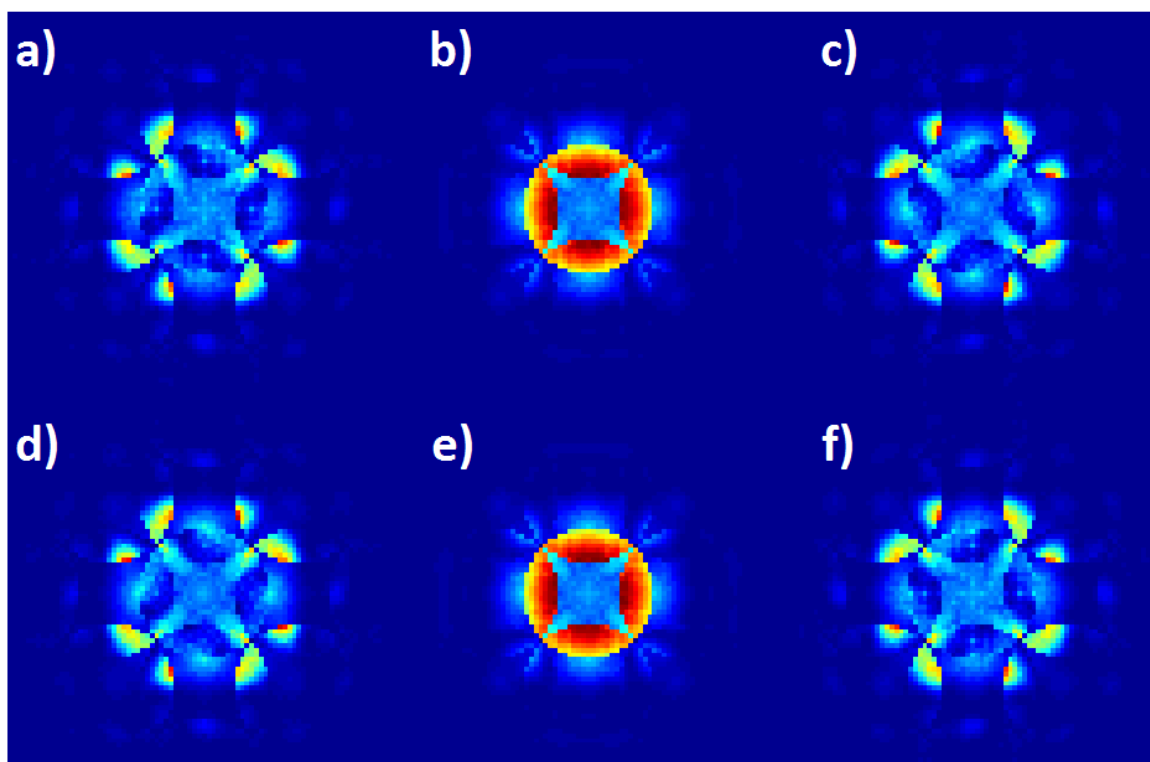


Fig. 4.10 CBED patterns for scattering from a thin square chiral crystal. The thickness of the crystal is 28nm. The simulation was run with 1024×1024 pixels, with real space dimensions of $57.18 \times 57.18 \text{ \AA}$. The beam energy was 60keV and a convergence angle of 11.64mrad.

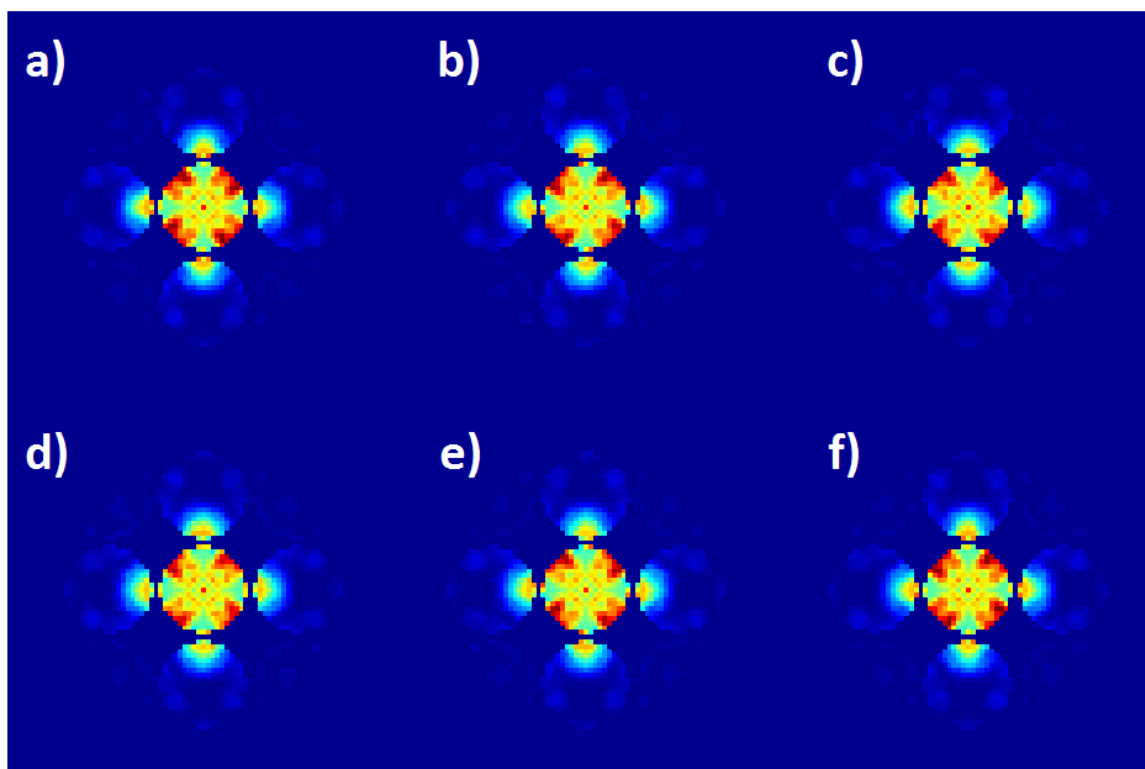


Fig. 4.11 Exit wave diffraction patterns for a square chiral crystal. The thickness of the crystal is 11nm. The simulation was run with 1024×1024 pixels, with real space dimensions of $57.18 \times 57.18 \text{ \AA}$. The beam energy was 10keV and a convergence angle of 19.46 mrad .

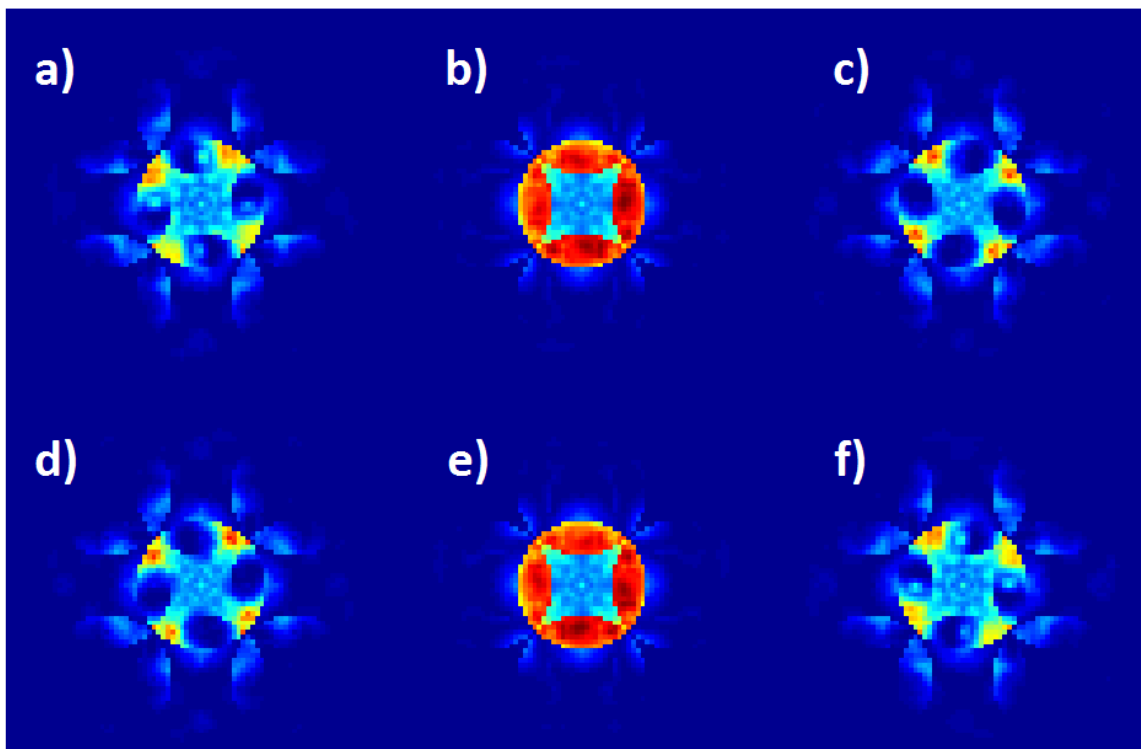


Fig. 4.12 Exit wave diffraction patterns for a square chiral crystal. The thickness of the crystal is 11nm. The simulation was run with 1024×1024 pixels, with real space dimensions of $57.18 \times 57.18 \text{ \AA}$. The beam energy was 10keV and a convergence angle of 29.19 mrad . Differences are now more apparent in the region of overlap.

4.5 Vortex Beam Diffraction in a Hexagonal Chiral Crystal

The third crystal system studied was a simple hexagonal helix. The crystal structure changes handedness between the two chiral crystals, by reflection in a mirror plane along the propagation direction of the electron beam (the z direction). This reflection in the z -direction is equivalent to reflection in a plane perpendicular to the page as was seen for the previous two sections and the atoms are iron. The probability density is aligned with the hexagonal potential such that the peak intensity of the beam lies on the atomic columns. Figure 4.13 shows the overlap of the beam and the atomic columns. The CBED patterns obtained

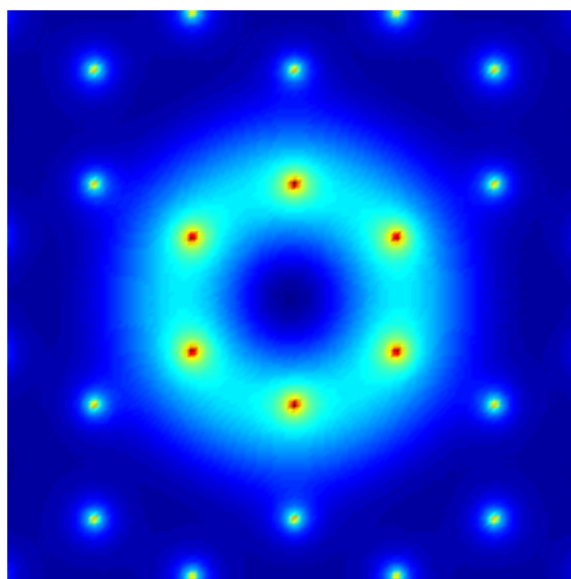


Fig. 4.13 The overlap of the vortex beam probability density with the hexagonal chiral potential, looking down the beam direction. The donut shaped intensity is chosen to lie directly over the sixfold helix, this results in overlapping diffraction disks.

from propagating a plus vortex beam ($l = +1$), Gaussian beam and minus ($l = -1$) vortex beam after scattering in the chiral potential in Figure 4.13 are shown in Figure 4.14. The top panel shows scattering in a clockwise crystal and the bottom panel shows scattering in an anticlockwise crystal, the crystal thickness was $9nm$. The beam energy is $10kev$ and the convergence angle was chosen to be $\alpha = 35.26mrad$. For this convergence angle we see that the disks overlap. In this example the effect of overlapping disks is to create a difference in intensity in the overlapping regions, as was seen in the previous examples. In Figure 4.14a and 4.14f there is a higher intensity in the central region of the CBED pattern but also in each of the overlapping regions of the central disk and those which surround it. Whereas in Figure 4.14c and 4.14d the intensity is focused on one disk. As was seen in the previous examples at such small thicknesses the overall intensity profile of the CBED pattern is dominated by the sign of the beam, however small effects due to the difference in scattering appear in the regions of overlap. These differences stem from the difference in scattering. Figure 4.16

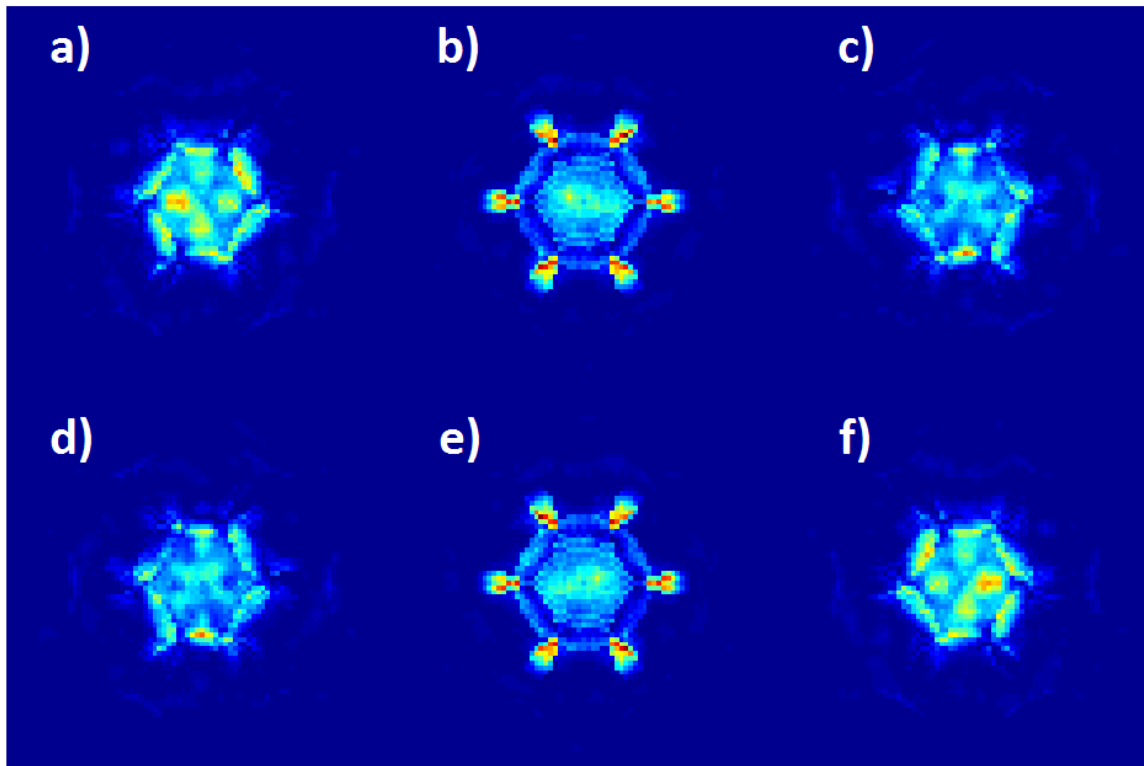


Fig. 4.14 CBED patterns from scattering with the hexagonal crystal. The thickness of the crystal is 9 nm. The simulation was run with 1024×1024 pixels, with real space dimensions of 49.6×49.6 Å. The beam energy was 10keV and a convergence angle of 35.26mrad .

shows the probability densities at the exit surface for the beams shown in Figure 4.14. We see that by focusing the beam onto the six central atoms which centre on the screw axis, we get differences in scattering between the beams. For the beams in opposite corners, Figure 4.16a and 4.16f we see that the six central atoms have a higher intensity whereas in Figure 4.16c and 4.16d the intensity is localised in around one atom. We also see that for the Gaussian example the electrons have been scattered further way from the beam centre which is interesting as the Gaussian beam overall has a more localized probability density, as was shown in Figure 1.15. This shows that the vortex beam circulating probability current is confining the probability density due to a region close to the chiral centre. Figure 4.17 shows CBED patterns obtained from propagating a plus vortex beam, Gaussian beam and minus vortex beam through the chiral potential in Figure 4.13. In this simulation the beam energy is 200keV and the thickness of the crystal is 47nm. To get an overlap of the CBED disks the convergence angle was chosen to be 7.24mrad . We see just by viewing the diffraction patterns that we have enantiospecific scattering. This is highlighted by the similarity of the bottom left and top right diffraction patterns and vice versa. Again the similarities arise from the overlap of the CBED disks. We explain this difference in CBED pattern by comparing the probability densities. Figure 4.18 shows the probability densities corresponding to the diffraction patterns in Figure 4.17. We see a similar story as was seen before, namely that the beam in one instance is being channeled within the unit cell, where the chirality is present

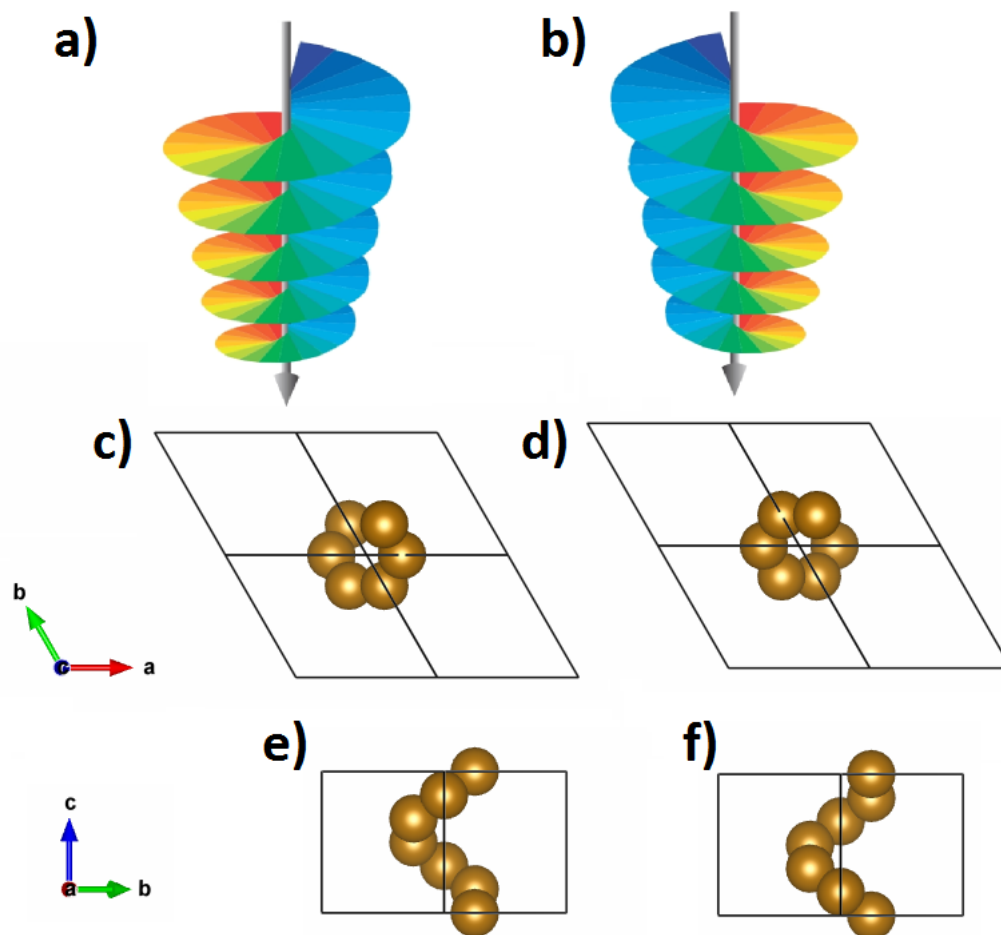


Fig. 4.15 Set up of the simulation for a hexagonal chiral crystal showing the (a) plus vortex beam wavefront, (b) minus vortex beam wavefront. (c)-(d) show the entrance face of the crystal viewed along the beam direction. (e)-(f) show the atomic positions within the unit cell.

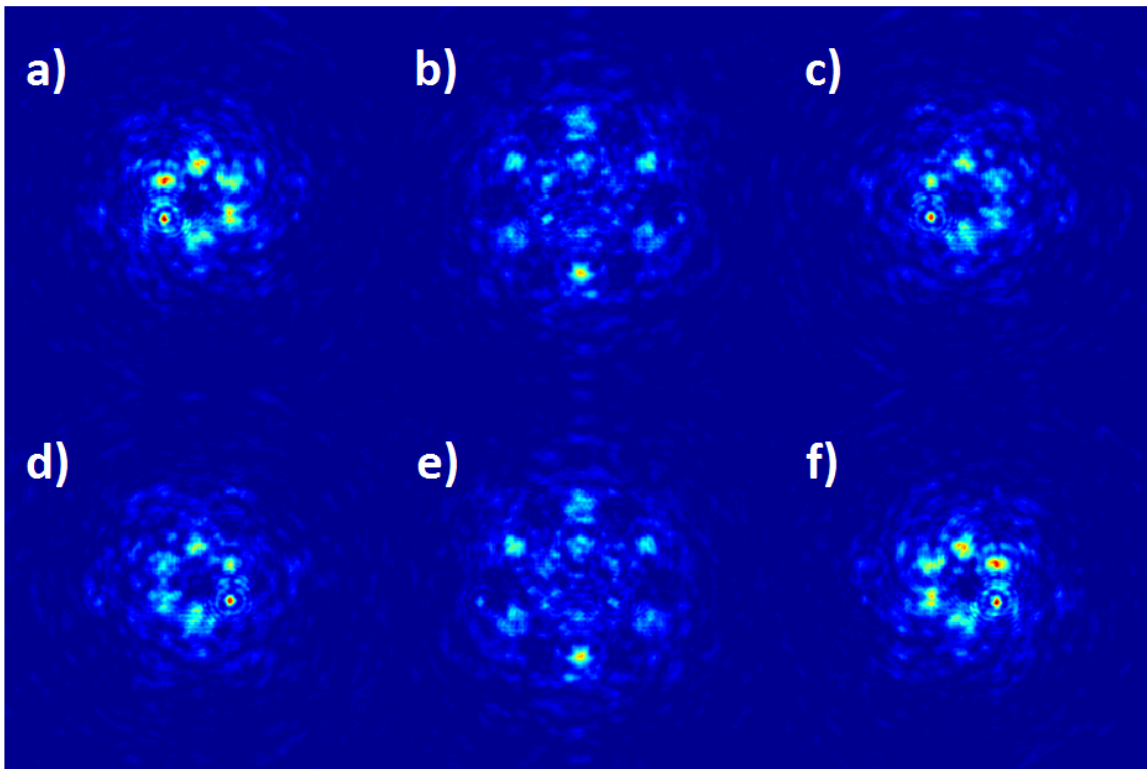


Fig. 4.16 Probability densities for scattering from a hexagonal chiral crystal. The thickness of the crystal is 9 nm. The simulation was run with 1024×1024 pixels, with real space dimensions of 49.6×49.6 Å. The beam energy was 10keV and a convergence angle of 35.26 mrad.

and for the other the intensity is higher outside of the main region, suggesting the electrons are being forward scattered outward. Also it can be seen in the Gaussian example that there is a small, but noticeable intensity further out from the central beam position than for the vortex beams. This further demonstrates the difference in scattering between vortex beams and planewaves. This difference in scattering, where one beam is channeled along the chiral axis, and the other is scattered outwards would lead to a change in integrated intensity as electrons which are scattered outwards are lost from the calculation. Figure 4.19 shows the integrated intensities for the three electron beams scattering in both the clockwise and anticlockwise crystals. Figure 4.19a shows the integrated intensity of a plus ($l = +1$) vortex beam scattering in the clockwise and anticlockwise six-folded chiral crystal described at the start of this section. To begin the beams have the same normalised integrated intensity. We see that as the beam scatters through more potential layers that the two crystal structures lead to differing integrated intensity, with the anticlockwise crystal leading to a more gradual decrease in integrated intensity. Conversely for a Gaussian beam ($l = 0$), as shown in Figure 4.19b, both crystals produce the same drop in integrated intensity. Importantly the minus vortex beam ($l = -1$) produces a mirror image of the plus vortex beam, where the clockwise crystal produces the more gradual decrease in integrated intensity. This supports what was observed when viewing the probability densities where the difference in scattering between

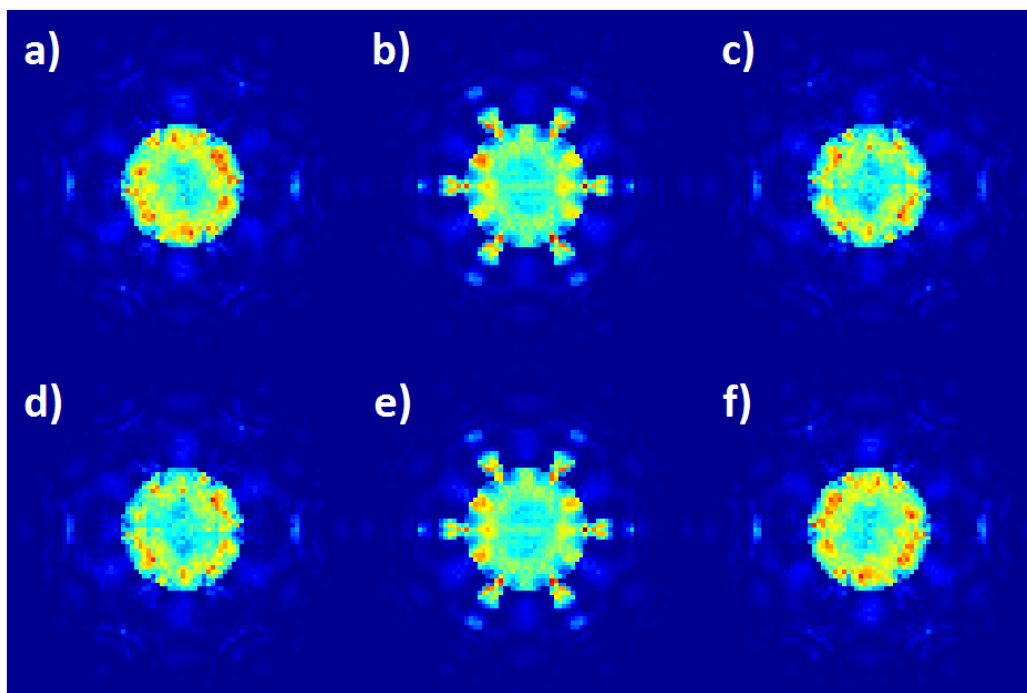


Fig. 4.17 CBED diffraction patterns for scattering from a hexagonal chiral crystal. The thickness of the crystal is 47 nm. The simulation was run with 1024×1024 pixels, with real space dimensions of 49.6×49.6 Å. The beam energy was 200keV and a convergence angle of 7.24mrad.

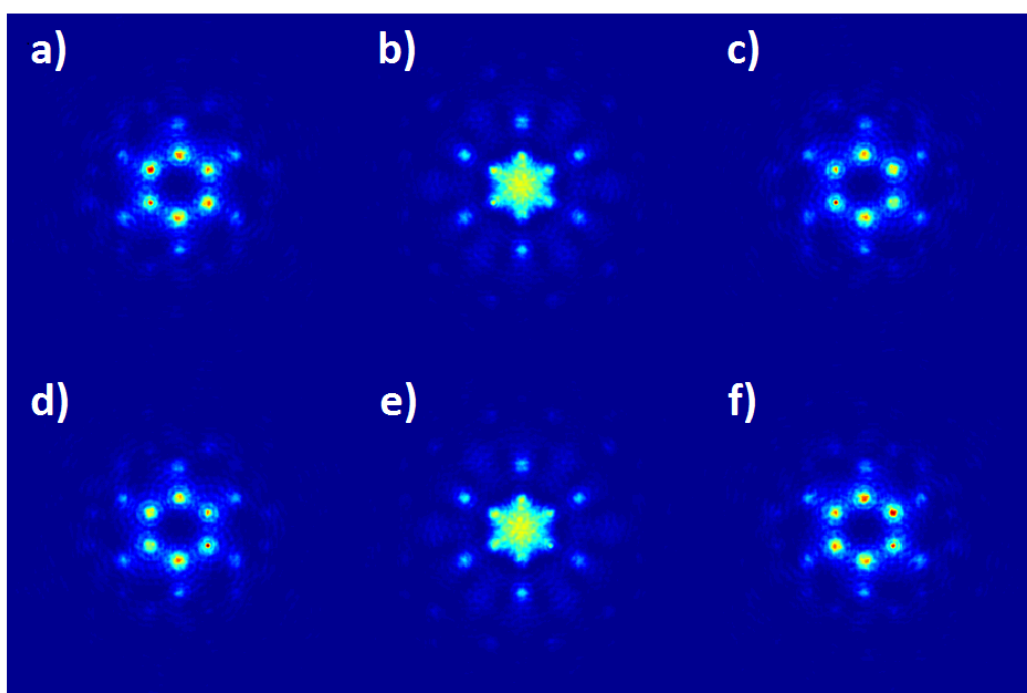


Fig. 4.18 Probability densities for scattering from a hexagonal chiral crystal. The thickness of the crystal is 47 nm. The simulation was run with 1024×1024 pixels, with real space dimensions of 49.6×49.6 Å. The beam energy was 200keV and a convergence angle of 7.24mrad.

the crystals resulted in electrons being scattered further from the beam centre in one scenario and channeled in the other.

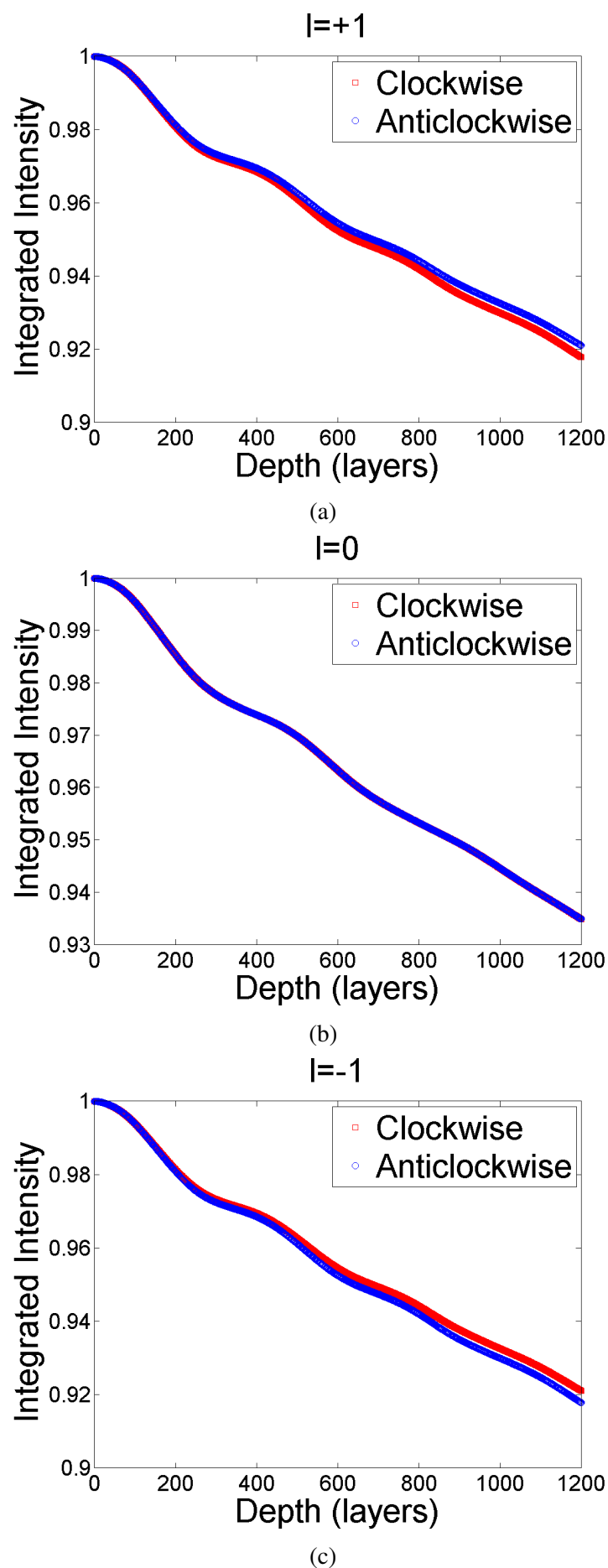


Fig. 4.19 Integrated intensities of a) $l = +1$ b) $l = 0$ and c) $l = -1$ electron beam scattering through both a clockwise and anticlockwise sixfold screw axis arrangement of iron atoms.

4.6 Vortex Beam Diffraction in Quartz

Up until now we have demonstrated enantiospecific scattering in simple geometric crystals. It will now be studied what happens in a real crystal structure. α -quartz was chosen as it exists naturally in two enantiomorphically related structures, D-quartz and L-quartz, belonging to the space groups $P3_121$ and $P3_221$ respectively [111]. These space groups possess an anticlockwise and clockwise 3-fold screw axis, respectively, when viewed down the c-axis. Figure 4.20a and 4.20b show the unit cells of L-quartz and D-quartz respectively. To investigate the interaction of the vortex beams with the chirality of the quartz an appropriate convergence angle was used to define the beam radius at the crystal's entrance face. This is optimised by choosing a convergence angle such that the donut-shaped intensity pattern of the vortex beam can be positioned with maximal intensity over the chiral scattering centres, which in this case form a helix of Si and O atoms within the quartz, shown in Figure 4.21. To maximise asymmetric, chiral diffraction the beam is also positioned to be incident along the screw axis of the crystal. For a 200keV beam, the convergence angle is chosen to be 8 mrad, resulting in a probe of 0.14 nm radius. The CBED patterns obtained from propagating

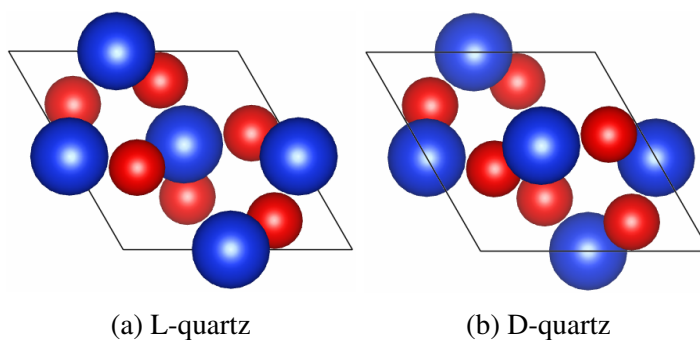


Fig. 4.20 The unit cells of α Quartz showing the two different chiral configurations (a) L-Quartz which contains a left handed screw axis and (b) D-Quartz which contains a right handed screw axis when looking down the 001 direction.

a plus vortex beam and a minus vortex beam after scattering in the chiral potential shown in Figures 4.20a and 4.20b are shown in Figure 4.22. The top panel shows scattering in a clockwise crystal and the bottom panel shows scattering in an anticlockwise crystal. To create the anticlockwise crystal the clockwise crystal was reflected in the z-direction. We see just by viewing the diffraction patterns that we do not have enantiospecific scattering. This is highlighted by the lack of similarity of the top left, Figure 4.22a and bottom right, Figure 4.22f diffraction patterns and vice versa. We see that the two diffraction patterns corresponding to the plus beam Figure 4.22a and Figure 4.22d have a similar triangular intensity in the outer part of the diffraction pattern which is not present in Figure 4.22c and Figure 4.22f. It is also important to note that Figure 4.22b and Figure 4.22e are also noticeably different which can be seen from central region of the diffraction pattern. This hints that flipping the crystal along the z-direction does not result in a similar crystal. Figure 4.23 shows each of the atoms in the unit cell of L- and D-quartz numbered to show its height in the unit cell. We

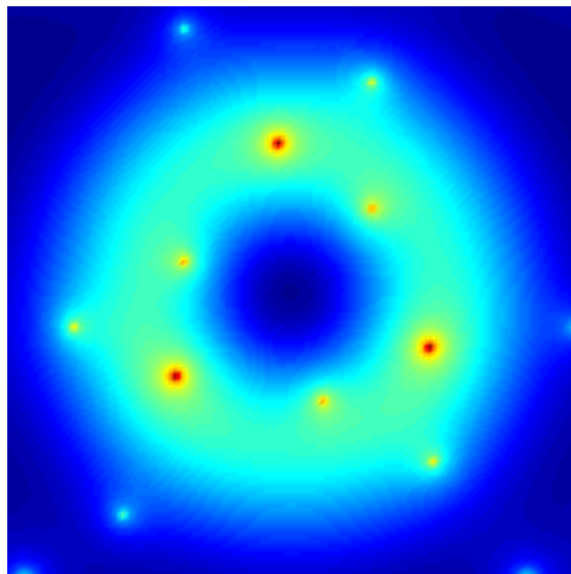


Fig. 4.21 The overlap of the vortex beam probability density on the quartz chiral potential, looking down the beam direction. The donut shaped intensity is chosen to lie directly over the screw axis of the crystal, this results in overlapping diffraction disks.

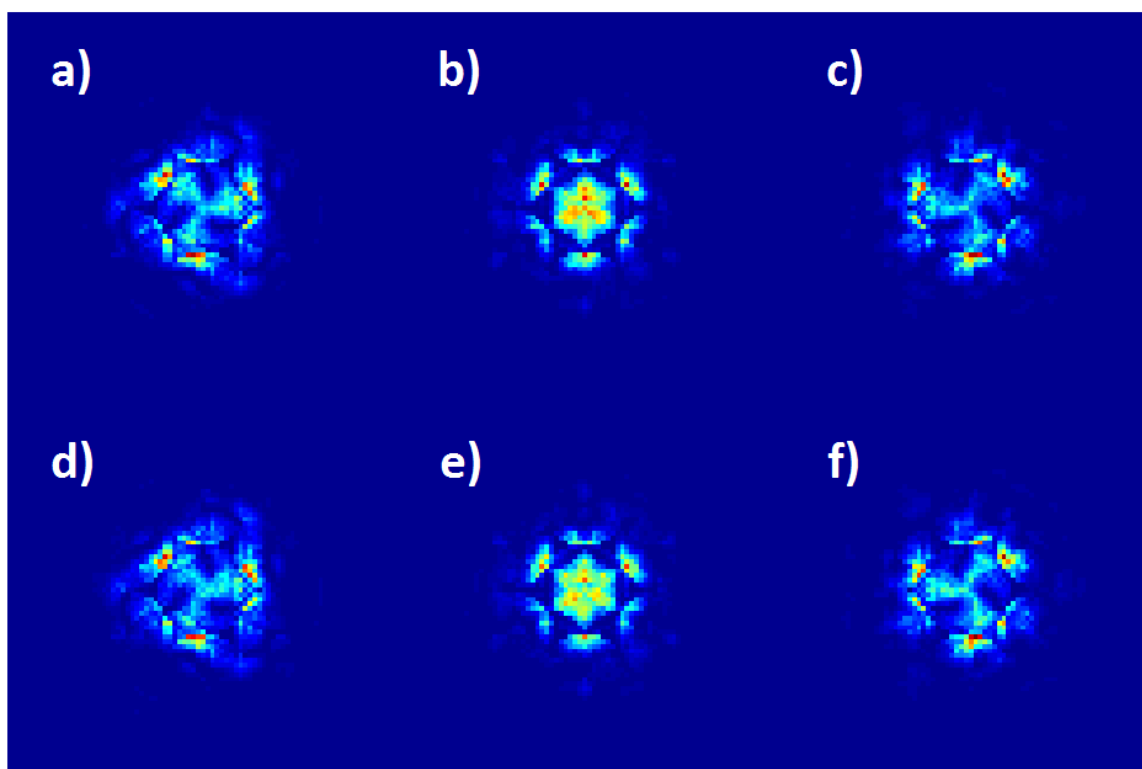


Fig. 4.22 CBED patterns for alpha quartz. The thickness of the crystal is 10nm. The simulation was run with 1024×1024 pixels, with real space dimensions of $40 \times 40 \text{ \AA}$. The beam energy was 10keV and a convergence angle of 29.79 mrad . The crystals are related to each other by being mirrored along the z-direction.

see that by keeping the first layer constant and permuting the other layers such that $2 \rightarrow 9$, $3 \rightarrow 8$ and so on that this does transform one crystal into the other. However by remaining in

the same position after the transformation we see that we end up with a different distance between atomic layers as the beam propagates. For example a beam centred on the right hand helix of Figure 4.23 a will scatter from the Si atom labelled 1 then at the next atomic layer will scatter from the oxygen atom labelled 2. A beam centred on the right hand helix of Figure 4.23 b however will scatter from the Si atom labelled 1 then at the next atomic layer will propagate outwards as there is no atom in the localised intensity of the beam. All of the previous examples in this work relied on crystals which had mirror planes so in these cases the atoms which the beam scattered from, as it propagated, remained the same. Figure 4.24 shows this is also true if the L-quartz in Figure 4.23 was mirrored. By mirroring the quartz, the atomic arrangement in the z direction remains the same, however the chirality changes. We see that when viewing the central region of Figure 4.24 a and Figure 4.24 f they have a similar intensity and also both diffraction patterns have a triangular shape globally. Conversely we see that when viewing the central region of Figure 4.24 c and Figure 4.24 d they have a weaker intensity and are lacking the triangular shape globally. The Gaussian CBED patterns Figure 4.24 b and Figure 4.24 e now match.

Another method to maintain the same scattering layers as the beam propagates would be to move the beam position after flipping the crystal. When we view the right helix in Figure 4.23 a we see the order goes $1 \rightarrow 2 \rightarrow 4 \dots$, this is also the same order seen in the left helix in Figure 4.23 b. Figure 4.25 shows that by moving the beam position after flipping the crystal along the z-direction we get enantiospecific scattering. This sections shows that the weak chiral specific scattering that was shown in previous examples also appears in the real crystal structure quartz. It was shown that simply mirroring the crystal in the z direction did not lead to chiral specific scattering, highlighting that it is the forward scattering of the beam which is the important feature. The enantiospecific scattering was seen on two different points on the unit cell of quartz, and thus could be observed in a real crystal.

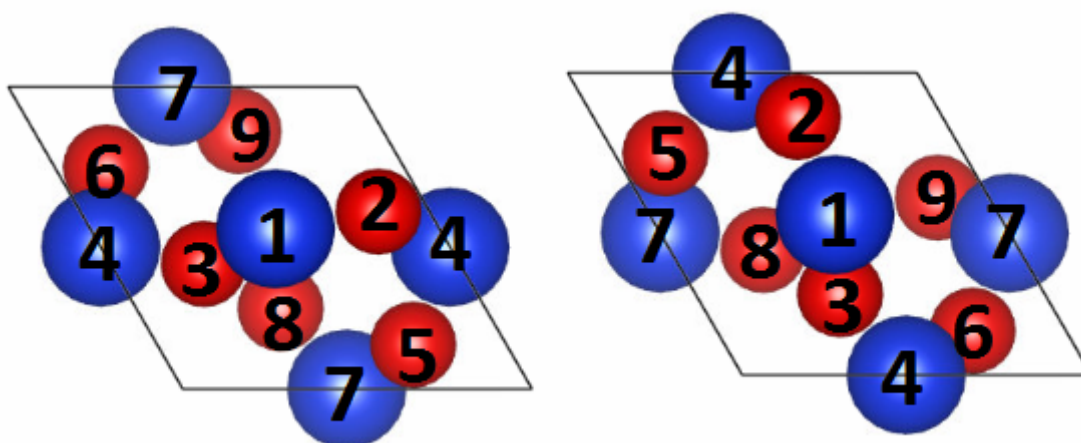


Fig. 4.23 Quartz positions before and after permuting the layers. We see that by keeping the first layer constant and permuting the other layers such that $2 \rightarrow 9$, $3 \rightarrow 8$ and so on, we transform one crystal into the other.

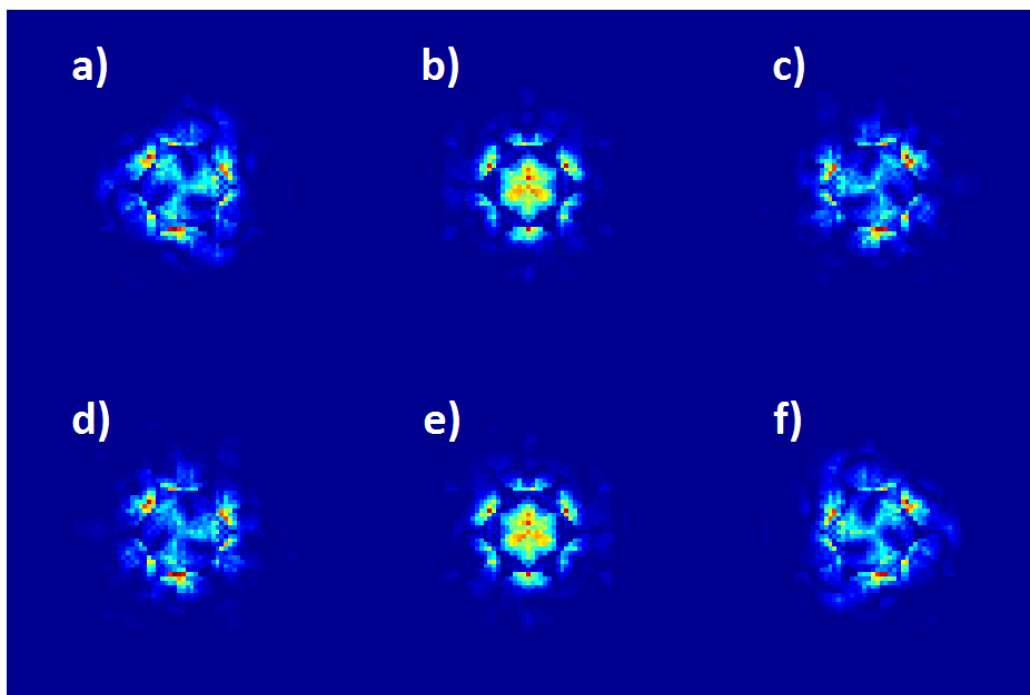


Fig. 4.24 CBED patterns from alpha quartz. The thickness of the crystal is 10nm. The simulation was run with 1024×1024 pixels, with real space dimensions of $40 \times 40 \text{ \AA}$. The beam energy was 10keV and a convergence angle of 29.79 mrad . The crystals are related to each other by a mirror plane perpendicular to the page.

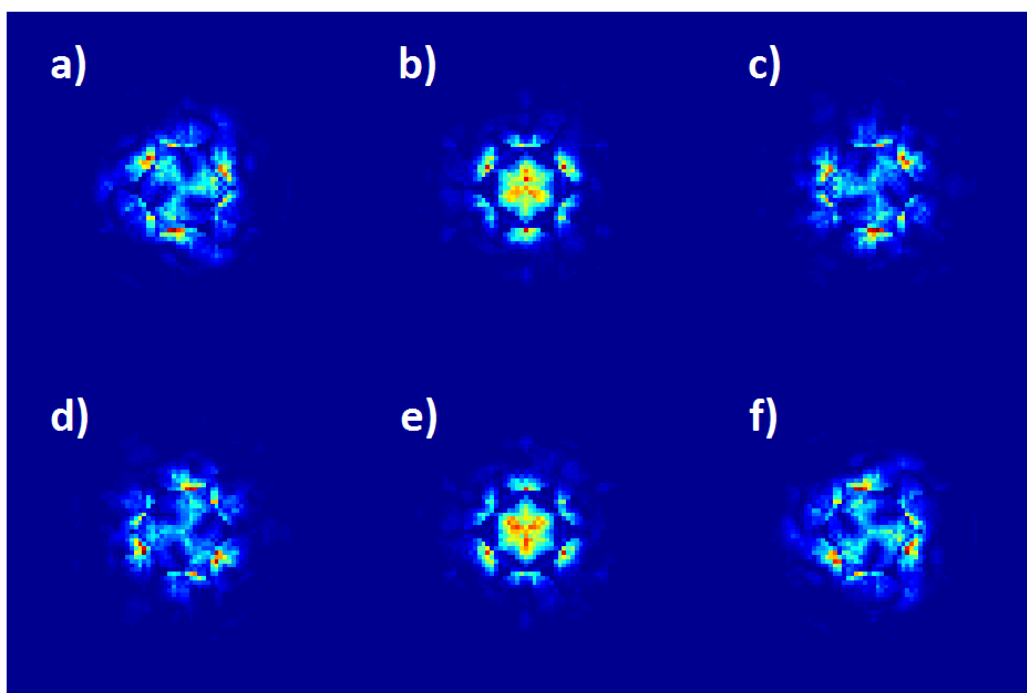


Fig. 4.25 CBED patterns from alpha quartz. The thickness of the crystal is 10nm. The simulation was run with 1024×1024 pixels, with real space dimensions of $40 \times 40 \text{ \AA}$. The beam energy was 10keV and a convergence angle of 29.79 mrad . The crystals are related to each other by being mirrored along the z-direction and a shift in the beam position.

4.7 Vortex Beam Diffraction in NbS_2

Cr_1NbS_2 is a magnetic crystal which has a layered hexagonal structure and belongs to the space group $P6_322$ [112, 113]. This space group contains a six fold screw axis. A clockwise and anticlockwise configuration of Cr_1NbS_2 is shown in Figure 4.26. In this structure the silicon atoms, shown in yellow, form a chiral arrangement about a central column of Niobium atoms, shown in green, which is the six fold screw axis. These silicon atoms can either lie in a clockwise or anticlockwise rotation. This crystal structure was chosen as it both contains a screw axis but also reflecting in a mirror plane perpendicular to the c-axis is equivalent to reflection about the c-axis. It was suggested in the previous section that the difference created by flipping quartz along the c-axis was the reason for not seeing enantiospecific scattering. Figure 4.27 shows the overlap of the vortex beam probability and the crystal structure, again the convergence angle is chosen to align the maximum intensity of the beam with the silicon atoms which form the screw axis.

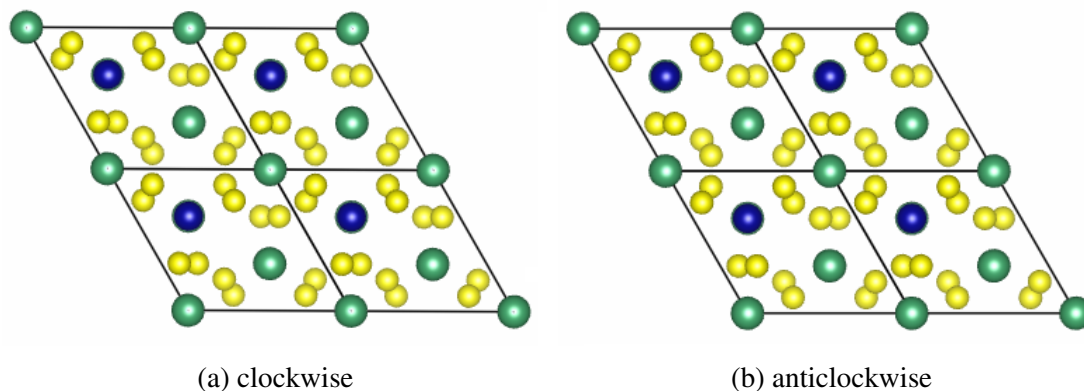


Fig. 4.26 The unit cells of Cr_1NbS_2 showing the two different chiral configurations where the silicon atoms, shown in yellow, form a a) clockwise and (b) anticlockwise crystal when viewed along the c-axis.

The CBED patterns obtained from propagating a plus vortex beam and a minus vortex beam after scattering in the chiral potential shown in Figures 4.26a and 4.26b are shown in Figure 4.28. The top panel shows scattering in a clockwise crystal and the bottom panel shows scattering in an anticlockwise crystal. We see just by viewing the diffraction patterns that we do enantiospecific scattering although, as before, the effects are very weak. This is highlighted by the similarity of the bottom left and top right diffraction patterns and vice versa. Again the similarities arise from the overlap of the CBED disks. In Figure 4.28a and Figure 4.28f we see an increased intensity, shown by the brighter red colour, where the six disks overlap with the central disk. This intensity is reduced in Figure 4.28c and Figure 4.28d. Note that in this example the Gaussian diffraction patterns match, showing that chiral determination can not be done using a planewave.

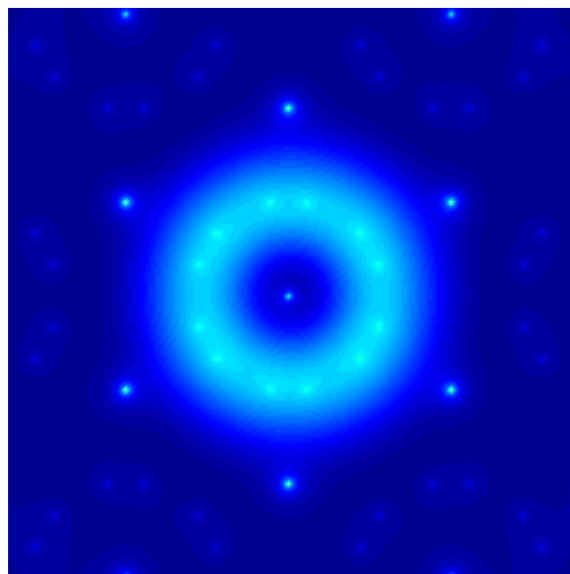


Fig. 4.27 The overlap of the vortex beam probability density with the $Cr_{1/3}NbS_2$ potential, looking down the beam direction. The donut shaped intensity is chosen to lie directly over the silicon atoms which form the screw axis, which results in overlapping diffraction disks.

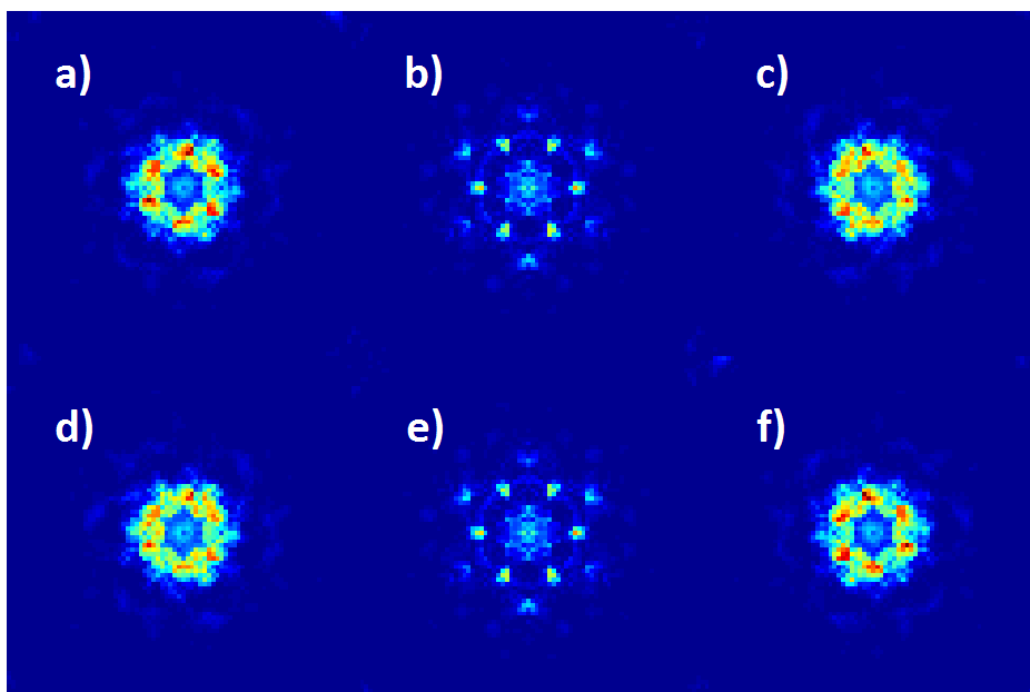


Fig. 4.28 CBED patterns. The thickness of the crystal is 12nm. The simulation was run with 1024×1024 pixels, with real space dimensions of $45.91 \times 45.91 \text{ \AA}$. The beam energy was 10keV and a convergence angle of 29.79mrad .

4.8 Conclusions

We have shown enantiospecific scattering of vortex electron beams from a number of chiral crystal structures and demonstrated the ability to distinguish between enantiomorphs using convergent electron vortex diffraction for crystal thickness down to just a few tens of nanometers thick. In our analysis we used the overlapping disks of CBED patterns to create intensity differences in the region of overlap. We have shown that vortex beams offer a solution to the problem of detecting chirality in crystals by showing the difference in vortex CBED when compared to plane-wave CBED, where for these crystal thickness no effects of the chirality were seen in the CBED patterns. Electron vortex beams are shown to break Friedel's law, allowing the chirality to be observed in CBED patterns. Using this method experimentally, the chirality of an unknown crystal could therefore be assigned simply by comparing the diffraction patterns for L- and R-vortex probes.

Chapter 5

Outlook

5.1 Conclusion and Outlook

This thesis has explored the use of electrons as probes of chiral materials. First we have shown the use of electrons as probes of chiral matter, specifically in electron microscopes. We showed that using an electron beam the plasmon states of a chiral material could be identified using EELS. This was done by examining the similarities in the modes observed between a set of different plasmonic nanoparticles. First the differences between a positive and negative nanoparticle were studied experimentally. We found that by processing the data, first by deconvolving and then performing matrix factorisation, we could reveal the modes which existed in the data sets. EELS provided a powerful tool with which to both spatially map the structure on the nanoscale by plotting the spatial distribution of the plasmonic modes on this scale. We found that the two particles had similar mode structures but the modes were shifted in energy. This will be important in future studies as research interest into templated (hole) nanoparticles increases due to the ease of producing when compared to the positive nanoparticle.

We performed simulations of EELS of these plasmonic nanoparticles, and included a study of the effects of surface roughness and edge imperfections. Four nanoparticles were chosen in order to investigate the role of the structure of the nanoparticles on the modes it could support. It was found that defects, when moving from an ideal high symmetry particle to an experimentally realistic nanoparticle, lead to mode splitting and a change in brightness of the modes. It was also found that the modes supported by an experimentally studied positive and negative nanoparticle can have similar intensity distributions, however may be shifted in energy. This is confirmation of Babinet's principle as the small shifts in energy can be attributed to the small deviations in shape caused by imperfections when the particles are made.

In the concluding chapter we showed that a chiral electron beam can, through diffraction effects, produce different diffraction patterns obtained from enantiomorphic pairs of chiral crystal structures for a number of example crystals. We found that we could, given the

right set up, show chiral selective diffraction from crystal. Future work could consider a number of other crystal structures in which vortex beams could provide 3D information. These include structures like an eshelby twist where a screw axis forms within the bulk of a material. Selective focusing of a vortex beam could exploit the vortex beams pitch and create a diffraction pattern which has information about the handedness of this twist. The technique has clear limitations but there are prospects to remove the difficulty of looking at HOLZ features. This method would require experimental verification in the future. Similar effects are seen in studies where chiral objects, usually molecules, interact with circularly polarized light. In these cases effects such as circular dichroism and optical rotatory dispersion can be observed. This takes advantage of both the chirality of the probing radiation and the chirality of the material under study, in a similar way as was seen in the previous chapter.

Future work would include the combination of the two techniques explored in this work, using a chiral probe to study chiral plasmons. Recent studies have used chiral matching to study chiral plasmonic structures using circularly polarized light. In such an experiment one detects differences in the absorption and transmission spectra after illuminating a sample with left and right-handed circularly polarized light. However this experiment is limited by the same optical resolution as discussed in the introductory chapter where we highlighted that optical techniques are insensitive to dark modes and have limited spatial resolution compared to EELS. This highlights the possibility of merging these two techniques, electron vortex beams and EELS in order to use chiral probes to probe chiral plasmonic states. Since the chirality of the field produced by plasmons and such a field's interaction with matter dictates many potential applications of chiral metamaterials, it is important to understand their distribution and magnitude if the applications are to be realised. This has the potential to form future research in this area.

References

- [1] David B Williams and C Barry Carter. *Transmission Electron Microscopy*. 2009.
- [2] H. Burzlaff and H. Zimmermann. *International Tables for Crystallography Volume A: Space-group symmetry*. Springer Netherlands, Dordrecht, hahn, th. edition, 2002.
- [3] British Museum Collection Database. www.britishmuseum.org/collection.
- [4] L de Broglie. La nouvelle dynamique des quanta. *Annalen der Physik*, 3.3:22–128, 1925.
- [5] Rolf Erni, Marta D. Rossell, Christian Kisielowski, and Ulrich Dahmen. Atomic-resolution imaging with a sub-50-pm electron probe. *Physical Review Letters*, 102(9):1–4, 2009.
- [6] D Richards. Near- Field microscopy : throwing light on the nanoworld. *Philosophical Transactions of the Royal Society A*, 361:2843–2857, 2003.
- [7] R.F. Egerton. *Electron Energy-Loss Spectroscopy in the Electron Microscope*, volume 72. 2011.
- [8] F. H. Read. Inner shell excitation of atoms and molecules by electron impact with high energy resolution. *Le Journal de Physique Colloques*, 39(C1):C1–82–C1–86, 1978.
- [9] Xiaoxing Ke, Carla Bittencourt, and Gustaaf van Tendeloo. Possibilities and limitations of advanced transmission electron microscopy for carbon-based nanomaterials. *Beilstein Journal of Nanotechnology*, 6(1):1541–1557, 2015.
- [10] L. H. Davisson, C. and Germer. Diffraction of electrons by a crystal of Nickel. *Physical Review*, 30(6):705–740, 1927.
- [11] P. P. Ewald. Introduction to the dynamical theory of X-ray diffraction. *Acta Crystallographica Section A*, 25(1):103–108, 1969.
- [12] S. Miyake and R. Uyeda. Friedel’s law in the dynamical theory of diffraction. *Acta Crystallographica*, 8(6):335–342, 1955.
- [13] A V Zayats and Smolyaninov II. Near-field photonics: surface plasmon polaritons and localized surface plasmons. *J. Opt. A: Pure Appl. Opt.*, 5(4):S16–S50, 2003.
- [14] Kathryn M Mayer and Jason H Hafner. Localized surface plasmon resonance sensors. *Chemical Reviews*, 111(6):3828–3857, 2011.
- [15] J. J. Burke, G. I. Stegeman, and T. Tamir. Surface-polariton-like waves guided by thin, lossy metal films. *Physical Review B*, 33(8):5186–5201, 1986.
- [16] M Quinten, A Leitner, J R Krenn, and F R Aussenegg. Electromagnetic energy transport via linear chains of silver nanoparticles [J]. *Optics letters*, 23(17):1331–1333, 1998.

- [17] T. Onuki, Y. Watanabe, K. Nishio, T. Tsuchiya, T. Tani, and T. Tokizaki. Propagation of surface plasmon polariton in nanometre-sized metal-clad optical waveguides. *Journal of Microscopy*, 210(3):284–287, 2003.
- [18] Stephan Link and Mostafa A El-sayed. Spectral properties and relaxation dynamics of surface plasmon electronic oscillations in Gold and Silver nanodots and nanorods. *Journal of Physical Chemistry B*, 103(1):8410–8426, 1999.
- [19] Michel Bosman, Vicki J Keast, Masashi Watanabe, Abbas I Maarroof, and Michael B Cortie. Mapping surface plasmons at the nanometre scale with an electron beam. *Nanotechnology*, 18(16):165505, 2007.
- [20] Jaysen Nelayah, Mathieu Kociak, Odile Stéphan, F. Javier García de Abajo, Marcel Tencé, Luc Henrard, Dario Taverna, Isabel Pastoriza-Santos, Luis M. Liz-Marzán, and Christian Colliex. Mapping surface plasmons on a single metallic nanoparticle. *Nature Physics*, 3(5):348–353, 2007.
- [21] A. J. Ward and J. B. Pendry. Program for calculating photonic band structures, Green’s functions and transmission/reflection coefficients using a non-orthogonal FDTD method. *Computer Physics Communications*, 128(3):590–621, 2000.
- [22] Jens Niegemann, Michael König, Kai Stannigel, and Kurt Busch. Higher-order time-domain methods for the analysis of nano-photonic systems. *Photonics and Nanostructures - Fundamentals and Applications*, 7(1):2–11, 2009.
- [23] Vincent L Y Loke, M. Pinar Mengüç, and Timo A. Nieminen. Discrete-dipole approximation with surface interaction: Computational toolbox for MATLAB. *Journal of Quantitative Spectroscopy and Radiative Transfer*, 112(11):1711–1725, 2011.
- [24] F. J. García de Abajo and A. Howie. Retarded field calculation of electron energy loss in inhomogeneous dielectrics. *Physical Review B (Condensed Matter and Materials Physics)*, 65:115418 — 17, 2002.
- [25] Ulrich Hohenester and Andreas Trügler. MNPBEM - A Matlab toolbox for the simulation of plasmonic nanoparticles. *Computer Physics Communications*, 183(2):370–381, 2012.
- [26] Ming-Wen Chu, Viktor Myroshnychenko, Cheng Hsuan Chen, Jing-Pei Deng, Chung-Yuan Mou, and F Javier García de Abajo. Probing bright and dark surface-plasmon modes in individual and coupled noble metal nanoparticles using an electron beam. *Nano letters*, 9(1):399–404, 2009.
- [27] Brent Fultz and James M. Howe. *Transmission electron microscopy and diffractometry of materials*. 2008.
- [28] M Lenzlinger and E H Snow. Fowler-Nordheim Tunneling into Thermally Grown SiO₂. *Journal of Applied Physics*, 40(1):278–283, 1969.
- [29] Max T. Otten and Wim M J Coene. High-resolution imaging on a field emission TEM. *Ultramicroscopy*, 48(1-2):77–91, 1993.
- [30] William Thomson Kelvin. Baltimore Lectures on Molecular Dynamics and the Wave Theory of Light. *C.J. Clay, London*, pages 602–642, 1904.
- [31] L D Barron. Chirality, magnetism and light. *Nature*, 405(June):895–896, 2000.

- [32] Zhaofeng Li, Mehmet Mutlu, and Ekmel Ozbay. Chiral metamaterials: from optical activity and negative refractive index to asymmetric transmission. *Journal of Optics*, 15(2):023001, 2013.
- [33] John A. Schellman. Circular dichroism and optical rotation. *Chemical Reviews*, 75(3):323–331, 1975.
- [34] Ventsislav K. Valev, Jeremy J. Baumberg, Concita Sibilia, and Thierry Verbiest. Chirality and chiroptical effects in plasmonic nanostructures: Fundamentals, recent progress, and outlook. *Advanced Materials*, 25(18):2517–2534, 2013.
- [35] Jino George and K. George Thomas. Surface plasmon coupled circular dichroism of Au nanoparticles on peptide nanotubes. *Journal of the American Chemical Society*, 132(8):2502–2503, 2010.
- [36] E Hendry, T Carpy, J Johnston, M Popland, R V Mikhaylovskiy, A J Laphorn, S M Kelly, L D Barron, N Gadegaard, and M Kadodwala. Ultrasensitive detection and characterization of biomolecules using superchiral fields. *Nat Nanotechnol*, 5(11):783–787, 2010.
- [37] Xiaoling Wu, Liguang Xu, Liqiang Liu, Wei Ma, Honghong Yin, Hua Kuang, Libing Wang, Chuanlai Xu, and Nicholas A. Kotov. Unexpected chirality of nanoparticle dimers and ultrasensitive chiroplasmonic bioanalysis. *Journal of the American Chemical Society*, 135(49):18629–18636, 2013.
- [38] Y. Zhao, M.a. Belkin, and A. Alù. Twisted optical metamaterials for planarized ultrathin broadband circular polarizers. *Nature Communications*, 3(May):870, 2012.
- [39] Elna Pidcock. Achiral molecules in non-centrosymmetric space groups. *Chemical Communications*, (27):3457–3459, 2005.
- [40] P. Goodman and a. W. S. Johnson. Identification of enantiomorphically related space groups by electron diffraction – a second method. *Acta Crystallographica Section A*, 33(6):997–1001, 1977.
- [41] Andrew W S Johnson. Chiral determination: direct interpretation of convergent-beam electron diffraction patterns using the series expansion of Cowley and Moodie. *Acta crystallographica. Section B, Structural science*, 63(Pt 4):511–20, aug 2007.
- [42] A F Moodie and H J Whitfield. Friedel’s law and non-centrosymmetric space groups. *Acta Crystallographica Section A*, 51(2):198–201, 1995.
- [43] L. Allen, M. W. Beijersbergen, R. J C Spreeuw, and J. P. Woerdman. Orbital angular momentum of light and the transformation of Laguerre-Gaussian laser modes. *Physical Review A*, 45(11):8185–8189, 1992.
- [44] Shubo Cheng and Shaohua Tao. Vortex-based line beam optical tweezers. *Journal of Optics*, 18(10):105603, 2016.
- [45] Miles Padgett, Johannes Courtial, and Les Allen. Light’s Orbital Angular Momentum. *Physics Today*, 57(May):35, 2004.
- [46] J Verbeeck, H Tian, and P Schattschneider. Production and application of electron vortex beams. *Nature*, 467(7313):301–4, sep 2010.
- [47] Johannes Paul, Armin Dörzbach, and Konstantin Siegmann. Circular Dichroism in the Photoionization of Nanoparticles from Chiral Compounds. *Physical Review Letters*, 79(16):2947–2950, 1997.

- [48] Konstantin Yu Bliokh, Yury P. Bliokh, Sergey Savel'Ev, and Franco Nori. Semiclassical dynamics of electron wave packet states with phase vortices. *Physical Review Letters*, 99(19):1–4, 2007.
- [49] Masaya Uchida and Akira Tonomura. Generation of electron beams carrying orbital angular momentum. *Nature*, 464(7289):737–9, apr 2010.
- [50] Sophia Lloyd, Mohamed Babiker, and Jun Yuan. Quantized Orbital Angular Momentum Transfer and Magnetic Dichroism in the Interaction of Electron Vortices with Matter. *Physical Review Letters*, 108(7):074802, feb 2012.
- [51] Roeland Juchtmans and Jo Verbeeck. Local orbital angular momentum revealed by spiral-phase-plate imaging in transmission-electron microscopy. *Physical Review A - Atomic, Molecular, and Optical Physics*, 93(2):1–7, 2016.
- [52] Stefan Löffler and Peter Schattschneider. Elastic propagation of fast electron vortices through crystals. *Acta Crystallographica Section A Foundations of Crystallography*, 68(4):443–447, may 2012.
- [53] J. M. Cowley and a. F. Moodie. The scattering of electrons by atoms and crystals. I. A new theoretical approach. *Acta Crystallographica*, 10(10):609–619, oct 1957.
- [54] Earl J. Kirkland. *Advanced computing in electron microscopy*. 2010.
- [55] J Zenneck. Über die Fortpflanzung ebener elektromagnetischer Wellen längs einer ebenen Leiterfläche und ihre Beziehung zur drahtlosen Telegraphie. *Annalen der Physik*, 328(10):846–866, 1907.
- [56] R W Wood. On a Remarkable Case of Uneven Distribution of Light in a Diffraction Grating Spectrum. *Proceedings of the Physical Society of London*, 18(1):269–275, 1902.
- [57] U. Fano. The Theory of Anomalous Diffraction Gratings and of Quasi-Stationary Waves on Metallic Surfaces (Sommerfeld's Waves). *Journal of the Optical Society of America*, 31(3):213–222, 1941.
- [58] R. H. Ritchie. Plasma Losses by Fast Electrons in Thin Films. *Physical Review*, 106(5):874–881, 1957.
- [59] C. J. Powell and J. B. Swan. Origin of the characteristic electron energy losses in aluminum. *Physical Review*, 115(4):869–875, 1959.
- [60] E. Kretschmann and H. Raether. Radiative Decay of Non Radiative Surface Plasmons Excited by Light. *Zeitschrift für Naturforschung - Section A Journal of Physical Sciences*, 23(12):2135–2136, 1968.
- [61] Andreas Otto. Excitation of nonradiative surface plasma waves in silver by the method of frustrated total reflection. *Zeitschrift für Physik A Hadrons and nuclei*, 216(4):398–410, Aug 1968.
- [62] J. C. Maxwell Garnett. Colours in Metal Glasses and in Metallic Films. *Philosophical Transactions of the Royal Society A*, 203:385–420, 1904.
- [63] Gustav Mie. Beiträge zur Optik trüber Medien, speziell kolloidaler Metallösungen. *Annalen der Physik*, 330(3):377–445, 1908.

- [64] Katherine A Willets, Rp Van Duyne, and Richard P Van Duyne. Localized Surface Plasmon Resonance Spectroscopy and Sensing. *Annual Review of Physical Chemistry*, 58(1):267–297, 2007.
- [65] J. G. Gordon and S. Ernst. Surface plasmons as a probe of the electrochemical interface. *Surface Science*, 101(1-3):499–506, 1980.
- [66] Claes Nylander, Bo Liedberg, and Tommy Lind. Gas detection by means of surface plasmon resonance. *Sensors and Actuators*, 3(C):79–88, 1982.
- [67] Jiri Homola, Sinclair S. Yee, and Gunter Gauglitz. Surface plasmon resonance sensors: review. *Sensors and Actuators B: Chemical*, 54(1-2):3–15, 1999.
- [68] Nathan G. Greeneltch, Martin G. Blaber, George C. Schatz, and Richard P. Van Duyne. Plasmon-sampled surface-enhanced raman excitation spectroscopy on silver immobilized nanorod assemblies and optimization for near infrared studies. *Journal of Physical Chemistry C*, 117(6):2554–2558, 2013.
- [69] R. Carles, M. Bayle, P. Benzo, G. Benassayag, C. Bonafos, G. Cacciato, and V. Privitera. Plasmon-resonant Raman spectroscopy in metallic nanoparticles: Surface-enhanced scattering by electronic excitations. *Physical Review B - Condensed Matter and Materials Physics*, 92(17):1–13, 2015.
- [70] T Brintlinger, A A Herzing, J P Long, I Vurgaftman, R Stroud, and B S Simpkins. Optical dark-field and electron energy loss imaging and spectroscopy of symmetry-forbidden modes in loaded nanogap antennas. *ACS Nano*, 9(6):6222–6232, 2015.
- [71] Affar S. Karimullah, Calum Jack, Ryan Tullius, Vincent M. Rotello, Graeme Cooke, Nikolaj Gadegaard, Laurence D. Barron, and Malcolm Kadodwala. Disposable Plasmonics: Plastic Templated Plasmonic Metamaterials with Tunable Chirality. *Advanced Materials*, 27(37):5610–5616, 2015.
- [72] T.w. Ebbesen, H.j. Lezec, H. F. Ghaemi, T. Thio, and P. A. Wolff. Extraordinary optical transmission through sub-wavelength hole arrays. *Nature*, 391(6668):667, 1998.
- [73] Julia Braun, Bruno Gompf, Georg Kobiela, and Martin Dressel. How holes can obscure the view: Suppressed transmission through an ultrathin metal film by a subwavelength hole array. *Physical Review Letters*, 103(20):1–4, 2009.
- [74] F. J. Garcia-Vidal, L. Martin-Moreno, T. W. Ebbesen, and L. Kuipers. Light passing through subwavelength apertures. *Reviews of Modern Physics*, 82(1):729–787, 2010.
- [75] Ahmer Naweed, Frank Baumann, William a Bailey, Aram S Karakashian, and William D Goodhue. Evidence for Radiative Damping in Surface-Plasmon-Mediated Light Transmission Through Perforated Conducting Films. *J. Opt. Soc. Am. B*, 20(12):2534, 2003.
- [76] K. J K Koerkamp, S. Enoch, F. B. Segerink, N. F. Van Hulst, and L. Kuipers. Strong influence of hole shape on extraordinary transmission through periodic arrays of subwavelength holes. *Physical Review Letters*, 92(18):183901–1, 2004.
- [77] Wilfried Sigle, Jaysen Nelayah, Christoph T Koch, and Peter a van Aken. Electron energy losses in Ag nanoholes—from localized surface plasmon resonances to rings of fire. *Optics letters*, 34(14):2150–2152, 2009.

- [78] Felix von Cube, Stephan Irsen, Jens Niegemann, Christian Matyssek, Wolfram Hergert, Kurt Busch, and Stefan Linden. Spatio-spectral characterization of photonic meta-atoms with electron energy-loss spectroscopy [Invited]. *Optical Materials Express*, 1(5):1009, 2011.
- [79] P. E. Batson. Surface plasmon coupling in clusters of small spheres. *Physical Review Letters*, 49(13):936–940, 1982.
- [80] P. E. Batson. Inelastic scattering of fast electrons in clusters of small spheres. *Surface Science*, 156:720–734, 1985.
- [81] N. Zabala, A. Rivacoba, and P. Echenique. Coupling effects in the excitations by an external electron beam near close particles. *Physical Review B*, 56(12):7623–7635, 1997.
- [82] P. E. Batson, N. Dellby, and O. L. Krivanek. Sub-ångstrom resolution using aberration corrected electron optics. *Nature*, 418(6898):617–620, 2002.
- [83] Shuang Zhang, Dentcho A. Genov, Yuan Wang, Ming Liu, and Xiang Zhang. Plasmon-induced transparency in metamaterials. *Physical Review Letters*, 101(4):1–4, 2008.
- [84] E. Wolf and M. Born. *Principles of Optics*. Cambridge University Press, Cambridge, 2002.
- [85] T. Zentgraf, T. P. Meyrath, A. Seidel, S. Kaiser, H. Giessen, C. Rockstuhl, and F. Lederer. Babinet’s principle for optical frequency metamaterials and nanoantennas. *Physical Review B - Condensed Matter and Materials Physics*, 76(3):4–7, 2007.
- [86] David Rossouw and Gianluigi A. Botton. Resonant optical excitations in complementary plasmonic nanostructures. *Optics Express*, 20(7):6968–6973, 2012.
- [87] E. Plum, J. Zhou, J. Dong, V. A. Fedotov, T. Koschny, C. M. Soukoulis, and N. I. Zheludev. Metamaterial with negative index due to chirality. *Physical Review B - Condensed Matter and Materials Physics*, 79(3):1–6, 2009.
- [88] W. Richardson and W. Richardson. Bayesian-based iterative method of image restoration. *Journal of the Optical Society of America*, 62(1):55–59, 1972.
- [89] L. B. Lucy. An iterative technique for the rectification of observed distributions. *The Astronomical Journal*, 79:745, 1974.
- [90] A. Gloter, A. Douiri, M. Tencé, and C. Colliex. Improving energy resolution of eels spectra: an alternative to the monochromator solution. *Ultramicroscopy*, 96(3):385 – 400, 2003. Proceedings of the International Workshop on Strategies and Advances in Atomic Level Spectroscopy and Analysis.
- [91] J. M. Zuo. Electron detection characteristics of a slow-scan CCD camera, imaging plates and film, and electron image restoration. *Microscopy Research and Technique*, 49(3):245–268, 2000.
- [92] D. D. Lee and H. S. Seung. Learning the parts of objects by non-negative matrix factorization. *Nature*, 401(6755):788–91, 1999.
- [93] Pentti Paatero and Unto Tapper. Positive Matrix Factorization - A Nonnegative Factor Model with Optimal Utilization of Error Estimates of Data Values. *Environmetrics*, 5(2):111–126, 1994.

- [94] Michael W. Berry, Murray Browne, Amy N. Langville, V. Paul Pauca, and Robert J. Plemmons. Algorithms and applications for approximate nonnegative matrix factorization. *Computational Statistics and Data Analysis*, 52(1):155–173, 2007.
- [95] Olivia Nicoletti, Francisco de la Peña, Rowan K Leary, Daniel J Holland, Caterina Ducati, and Paul a Midgley. Three-dimensional imaging of localized surface plasmon resonances of metal nanoparticles. *Nature*, 502(7469):80–4, 2013.
- [96] T. Malis, S. C. Cheng, and R. F. Egerton. Log-Ratio Technique for Specimen-Thickness Measurement in the TEM. *Journal of Electron Microscopy Technique*, 8(2):193–200, 1988.
- [97] Alejandro Portela, Takaaki Yano, Christian Santschi, Hiroaki Matsui, Tomohiro Hayashi, Masahiko Hara, Olivier J F Martin, and Hitoshi Tabata. Spectral tunability of realistic plasmonic nanoantennas. *Applied Physics Letters*, 105(9):2–7, 2014.
- [98] Andreas M. Kern and Olivier J F Martin. Excitation and reemission of molecules near realistic plasmonic nanostructures. *Nano Letters*, 11(2):482–487, 2011.
- [99] C. Moosmann, G. S. Sigurdsson, M. D. Wissert, K. Dopf, U. Lemmer, and H.-J. Eisler. Investigating the influences of the precise manufactured shape of dipole nanoantennas on their optical properties. *Optics Express*, 21(1):594–604, 2013.
- [100] Achim Gelessus, Walter Thiel, and Wolfgang Weber. Multipoles and Symmetry. *Journal of Chemical Education*, 72(6):505, 1995.
- [101] Stéphane Olivier Guillaume, F. Javier García De Abajo, and Luc Henrard. Efficient modal-expansion discrete-dipole approximation: Application to the simulation of optical extinction and electron energy-loss spectroscopies. *Physical Review B - Condensed Matter and Materials Physics*, 88(24):1–10, 2013.
- [102] V Myroshnychenko, J Nelayah, G Adamo, N Geuquet, J Rodriguez-Fernandez, I Pastoriza-Santos, K F MacDonald, L Henrard, L M Liz-Marzan, N I Zheludev, M Kociak, and F J G de Abajo. Plasmon Spectroscopy and Imaging of Individual Gold Nanodecahedra: A Combined Optical Microscopy, Cathodoluminescence, and Electron Energy-Loss Spectroscopy Study. *Nano letters*, 12(8):4172–4180, 2012.
- [103] Guillaume Boudarham and Mathieu Kociak. Modal decompositions of the local electromagnetic density of states and spatially resolved electron energy loss probability in terms of geometric modes. *Physical Review B*, 85(24):245447, 2012.
- [104] Ulrich Hohenester, Harald Ditlbacher, and Joachim R. Krenn. Electron-Energy-Loss Spectra of Plasmonic Nanoparticles. *Physical Review Letters*, 103(10):106801, 2009.
- [105] A Vansteenkiste, M Weigand, M Curcic, H Stoll, G Schütz, and B Van Waeyenberge. Chiral symmetry breaking of magnetic vortices by sample roughness. *New Journal of Physics*, 11(6):063006, 2009.
- [106] H. He, M. E J Friese, N. R. Heckenberg, and H. Rubinsztein-Dunlop. Direct Observation of Transfer of Angular Momentum to Absorptive Particles from a Laser Beam with a Phase Singularity. *Physical Review Letters*, 75(5):826–829, 1995.
- [107] P Schattschneider, S Löffler, M Stöger-Pollach, and J Verbeeck. Is magnetic chiral dichroism feasible with electron vortices? *Ultramicroscopy*, 136:81–5, jan 2014.
- [108] Hiroshi Daimon, Shin Imada, and Shigemasa Suga. Direct surface-structure analysis by the peak rotation in circularly polarized light photoelectron diffraction. *Surface Science*, 471:143–150, 2001.

- [109] Roeland Juchtmans and B Armand. Using electron vortex beams to determine chirality of crystals in transmission electron microscopy. *Physical Review B*, 91(m), 2015.
- [110] W. Kossel and G. Möllenstedt. Elektroneninterferenzen im konvergenten Bündel. *Annalen der Physik*, 428:113–140, 1939.
- [111] Kenso Soai, Shunji Osanai, Kousuke Kadowaki, Shigeru Yonekubo, Takanori Shibata, and Itaru Sato. d- and l-Quartz-Promoted Highly Enantioselective Synthesis of a Chiral Organic Compound. *Journal of the American Chemical Society*, 121(48):11235–11236, 1999.
- [112] Y. Togawa, T. Koyama, K. Takayanagi, S. Mori, Y. Kousaka, J. Akimitsu, S. Nishihara, K. Inoue, A. S. Ovchinnikov, and J. Kishine. Chiral magnetic soliton lattice on a chiral helimagnet. *Physical Review Letters*, 108(10):21–25, 2012.
- [113] T. Moriya and T. Miyadai. Evidence for the helical spin structure due to antisymmetric exchange interaction in Cr₁₋₃NbS₂. *Solid State Communications*, 42(3):209–212, 1982.